CERN 2000–012
15 December 2000

ORGANISATION EUROPÉENNE POUR LA RECHERCHE NUCLÉAIRE
CERN EUROPEAN ORGANIZATION FOR NUCLEAR RESEARCH

CONCEPTUAL DESIGN OF THE SPL, A HIGH-POWER SUPERCONDUCTING H^- LINAC AT CERN

B. Autin, A. Blondel, K. Bongardt, R. Cappi, F. Caspers, E. Cennini, E. Chiaveri, S. Claudet, R. Garoby, F. Gerigk H. Haseroth, C. Hill, N. Hilleret, J. Inigo-Golfin, M. Jimenez, A. Krusche, D. Kuchler, M. Lindroos, A. Lombardi, R. Losito, R. Nunes, M. Paoluzzi, J. Pedersen, M. Poehler, H. Ravn, M. Sanmartí, H. Schönauer, M. Silari, J. Tückmantel, A. Vital, M. Vretenar

Editor: M. Vretenar

GENEVA
2000

CERN–Service d’information scientifique–RD/1008–1000–décembre 2000

ABSTRACT

The conceptual design of a superconducting H^- linear accelerator at CERN for a beam energy of 2.2 GeV and a power of 4 MW is presented. Using most of the superconducting RF cavities available after the decommissioning of LEP, it operates at 352 MHz and delivers 10^{16} protons per second, in 2.2 ms bursts with a repetition rate of 75 Hz. In conjunction with an accumulator and a compressor, it is designed to be the proton driver of a neutrino factory at CERN. At an early stage, it will upgrade the performance of the PS complex by replacing Linac2 and the PS Booster, by injecting protons directly into the PS. The brilliance of the LHC beam will thus be tripled. The present ISOLDE facility can be supplied with five times more beam current than today, and a new-generation radioactive ion beam facility receiving up to 100 μA beam current could also be accommodated. More generally, the PS beam intensity will be substantially increased at all energies, with a direct benefit for fixed-target physics and especially neutrino physics based on pion decay.

GLOSSARY

Abbreviations

AD	Antiproton Decelerator
BNL	Brookhaven National Laboratory, USA
CEA	Commissariat pour l'Energie Atomique, France
CNGS	CERN Neutrino Gran Sasso
CW	Continuous Wave
d.c.	Direct Current
DESY	Deutsches Elektronen-Synchrotron, Hamburg, Germany
DTL	Drift Tube Linac
ECR	Electron Cyclotron Resonance
ESS	European Spallation Source
GSI	Gesellschaft für Schwerionenforschung mbH, Darmstadt, Germany
IGBT	Insulated Gate Bipolar Transistor
INFN	Istituto Nazionale di Fisica Nucleare, Italy
ISOLDE	Isotope Separator on Line experiment at CERN
ISR	Intersecting Storage Ring
LANL	Los Alamos National Laboratory, USA
LEBT	Low-Energy Beam Transport
LEP	Large Electron–Positron storage ring
LEP1	LEP – Phase 1 (only copper cavities)
LEP2	LEP – Phase 2 (adding superconducting cavities)
LHC	Large Hadron Collider
Linac	Linear Accelerator
MEBT	Medium Energy Beam Transport
MOSFET	Metal Oxide Semiconductor Field Effect Transistor
NToF	Neutron Time of Flight
NuPECC	Nuclear Physics European Collaboration Committee
PS	Proton Synchrotron (refers to the CERN 28 GeV Proton Synchrotron)
PTFE	Polytetrafluoroethylene
r.m.s.	root mean square
RF	Radio Frequency
RFQ	Radio Frequency Quadrupole
RNB	Radioactive Nuclear Beam
SNS	Spallation Neutron Source, Oak Ridge, USA
SPS	Super Proton Synchrotron
TESLA	TeV Energy Superconducting Linear Accelerator project at DESY
TT(n.)	Transfer Tunnel (n.), CERN beam transfer tunnel

Parameters

h	Harmonic number
Q	Quality factor or synchrotron tune
R/Q	Form factor (shunt impedance over quality factor)
T	kinetic energy
V_{RF}	RF voltage
β	Relativistic velocity
ϕ	Synchronous phase
λ	RF wavelength

CONTENTS

1. INTRODUCTION AND EXECUTIVE SUMMARY

The ever-increasing flux of secondary particles requested by physics experiments can only be met using higher power proton beams. Especially demanding are the needs of a neutrino factory, which requires 4 MW of beam power on target to provide 10^{21} high-energy muons per year [1, 2]. These requests have re-activated the study of a Superconducting Proton Linac (SPL) already proposed [3, 4] as an upgraded injector for the CERN PS. Triggered by a previous proposal to re-use the LEP RF hardware for the proton driver of an energy amplifier [5, 6], this machine was originally intended to accelerate mainly protons, and although in the following studies the advantages of a common H^- operation for all the users became clear, the name SPL has been retained. The basic linac characteristics for the present configuration are summarized in Table 1.1.

Table 1.1: Basic SPL characteristics.

Mean beam power	4 MW
Kinetic energy	2.2 GeV
Repetition rate	75 Hz
Pulse duration	2.2 ms
Number of protons per pulse (per second)	1.5×10^{14} (1.1×10^{16})
Mean current during a pulse	11 mA
Overall length	799 m
Bunch frequency (minimum time between bunches)	352.2 MHz (2.84 ns)
Peak RF power at 352.2 MHz	32 MW

In the present set-up of the driver for a neutrino factory at CERN [7, 8, 9], the SPL supplies H^- ions to a fixed-energy accumulator which collects protons during 2.2 ms in 140 bunches, and ejects them as a 3.3 μs burst into a compressor ring where the length of the bunches is reduced to 1 ns r.m.s. [10]. Although the SPL is designed for that purpose, minor modulations of its parameters make it a high-performance injector for the PS as well as an excellent driver for the present ISOLDE target and for a potential future radioactive ion beam facility. These issues are addressed in Section 2.

The design of the accelerator is presented in detail in Sections 3 and 4. It is based upon the re-use of LEP RF equipment that will be available after the end of 2000. As many klystrons are used as in LEP-2, although in pulsed mode with a 30% duty cycle. Out of the 800 m of Linac length, more than 500 m are equipped with LEP-2 RF cryostats either unmodified (for 360 m, above 1085 MeV) or refurbished with five-cell $\beta = 0.8$ resonators (for 150 m between 390 and 1085 MeV). The low-energy part up to 390 MeV (~ 280 m) is of a completely new design; above 120 MeV, superconducting cavities are used, while room-temperature structures are preferred below that energy.

The main parameters of the different components of the linear accelerator are summarized in the Appendix. The layout on the CERN site is shown in Fig. 1.1 and detailed in Section 5. To minimize the cost of civil engineering, the linac location is optimized for injection into the accumulator ring of the neutrino factory situated on the ISR site, and extensive use is made of the tunnels connecting it to the PS. A 60 kW beam dump is foreseen in the prolongation of the linac tunnel which could receive nominal beam pulses at a rate of 1 Hz. The rest of the neutrino factory will probably extend underground and beyond the present limits of the CERN site.

For the linac itself, tunnel work is very limited and the accelerator as well as the klystron gallery are built in trenches in a small extension of the CERN territory. The infrastructure for the services

(electricity, cryogenics, water cooling, etc.) is of a significant size and makes maximum use of existing buildings.

At this stage of the study, the SPL design and performance have been tailored to the presently expressed needs of a neutrino factory and to the specificity of the means and site available at CERN. However, these may still evolve if the requirements of the neutrino factory change, for example because of the results of the HARP experiment [11], because of evolutions in the design of the muon accelerator, or simply because of new needs for physics (a non-exhaustive list of possibilities is sketched in Section 7). For example, a preliminary analysis of the possibility of running the SPL at a higher duty factor to provide more than 4 MW of beam power is given in Section 6. Moreover, the various parts of the accelerator are in different states of development and in some cases solutions have still to be developed (e.g. the $\beta = 0.52$ superconducting section where a room-temperature solution could still be considered).

This report nevertheless confirms the great potential of a high-energy, high-power proton linac at CERN, as well as the great value of the LEP RF equipment for the Organization. The information it contains is a solid basis for any future work in this direction.

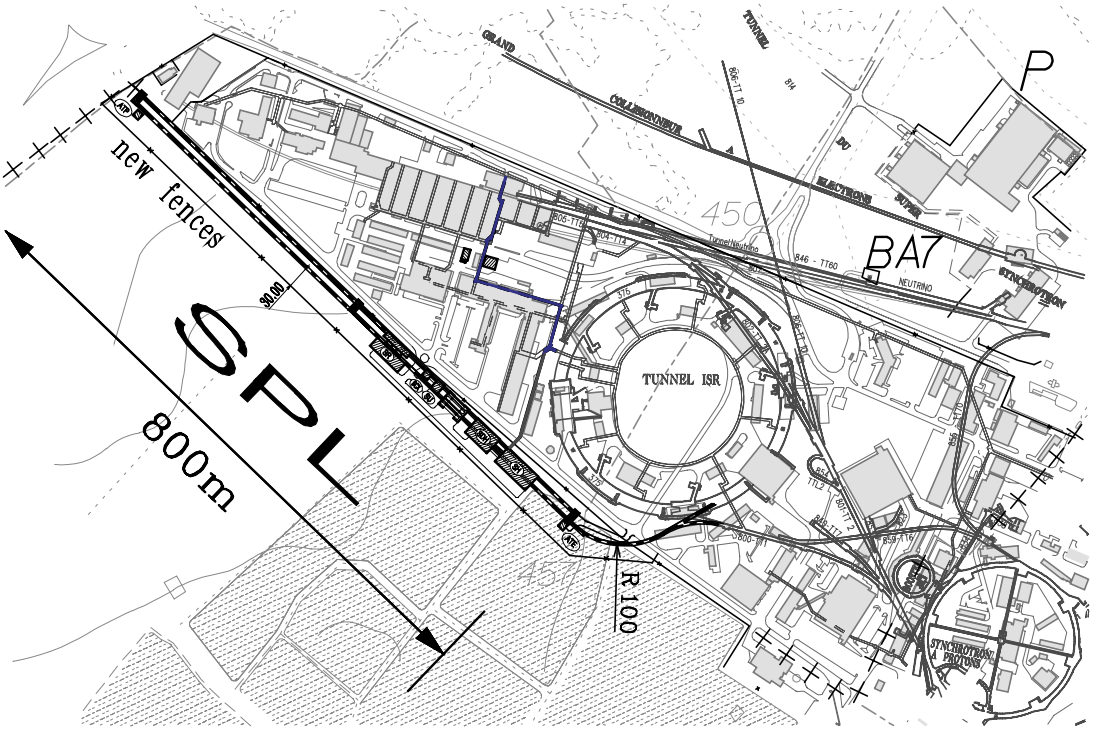

Fig. 1.1: SPL layout on the CERN site.

2. APPLICATIONS AND PERFORMANCE REQUIREMENTS

2.1 Proton driver for a neutrino factory

2.1.1 Requirements of a neutrino factory

The scenario for bunch rotation, cooling and acceleration of muons which has recently been adopted at CERN [12] is well matched to the capability of a linac-based proton driver. The overall neutrino facility is sketched in Fig. 2.1. The proton beam is sent onto a target to produce pions which are captured in a solenoidal channel where they decay into muons. These have a time structure similar to the proton beam impinging the target. Bunches being short (1 ns r.m.s.) with respect to the distance between them (23 ns), bunch (phase) rotation can be applied using 44 MHz RF systems to reduce their energy spread by increasing their length. Afterwards, ionization cooling is used to increase the density of muons and the fraction of muons that can be accelerated in the following cascade of linac and recirculating accelerators which bring the energy up to 50 GeV. Finally these muons are injected inside a storage ring with long straight sections aimed at remote experiments which will be irradiated by the flux of neutrinos resulting from the muons' decays. As the 50 GeV muons have a lifetime of ~ 1 ms in the laboratory frame, the storage ring can be refilled every few milliseconds. The required characteristics of the proton beam hitting the target are summarized in Table 2.1.

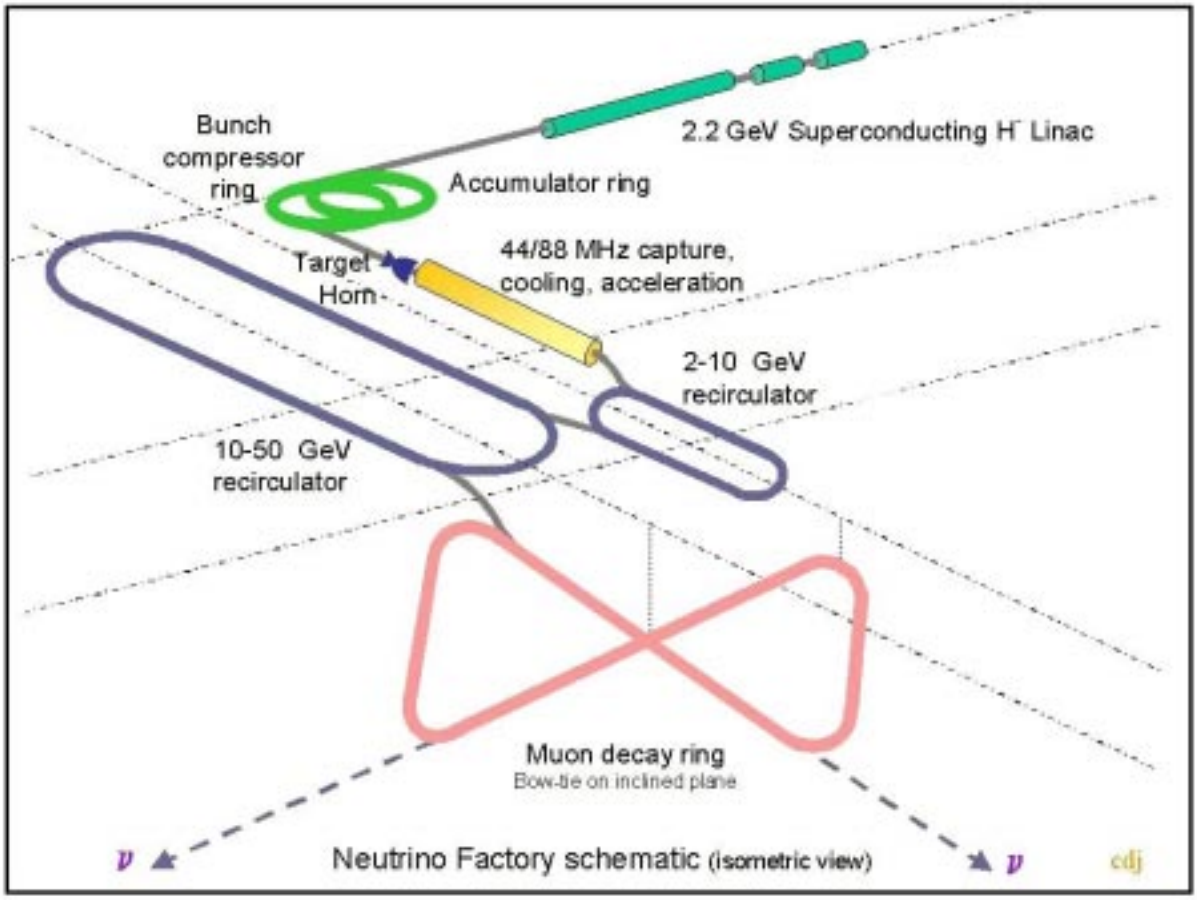

Fig. 2.1: Baseline scheme for a neutrino factory at CERN.

Table 2.1: Parameters of the proton beam for the CERN neutrino factory.

Parameter	Value	Source of constraint
Beam power (mean)	4 MW	Capability of the target
Repetition rate	75 Hz	High limit: power consumption of pulsed systems Low limit: intensity limitation in the accumulator/ compressor
Beam burst duration	< 6 μs	Circumference of the muon storage ring (single-turn injection)
Time between bunches	23 ns	Bunch rotation of muons
Bunch duration (r.m.s.)	1 ns	High limit: efficiency of bunch rotation of muons Low limit: uncertainty in decay time of pions

Until more detailed experimental data are available [11], the number of pions and muons that can be processed after the target is considered as proportional to the power of the proton beam and independent of its energy (for $T \geq 2$ GeV). A limit to this power is given by the target and pion capture set-up, which represents a technological challenge: 4 MW is the ultimate value that experts consider as feasible. A linac-based driver can easily deliver such a beam power, but in long pulses because of the limitation of the current per bunch at low energy.

The duration of the burst of muons has to be smaller than 6 μs to be injected in a single turn inside the 2000 m circumference storage ring. The duration of the burst of protons onto the target must then respect the same constraint. This cannot be obtained directly from a linac; an accumulator ring is necessary, where a few milliseconds of beam are stacked and later ejected in a single turn of a few microseconds.

The numerous pulsed high-power RF systems in the neutrino factory make the electrical power consumption a strong and increasing function of the repetition rate of the accelerator complex. However, at constant beam power, the beam intensity per pulse increases as the inverse of that rate, so that the lower limit is given by the intensity limitation in the accumulator. The value of 75 Hz has been selected as an acceptable compromise.

Short proton bunches are necessary to help reduce the energy spread of the muon beam by bunch (phase) rotation. The value of 1 ns r.m.s. which is required is difficult to achieve in a low-energy synchrotron because it needs a high longitudinal density to keep the total relative energy spread at an acceptable level (< 2%), and because of transverse defocusing due to the self-fields. This is achieved in the present scenario by limiting the number of protons per bunch to 3.3×10^8, using 140 bunches spaced by 23 ns.

2.1.2 Linac-based proton driver

Beam losses are a major concern for such high-power accelerators. To minimize radioactivation of the equipment and keep hands-on maintenance possible, the conventional limit of less than 1 W/m is deemed necessary during accelerator operation, which corresponds to a relative loss of 2.5×10^{-7} per meter at 2 GeV. In the accumulator and compressor, the total power of uncontrolled loss distributed over their 1 km circumference must not exceed 1 kW. This imposes stringent requirements on the design, and the selection of potentially loss-less schemes with large safety margins. Concerning injection and stacking in the accumulator, the solution is to use charge-exchange injection, sending H^- ions from the linac into the accumulator at the location of a stripping foil which strips the ions from their electrons.

In the accumulator, protons are captured in 140 out of the 146 RF buckets created by an RF system at 44 MHz. Capture losses and bunch emittance are minimized using gaps in the linac bunch trains, so that protons are always injected in a small area near the bucket centre. Moreover, six successive buckets are left empty to preserve a particle-free gap for the rise time of the ejection kicker. At the end of the accumulation process, the bunches have an r.m.s. length of 3.5 ns. The compression to 1 ns r.m.s. is achieved in seven turns (~ 23 μs) in a dedicated compressor ring equipped with 2 MV of RF at 44 MHz and 350 kV at 88 MHz.

The cascade of machines along the beam path, and the evolution of the time structure of the beam are represented in Fig. 2.2. The beam delivered to the target by the compressor satisfies the requirements listed in Table 2.1, with the complementary characteristics listed in Table 2.2.

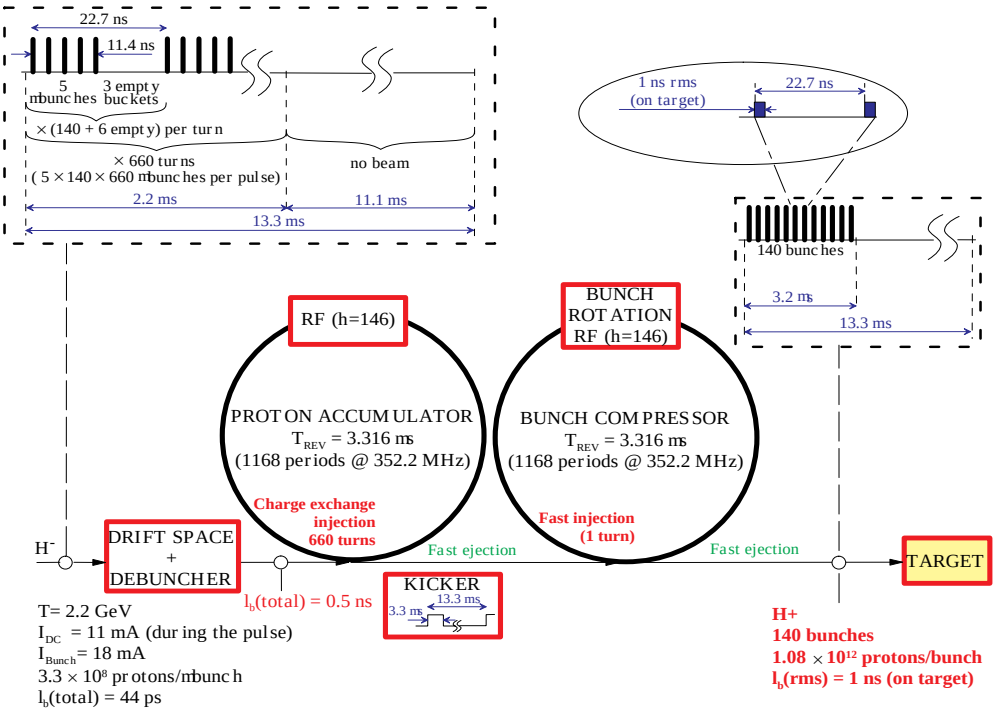

Fig. 2.2: Beam time structure in the proton driver machines.

Table 2.2: Characteristics of the beam from the proton driver.

Pulse duration	3.18 μs
Time between bunches (RF frequency)	22.7 ns (44.025 MHz)
Number of bunches	140
r.m.s. bunch length	1 ns
Number of protons per bunch	1.06×10^{12}
Number of protons per pulse	1.49×10^{14}
Total longitudinal emittance ε_l	0.1 eVs
Transverse r.m.s. emittance $\varepsilon^*_{h,v}$	50 μm

2.1.3 Linac specifications for the proton driver

The SPL is in fact accelerating H^- ions. Its characteristics for the proton driver are brought together in Table 2.3.

The fine time structure of the beam is obtained with a chopper, a fast transverse deflector (2 ns rise-time) at 3 MeV kinetic energy, sending 40% of the bunches onto a dump.

Longitudinal space-charge in the accumulator necessitates an increase in the length of the linac bunches from their 'natural' value of 44 ps, up to 0.5 ns. Therefore a debunching section is added at the end of the linac which brings the advantage of reducing the beam-energy spread and jitter.

To reach the required longitudinal density in the accumulator bunches, tight requirements are made on the stability of the beam energy. This is especially delicate for the SPL because of the high Q and small bandwidth of the superconducting cavities, which makes them prone to detuning as a result of mechanical vibrations. Design choices (RF power distribution, feedback systems, etc.) are made to minimize the effective modulation of the amplitude and phase of the accelerating field and limit the jitter in beam energy.

Table 2.3: SPL beam characteristics for the proton driver

Ion species	H^-
Mean beam power	4 MW
Kinetic energy	2.2 GeV
Repetition rate	75 Hz
Pulse duration	2.2 ms
Number of protons per pulse (mean current within a pulse)	1.5×10^{14} (11 mA)
Beam transverse emittance (normalized)	0.6 mm r.m.s.
Bunch frequency (time between bunches)	352.2 MHz (2.84 ns)
Time structure of the pulse	[140 × (5 consecutive + 3 missing) bunches + 6 × 8 missing bunches] × 660 revolutions in the accumulator
Number of protons per bunch	3.3×10^8
Total bunch length at the accumulator input (at the SPL end)	0.5 ns (44 ps)
Total energy spread at the accumulator input (at the SPL end)	0.4 MeV (6 MeV)
Peak-to-peak energy jitter during a pulse at the accumulator input (pulse-to-pulse jitter)	0.2 MeV (4 MeV)

2.2 PS injector

2.2.1 Principle

Modifications limited to the hardware handling the injection process are sufficient for the PS to benefit from the SPL beam. These have been described in the previous report [3] and mostly involve removing the present 1.4 GeV fast injection system and replacing it with a charge-exchange injection set-up in straight section 78.

The SPL will supply H^- to the PS and ISOLDE according to the principle shown in Fig. 2.3. Most SPL beam pulses are sent to the accumulator of the neutrino factory at the 75 Hz rate. The ISOLDE facility is fed with a short beam burst from the end of these pulses. The mean current received by the target can be changed from 2 to 100 μA by changing the length of the ISOLDE beam burst from 2.4 to 120 μs. Some pulses (~ 1 per second, or 1 in 75) are sent to the PS for the needs of the CERN complex of high-energy accelerators. The duration of these pulses and their fine time structure are completely defined by the PS needs for each specific cycle in the PS supercycle.

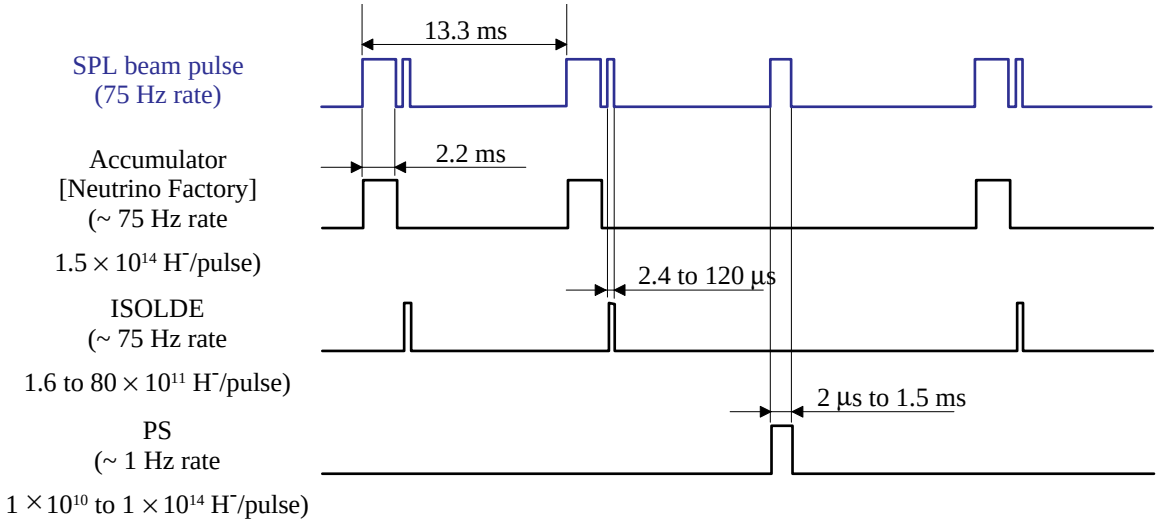

Fig. 2.3: Principle of SPL sequencing.

2.2.2 Beam dynamics in the PS

The main limitation of the PS machine for high-intensity, high-density beams comes from space-charge detuning at low energy [4], given by:

$$\Delta Q_{x,y} \propto \frac{I_p}{\varepsilon^*_{x,y}(\beta\gamma)^2}, \tag{1}$$

where $\Delta Q_{x,y}$ is the incoherent (self field) detuning in the horizontal (x) and vertical (y) planes, I_p is the bunch peak current, $\varepsilon^*_{x,y}$ are the normalized emittances (the ratio $I_p/\varepsilon^*_{x,y}$ is the beam brightness), and β and γ are the usual relativistic factors. As an injector for the PS machine, replacing the present Linac2 and PS Booster, the SPL increases the minimum energy in the PS from 1.4 to 2.2 GeV, which reduces the space charge detuning $\Delta Q_{x,y}$ by a factor of two. The beam brightness I_p/ε^* can then be doubled while keeping the same $\Delta Q_{x,y}$.

H^- injection allows control (by painting) of the particle density in the transverse phase planes. The fast chopper at the SPL front end gives the possibility to optimize the population of the longitudinal phase plane, and in particular to use the harmonic number and the number of bunches that are best matched for each specific PS beam user.

2.2.3 Performance improvement for the LHC

A higher space-charge tune shift than in the nominal scheme for the LHC using the PSB [13] can be tolerated because the beam stays a much shorter time at the injection energy (the 'ultimate' intensity is accumulated in ~ 100 turns or 200 ms instead of 1.2 s when using the PSB). Combined with the gain resulting from the higher injection energy (see Section 2.2.2), we extrapolate from a previous study [4] that the ultimate intensity for the LHC can probably be achieved with a transverse emittance of 1 μm (rather than the present 3 μm). The brilliance, at the PS exit, will then be three times higher than nominally specified [13]. The main beam parameters at the injection energy in the PS are summarized in Table 2.4.

Table 2.4: Tentative parameter list of an LHC 'ultimate beam' at low energy in the PS machine at T = 2.2 GeV, V_{RF} = 50 kV, h = 21 (only 18 buckets filled), N_t = *(h-3)* N_b = 1.5×10^{13} p/pulse.

N_b [$\times 10^{11}$]	ε_l [eVs]	τ_b [ns]	ε_x* [μm]	ε_y* [μm]	ΔQ_x	ΔQ_y
8.3	0.6	60	1	1	0.24	0.39

The fast PS filling process also has the advantage of reducing the PS cycle length from 3.6 s to 2.4 s which shortens the injection flat-top in the SPS from 7.2 s to 4.8 s and reduces the LHC filling time accordingly.

2.2.4 Performance improvement for the SPS fixed-target physics

With the same arguments as for the LHC beam (see Section 2.2.3), a PS beam of, for example, 4×10^{13} protons, can be accumulated in transverse emittances of 4 μm in the horizontal and 6 μm in the vertical plane (at present 17 μm and 7 μm, respectively) while keeping the tunes shifts below 0.3. This will eliminate one of the major limitations for achieving a higher intensity (e.g. for the CNGS beam) in the SPS machine which comes from the limited SPS transverse acceptances at injection energy. The estimated parameters for this beam at injection energy in the PS are given in Table 2.5.

Studies have started for a new type of 'Continuous Transfer' extraction aimed at reducing the high losses presently related to this operation and giving the possibility to increase beam intensity without irradiating the accelerator's equipment more.

Table 2.5: Tentative parameter list of a high-intensity beam for the SPS at low energy in the PS machine at T = 2.2 GeV, V_{RF} = 50 kV, h = 16, $N_{t=}$ h N_b = 4×10^{13} p/pulse.

N_b [$\times 10^{12}$]	ε_l [eVs]	τ_b [ns]	ε_x* [μm]	ε_y* [μm]	ΔQ_x	ΔQ_y
2.5	0.8	75	4	6	0.21	0.21

The high-intensity performance, however, also depends on other collective effects. They are strictly dependent on the intensity and will probably limit the total intensity gain to about 30%.

2.2.5 Performance improvement for the high-intensity beams used by nToF and AD

Keeping acceptable tune shifts (0.28 in both planes), the nToF bunch intensity can be increased to 10^{13} p (0.7×10^{13} at present) by adjusting the horizontal and vertical emittances to 6 and 8 μm respectively. Note that for this beam the longitudinal emittance should not be made smaller than 2.8 eVs to avoid beam break up instabilities at transition and not higher than 3 eVs to maintain a short bunch at extraction.

The intensity of the antiproton beam could also be brought up to 2×10^{13} p/pulse (at present 1.5×10^{13} p/pulse).

2.2.6 Other advantages and potential improvements

The high proton flux and the fast cycling rate of the SPL decouples the PS and the ISOLDE operations (Fig. 2.3). The PS does not compete with ISOLDE for particles from the injectors, in contrast to the present situation with the PSB.

Using the SPL as the injector, the PS is no longer linked to the present linac and PSB repetition rate (i.e. multiples of 1.2 s), and in principle, magnetic cycles of 'any length' can be envisaged. This should bring some gain in the duty factor of the PS by reducing the dead time between cycles. However, a significant improvement can only be achieved if the dB/dt in the bending magnets is noticeably increased. Since magnet isolation limits the maximum voltage acceptable on the coils, splitting the magnets into two strings and changing the power supplies accordingly could be envisaged to practically double the PS repetition rate. In this case the maximum RF voltage also has to be upgraded accordingly.

2.3 Second-generation Radioactive Nuclear Beam facility at CERN

NuPECC and the leading European research facilities have set up a Research and Technical Development (RTD) project, called EURISOL, intended for the preliminary design of a truly second-generation facility based on the Isotope Separation On Line (ISOL) approach [14,15]. Since the technology on targets and ion sources for the production of radioactive ion beams at CERN is by far the most advanced, it is natural to consider the idea that a future second-generation radioactive nuclear beam facility could be located at CERN. The proposed linac should eventually allow the increase of the intensity of secondary radioactive ions beams by a factor of 100 to 1000 compared to the present PS-ISOLDE facility. A conceptual plan of the facility is shown in Fig. 2.4. This laboratory will meet the demands of a wide science programme covering solid state physics, biophysics, nuclear astrophysics, studies of fundamental symmetries and interactions, and a full programme on structure and reaction studies of atomic nuclei very far from the valley of beta stability.

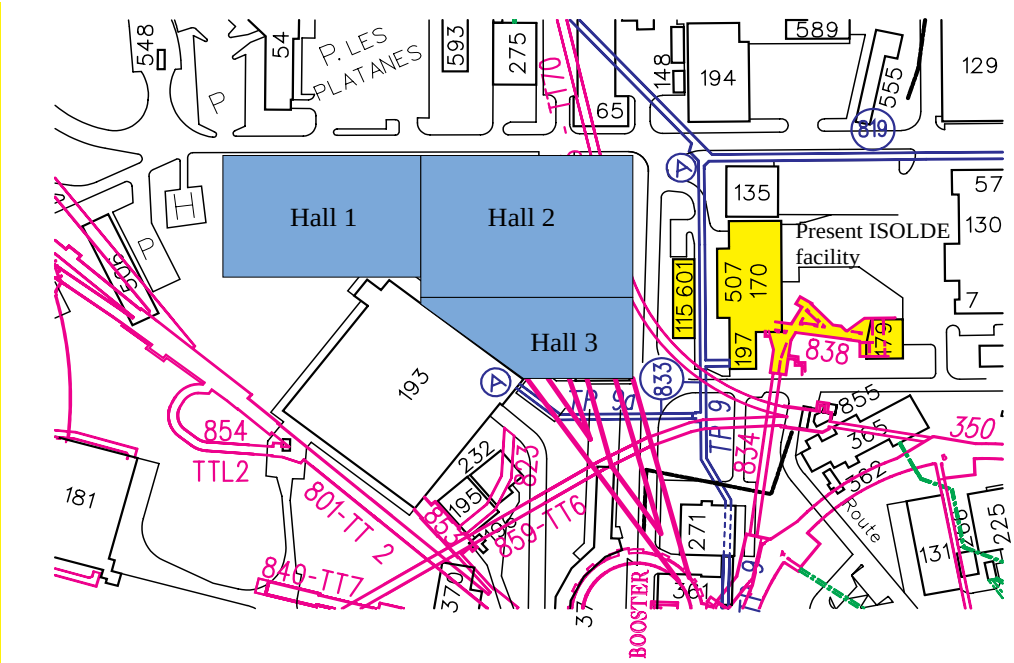

Fig. 2.4: A conceptual plan of where the future CERN second-generation RNB facility could be located. Hall 1 would hold the storage ring complex and Hall 2, the post-accelerator and the multi-segmented detectors. In Hall 3 a class A laboratory for handling radioactive targets would be housed. The three target stations would be accessed directly from Hall 3, thus avoiding any unnecessary transport of radioactive material on the site.

An important feature of a linac-based proton driver is the high repetition rate resulting in a lower peak intensity (DC like) of the proton beam than at the present PS Booster ISOLDE facility. An option to run the linac at lower energies than the nominal 2.2 GeV is of the highest importance for the CERN second-generation RNB facility. Several studies have recently been performed [16] of the energy dependence of the nuclear cross-sections using cascade calculations. The theoretical results have partly been verified at the PS Booster ISOLDE. They show a strong energy dependence for the optimum production cross-section for typical ISOLDE targets, with the optimum energy ranging from as low as 100 MeV to at least the full 2.2 GeV linac energy.

The driver beam will be transported to both the existing ISOLDE facility, and a new target area, which will be situated in the region of the present beam dump for the PS Booster. A first feasibility study, considering only radiation protection issues [17], shows that the present ISOLDE facility could accept up to a maximum of 10 μA of proton beam. The target area for a second-generation RNB facility will have to be located underground to permit proton beam currents of at least 100 μA, which is the present estimated maximum beam current tolerable on thick ISOL-type targets. The possibility of receiving a pulsed proton beam from the PS, the neutrino factory beam compressor, or a chopped SPL beam with pulses of roughly a millisecond length, would be of interest. Such a beam would permit the physics community to continue taking advantage of the techniques developed at the pulsed PS Booster ISOLDE facility.

The new target area will consist of two parallel target stations for the production beam. The stations will be made with independent access to permit push-pull operation between them. A third target station will be provided for pure development work, including that for the neutrino factory targets.

There are plenty of ideas for the target and ion sources for a second-generation RNB facility. Many of the ideas have already been probed by some preliminary feasibility tests, but so far there has been no systematic major research effort in this domain. The time has now come to give this field a real boost, and this is now being undertaken within the EURISOL Collaboration started by NuPECC. The study is financed by the European Union and an outline of the possible target and ion sources for a second-generation RNB-type facility has been published in a recent report [15]. The choice of material and the importance of the internal transport mechanisms for high-intensity targets has been studied in connection with the development of the target [18] for the proposed SIRIUS facility at the Rutherford Appleton Laboratories. This study is of great importance for a second-generation RNB facility and will be pursued further. Among the ion sources to be studied (besides the standard ISOLDE ion sources) are a compact ECR ion source and further development of the ISOLDE LASER ion source.

A second-generation RNB facility at CERN should have three experimental sections, according to the energy of the radioactive ion beam and the type of instrumentation used in the experiments. There is the low-energy area, where ions with energies up to 100 keV are used; the area where ion energies up to and above the Coulomb barrier and up to nearly 100 MeV/u are used; and the storage and cooler ring (300 MeV/u) area, possibly connected to an electron ring (100–400 MeV) for electron-ion collider experiments (a GSI scenario to be optimized for our physics and ions). In addition, the possibilities provided by the proximity of an antiproton source and an intense source of muons should be investigated as novel approaches for characterizing the structural features of exotic nuclei, such as their charge and mass density distributions via measurements on hyperfine splitting and isotope shifts. The future facility will have to be a multiuser facility with the potential to serve several experiments simultaneously. In a limited way, the present ISOLDE facility already operates in this way.

3. CHOICE OF PARAMETERS AND OVERALL DESIGN OF THE LINAC

The linac parameters must be defined to suit its three main users, the accumulator/compressor ring for the Neutrino Factory, the PS ring for the LHC and other high-intensity fixed-target applications, and a second-generation radioactive-beam facility for ISOLDE. However, the Neutrino Factory will determine the main linac parameters, being by far the most demanding user in terms of particle flux and time structure of the beam pulses.

Beam simulations for the Neutrino Factory layout indicate that 10^{21} neutrino decays per year in the muon decay ring can be provided by a proton beam power on target of 4 MW [8]. Simulations of particle production in the target show that the number of generated pions is approximately proportional to beam power for energies ≥ 2 GeV, indicating that a pulsed linac in this energy range with about 2 mA average current would constitute an appropriate proton driver for a Neutrino Factory. An injection energy of about 2 GeV is also perfectly adequate for accelerating higher intensities in the CERN PS, with a substantial decrease in the space-charge tune shift at injection with respect to the present 1.4 GeV injection from the PS Booster.

The definition of the final linac energy, as for the pulsing parameters (pulse repetition rate and length) is the result of a compromise between many requirements. Although by adding up all the available LEP cavities an energy of about 3 GeV could be reached, a final linac energy of 2.2 GeV has been selected slightly above the pion production threshold, in order to release to some extent the space-charge problems in the accumulator without an excessive increase in the length and cost of the machine.

In the same way, a linac mean current during the pulse of 11 mA has been selected as a compromise between many factors. A lower current reduces the number of klystrons needed by the superconducting section, at the cost of an increase in the complexity of the power distribution network and in the sensitivity of the linac to vibration errors in the superconducting cavities. It would also lead to a longer linac pulse, increasing the number of turns required at injection in the accumulator and the time for dangerous instabilities to develop. In contrast, a higher current improves the power efficiency of the room temperature section and reduces the number of injected turns, but also introduces space-charge problems at the low-energy linac end and increases the RF power to the superconducting section, requiring a higher number of klystrons. A current of 11 mA is a good compromise between these factors and has the additional advantage that no modifications are needed to the input couplers of the LEP cavities.

The selection of beam power, energy, and pulse current determines the linac duty cycle, 16.5% in this case. The choice of the repetition rate is determined by the superconducting cavities. In a superconducting linac the cavities are largely overcoupled, and the rise time of the fields in the structures is of the order of a few milliseconds. In order to establish the field in the cavities, a large amount of RF power is reflected from the couplers and has to be absorbed into the loads. A pulsed superconducting linac is therefore more effective in terms of the conversion of mains power into beam power at low repetition rates. On the other hand, a lower repetition rate means a longer beam pulse, which could dangerously increase the number of turns for accumulation in the following ring. A repetition rate of 75 Hz and a pulse length of 2.2 ms have therefore been selected, corresponding to 660 injection turns into the accumulator. Simulations of injection into the accumulator indicate that this number of turns is still acceptable [10], whilst the repetition rate, 3/2 of the mains frequency, remains below the 100 Hz mechanical oscillation frequency of the LEP cavities.

A chopper in the low-energy section is an essential feature of any high-intensity linac injecting into a circular machine. In the present design, the chopper is a travelling wave structure placed at 3 MeV energy between two RFQs and has to provide a rise time of 2 ns to avoid partially-filled linac buckets. The time structure of the chopped beam is determined by the RF accumulator. In the present scheme, the accumulator bucket at 44 MHz is filled by five linac bunches, spaced by three empty buckets (Fig. 3.1). Including the space left in the linac pulse for the rise time of the ejection kicker (six empty accumulator buckets every 146) the overall chopping factor, i.e. the fraction of beam removed at the chopper position, is 40%. The corresponding mean bunch current in the linac (averaged during a

linac RF period corresponding to a full bucket) is 18.5 mA, which is below the limits of a space-charge dominated beam. The ion source has to provide a current of about 25 mA, a value well within reach for present H^- sources. The main design parameters of the 2.2 GeV linac are summarized in Table 3.1.

Table 3.1: Main linac design parameters.

Particles	H^-
Kinetic energy	2.2 GeV
Mean current during pulse	11 mA
Repetition frequency	75 Hz
Beam pulse duration	2.2 ms
Number of particles per pulse	1.5×10^{14}
Duty cycle	16.5%
Mean beam power	4 MW
RF frequency	352.2 MHz
Chopping factor	40%
Mean bunch current	18.4 mA
Transverse r.m.s. emittance (norm.)	0.6 μm

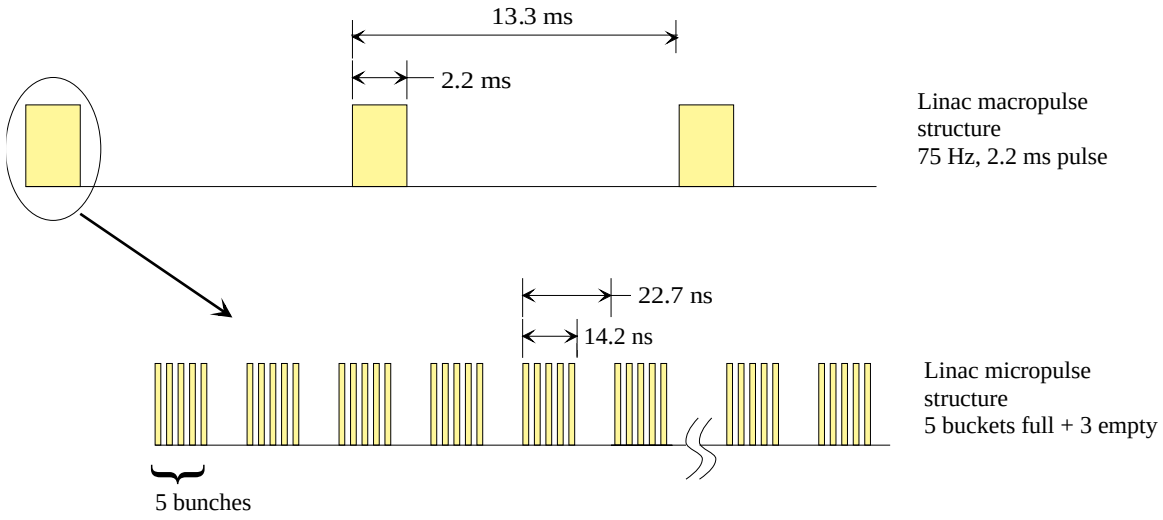

Fig. 3.1: Time structure of the linac pulses.

The RF frequency for the high-energy part of the linac is determined by the existing LEP cavities and klystrons at 352 MHz. For the new superconducting cavities that have to be constructed for a beta lower than unity, the choice of the same frequency allows us to take advantage of the CERN niobium sputtering fabrication technique and to re-use couplers and cut-off tubes recuperated from LEP units. For the structures at room temperature, this frequency offers a good compromise between the large

dimensions and easier fabrication tolerances of lower frequencies, and the better shunt impedance of higher frequency structures. The RF cavities can thus have the same frequency all along the linac, simplifying the RF system and avoiding frequency jumps which are dangerous for the beam dynamics. The frequency of 352.2 MHz also lies at the boundary between klystron and tetrode amplifier technology, providing additional flexibility in the design of the RF system and the possible use of both types of power sources. For the sections with high-power cavities (the room temperature structures and the high-energy part of the superconducting linac) the 1 MW klystrons of LEP are well suited, with simple (from one to six cavities per klystron) RF distribution networks. For the cavities of the low-beta superconducting sections, where the power per cavity is lower and the beam is very sensitive to errors in cavity field, it is more convenient to use 100 kW conventional tetrode RF amplifiers, each one feeding a single cavity.

The transverse emittance of the linac must be carefully controlled for two reasons, to minimize losses and to achieve the high beam brightness required by the LHC. An r.m.s. normalized emittance of $0.2\,\pi$ mm mrad is considered to be a reasonable goal for the H^- source, whilst in order to keep a large safety margin, a design emittance of $0.6\,\pi$ mm mrad has been adopted at the input of the accumulator ring. An intermediate design emittance of $0.4\,\pi$ mm mrad has been assumed for the different linac sections.

The need to minimize space-charge effects in the accumulator imposes the additional constraint that the total bunch length at injection in the accumulator has to be larger than 0.5 ns. Stretching the bunch length from the 40 ps at the linac exit is achieved by two bunch rotation sections made of LEP cavities in the transfer line, the first at the end of the linac to increase the energy spread and to accelerate the natural debunching of the beam, and the second before injection to minimize again the energy spread. Whilst the individual bunches have a total energy spread of 0.5 MeV, the accumulator can accept pulse-to-pulse variations of the mean bunch energy inside 4 MeV. Oscillation of the beam energy due to vibrations of the superconducting cavities have to be kept inside these limits by means of feedback loops. The requirements for the linac beam in the longitudinal plane are summarized in Table 3.2

Table 3.2: Parameters of the linac beam in the longitudinal plane.

Longitudinal r.m.s. emittance	$0.6\,\pi$ ° MeV
Bunch length at accumulator, total	0.5 ns
Energy spread at accumulator, total	0.5 MeV
Energy jitter at accumulator, between pulses (max.)	±2 MeV

A major concern in the design of the linac is the reduction of beam losses, in order to avoid activation of the machine and irradiation of the environment. The main constraint is to maintain losses below the commonly agreed limit for hands-on maintenance of 1 W/m, corresponding for this design to a relative loss per metre of 2.5×10^{-7} at the high-energy end, or 0.5 nA/m. The shielding is dimensioned to keep radiation at the surface below the limit for public areas, assuming a 1 W/m loss in the machine. While losses caused by collisions with the residual gas and by H^- stripping in the magnetic field can be maintained below the activation limit, a careful beam dynamics design is needed to avoid the formation of a particle halo that would finally be lost in the linac or in the transfer line. The basic principles in the design of the linac were to vary smoothly the focusing parameters, to match carefully the beam at the transitions between sections, to avoid crossing of resonances and finally to prefer, wherever possible, large apertures in spite of some reduction in shunt impedance. Another important principle is to concentrate the remaining unavoidable losses on well-localized shielded dumps, as is the case for the cleaning of the beam before injection into the accumulator, where collimation stripping foils send the stripped particles to dedicated dumps.

The overall layout of the linac is shown in Fig. 3.2. After the source, the beam extracted at 45 keV enters a first RFQ which boosts the beam energy up to 3 MeV. The chopper is placed in this position, inside a transport line that provides space for extracting the chopped beam to a dump and rematches the beam to the acceptance of a second RFQ. The chopper energy of 3 MeV is a compromise between the unavoidable beam neutralization in a chopper line at lower energy (before the RFQ) and the high voltage required to deflect the beam at high energy (exit of the RFQ section).

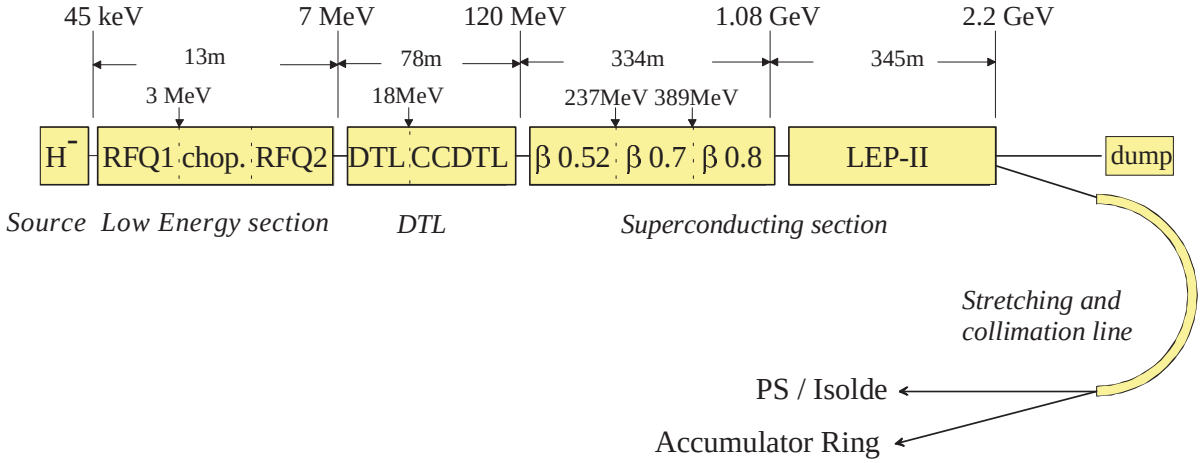

Fig. 3.2: Schematic layout of the linac.

A second 4 m long RFQ increases the energy to 7 MeV, an energy well within reach for an RFQ starting at 3 MeV and equipped with a standard 1 MW power source. The choice of this high injection energy into the following Drift Tube Linac (DTL) facilitates the design of the critical drift tubes and quadrupoles at its low-energy end. The DTL is made of two sections, the first one with two conventional Alvarez tanks up to 18 MeV, and the second that goes up to 120 MeV with shorter 2-gap tanks and external quadrupoles. At this energy, considered at the moment to be the lowest achievable with elliptical superconducting cavities, a short matching line transfers the beam into the superconducting linac. Three sections made of superconducting cavities designed for a beta of 0.52, 0.7 and 0.8 increase the beam energy to about 1 GeV, where the section equipped with LEP cavities starts, up to the final energy of 2.2 GeV. A transfer line brings the beam to the accumulator and to the PS. This line accomplishes two other functions: stretching the bunch length before injection in the accumulator, and providing collimation transversally and in energy. A 50 kW dump for setting the beam up at a low repetition rate is foreseen in a straight line at the end of the linac, whilst a common 4 MW dump for the linac, accumulator, and compressor is foreseen in an area external to the ring tunnel, connected to the injection point by a short transport line.

An additional design constraint could come from the ISOLDE requirement for different beam energies. Pending a more advanced definition of the ISOLDE requirements, this option has not been included in the present design. However, different options have been analysed, and a viable solution would be to extract a fraction of the beam pulse by means of fast kickers placed at the transitions between different linac sections (120, 240, 390 and 1000 MeV). The beam would be sent into an ISOLDE beam line running parallel to the linac from the 120 MeV energy point.

The main layout data are given in Table 3.3. The overall linac length is 799 m, and it requires 44 klystrons and 79 tetrode amplifiers. A total of 116 unmodified LEP cavities are used, i.e. 43% of the total inventory of 272 cavities.

Table 3.3: Linac layout.

Section	Input energy (MeV)	Output energy (MeV)	Number of cavities	Peak RF power (MW)	Number of klystrons	Number of tetrodes	Length (m)
Source, LEBT	–	0.045	–	–	–	–	3
RFQ1	0.045	3	1	0.4	1	–	3
Chopper line	3	3	5	0.3	–	5	6
RFQ2	3	7	1	0.5	1	–	4
DTL	7	120	100	8.7	11	–	78
SC – reduced β	120	1080	122	10.6	12	74	334
SC – LEP	1080	2200	108	12.3	18	–	345
Debunching	2200	2200	8	–	1	–	26
Total			345	32.8	44	79	799

4. DESIGN PROPOSAL

4.1 Source and low-energy beam transport (LEBT)

Today there are two major types of H^- sources, surface and volume sources. A review of their technical principles, advantages and disadvantages is given in Ref. [19]. Not all of these particle sources are well suited for accelerator operation where intensity, short- and long-term stability, reliability and easy maintenance are of major importance. Existing sources suffer from a number of problems. In many cases caesium is used to get high H^- currents, but caesium pollution of the beam can give rise to RF voltage-holding problems in the following accelerator structures. A possible solution is the use of rare gases to increase ion yields [20].

The requirement of an 18.4 mA, 2.2 ms beam pulse out of the linac could be met with an extracted beam of around 30 mA out of the source. This would give a good margin for stripping losses in the LEBT and some margin for beam shaving to reduce aberrations. In itself, this current is well within the reach of modern ion sources. However, the 75 Hz repetition rate puts this source into an entirely different class. Sources with caesium would probably have difficulty in maintaining an adequate caesium coverage (0.7 monolayers). Source cooling will become a major problem, especially for any permanent magnetic material (magnetic filters), and electron suppression/dump will need to be very effective to avoid major vacuum perturbations on long pulses.

Some sources use a porcelain-coated antenna inside the plasma chamber (e.g. the RF volume source at DESY [19]). The lifetime of this antenna is a major factor in the reliability of the source and would certainly become problematic at 75 Hz. There are several approaches to overcome this problem. One is the transformer-coupled plasma source [21]. Another is the ECR type of source [22, 23, 24]. Based on experience with positive ion ECR sources, the ECR source makes a good choice for stability, reliability and maintenance. However, existing sources can deliver only microamperes of H^- and for this reason a collaboration for the development of a new source based on the design of the CEA-Saclay SILHI source (a high-intensity proton source [25]) is considered. A conceptual design is shown in Fig. 4.1.

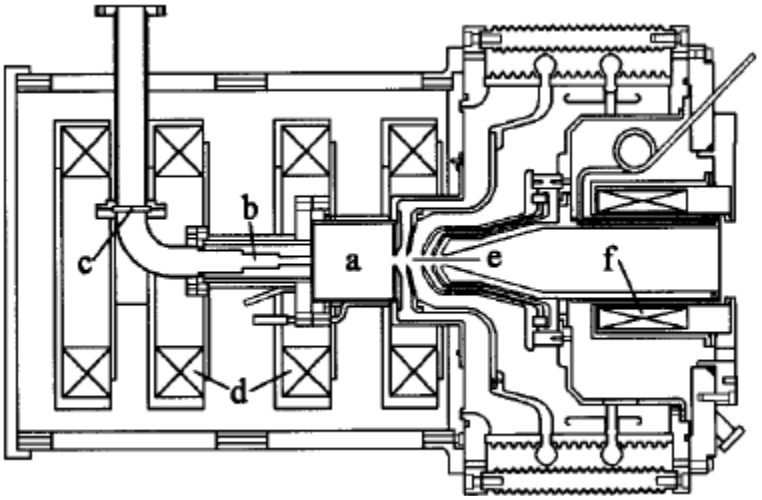

Fig. 4.1: A possible design for an ECR H^- source [25].

Commercial sources also exist, e.g. the Series 4 H^- source from AEA Technology, Culham [26]. This is a magnetically confined volume-type source with filament, but is only designed for 100 hours of CW operation.

The H^- beam extracted from the source contains not only the ions but also electrons and, depending on the source type, there can be many times more electrons than H^- which have to be

removed at low energies by electrostatic and dipole magnetic fields near, or in, the extraction region. Additionally the extracted beam has to be accelerated as quickly as possible because stripping losses of H^- occur mainly in the low-energy, high-gas-pressure region near the extraction region. Thus a sophisticated extraction system is needed [21]. Stripping losses would benefit from a high extraction voltage but this would increase the power deposited by electrons which leak through the electron sweeping system. Lower extraction voltages would require high-gradient structures which would complicate the sweeping system. Efficient pumping of the source extraction region would reduce stripping losses but this could be limited in effectiveness by the geometry of the electrodes needed for high gradient acceleration. A final consideration comes from the power needed from the high-voltage power supply. The inherent stored energy should be kept as low as possible suggesting a lower extraction voltage (around 45 kV), whereas the need for open high-gradient structures and limiting space-charge effects suggests around 90 kV. For reliability reasons, a voltage falling 10% below a commercial supply should be chosen. In the present design, where the extracted current would be about 30 mA and space-charge effects would not be too harmful, an extraction voltage of 45 kV is preferred.

In summary, at the moment some sources exist which in terms of peak and in some cases average current can fulfil the specific beam needs of our linac design (e.g. DESY, BNL and Frankfurt). Development is needed to produce a source with similar specifications but with a high stability and long-term reliability at high repetition rate. A considerable effort will still be needed to master the extraction process and high-voltage systems.

The source and the LEBT have to be considered together from the design stage. The basic choice for the LEBT will be between a magnetic and an electrostatic design. Two-solenoid LEBT designs as for the CERN RFQ2 injector [27] are well proven and allow a precise matching to the RFQ, leaving enough space in the line for beam diagnostics and other equipment. This type of LEBT is however subject to unpredictable levels of beam neutralization that can perturb the beam dynamics, increase the losses in the machine and introduce harmful beam resonances. Electrostatic beam transport (Einzel lenses) as in the BNL design for SNS [28] are exempt from neutralization problems, but require a sophisticated electrode design and do not leave any space for diagnostics before the RFQ. In both cases the LEBT must include an electron suppressor and a pre-chopper with rise time in the microsecond range, to reduce the load on the main chopper. The final decision on the LEBT design can be made only when the source and source extraction design have been finalized.

4.2 The RFQs

After the source and a LEBT section, the beam is accelerated to 7 MeV by a pair of RFQs at 352.2 MHz. Between the two RFQ stages, at 3 MeV energy, is situated the chopping line. The transition energy between the RFQs should be neither too low to limit the effect of the debunching nor too high to limit the voltage needed in the chopper.

In the design of the RFQs the maximum vane field has been limited to 1.6 Kilpatrick, to increase reliability and to limit power consumption without an excessive increase in the length of the RFQs.

For the more specific beam dynamics parameters, a special concern comes from the inevitable emittance increase in the chopping line. An acceptance of up to three times the nominal emittance from the source should absorb the emittance growth in the chopping line also at the maximum current of 40 mA (a safety margin of a factor 2 has been taken with respect to the SPL design current of 18 mA).

Both RFQs contain a dedicated ‘matching section’. The first RFQ has been equipped with an output matching section to get a round beam (Fig. 4.2) with a spot of about 3 mm. A chopping line composed of 352 MHz cavities and magnetic quadrupoles performs the 6-D rematching to the second RFQ. Figure 4.3 shows the variation of the parameters along the first RFQ. In the second one the modulation and the aperture are kept constant and the synchronous phase is linearly ramped up to the final value of –15°. The large design acceptance of the second RFQ should be sufficient to accommodate the emittance increase in the chopping line.

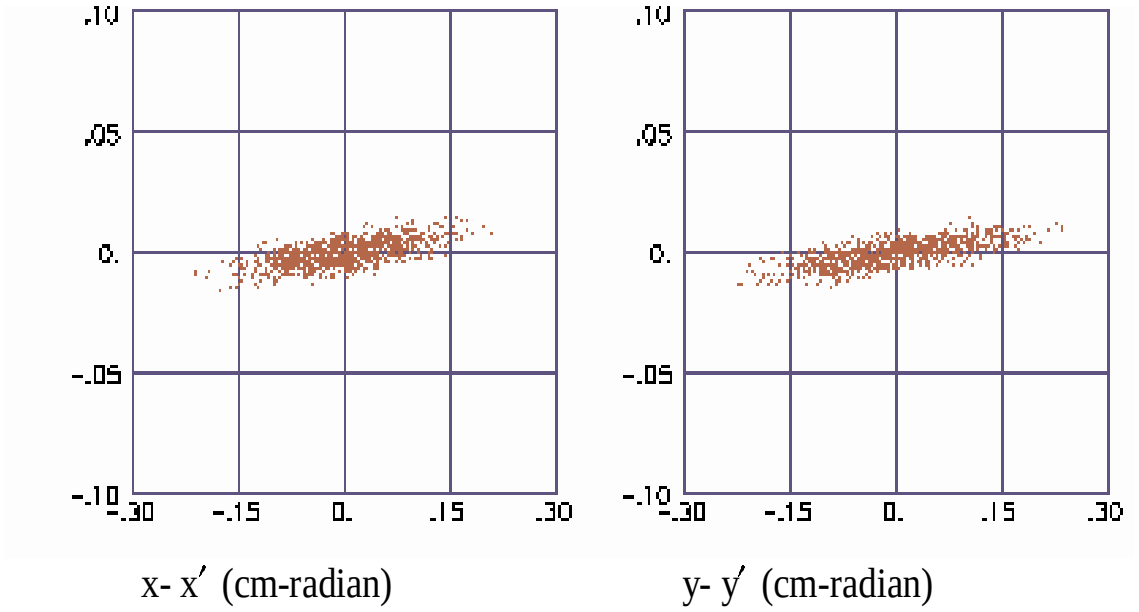

Fig. 4.2: Beam transverse phase space at the output of the first RFQ.

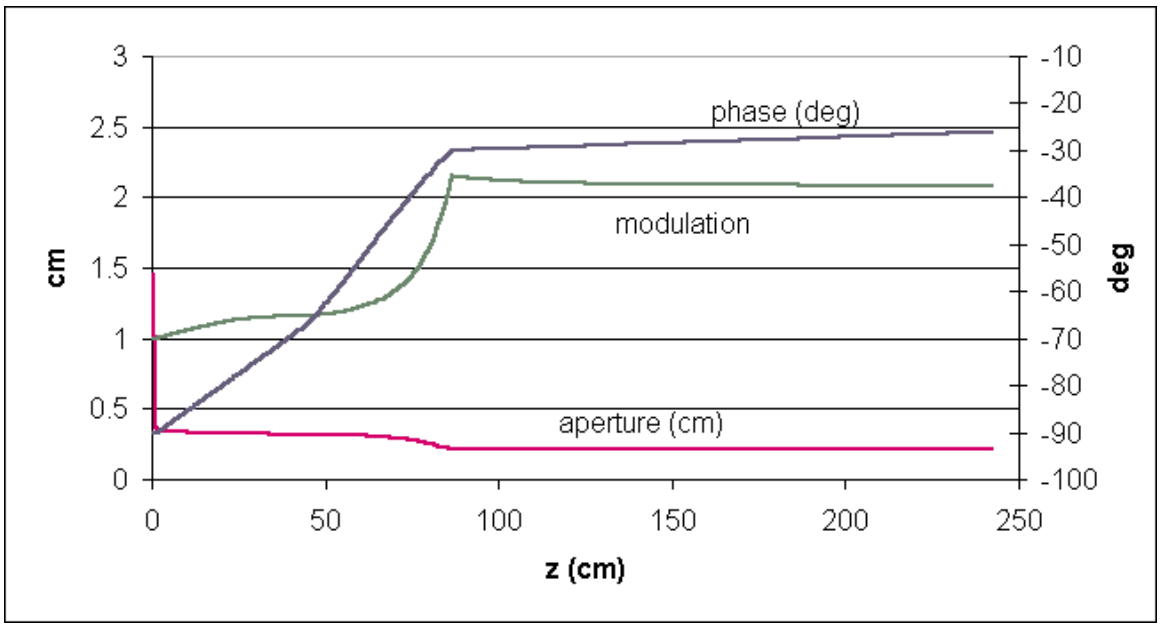

Fig. 4.3: Minimum aperture, modulation factor and synchronous phase along the first RFQ.

Table 4.1 summarizes the main RFQ parameters.

The RFQ cavity design can profit from the progress recently made in the field of high duty cycle 352 MHz four-vane RFQs by the construction of the RFQ for the Low Energy Demonstration Accelerator (LEDA) at LAMPF [29] and by the similar developments in Europe, at CEA Saclay [30] and at INFN-Legnaro [31]. The SPL duty cycle of 16.5% will relax the effects of thermal losses and guarantee a better stability of the cavity. To simplify the design of the structure, some of the cooling solutions of the 402 MHz 6% duty cycle RFQ being built at Berkeley for the SNS project could be

profitably adopted for the SPL RFQs [32]. The first RFQ is only two wavelengths long, enough not to have particular concerns for the longitudinal field stability. The second RFQ, however, has to be made of two resonantly-coupled segments. The power required is low enough to have only one RF window for each of the RFQs, without the need for complex waveguide distribution networks.

Table 4.1: Main RFQ parameters.

	RFQ1	RFQ2
Input energy	45 keV	3 MeV
Output energy	3 MeV	7 MeV
Frequency	352 MHz	352 MHz
Voltage	90 kV	90 kV
Maximum electric field	34 MV/m	34 MV/m
Length	2.6 m	3.9 m
Shunt impedance	60 kΩ m	60 kΩ m
Power	360 kW	500 kW
Average bore radius	0.34 cm	0.34 cm
Modulation factor (max)	2.15	2.15
Transmission (at 40 mA current)	95%	100%
Input emittance (r.m.s., norm)	0.2 π mm mrad	0.26 π mm mrad
Total normalized acceptance	3 π mm mrad	3 π mm mrad
Longitudinal output emittance (r.m.s.)	0.12 ° MeV	0.16 ° MeV
Output emittance (r.m.s., norm.)	0.2 π mm mrad	0.3 π mm mrad

4.3 Chopper

4.3.1 Chopper structure

The chopper is placed between the two RFQ tanks, which both operate at a frequency of 352.2 MHz. The transfer energy of 3 MeV avoids beam neutralization problems of a chopper placed before the RFQ, as well as the higher voltage required by a chopper placed at the DTL input.

In order to avoid partially filled buckets, the chopper rise time has to be shorter than the distance between bunches. For a maximum bunch phase length of ±45° at 352.2 MHz frequency, the chopper rise time has to be kept below 2.1 ns. Such short rise times can be obtained by using travelling-wave stripline structures, where the striplines are meander-folded in order to match the travelling-wave velocity to the beam velocity.

In the present design, a section of 1.2 m is available for the chopper. This section is split into two parts: the first with a total vertical aperture of 20 mm and 60 cm length, and the second with 30 mm total vertical aperture. For a deflection voltage of ±1 kV on either deflection plate (i.e. +1 kV on the upper plate and –1 kV on the lower one) one can expect at 3 MeV a deflection of 10 mrad from the first section and 7 mrad from the second one. Separate amplifiers are foreseen for each plate, delivering 1 kV peak deflection voltage each.

The Los Alamos National Laboratory (LANL) has developed such a chopper structure for the Spallation Neutron Source project, using notched striplines with separators to avoid coupling between adjacent lines. The LANL design is developed for a beam energy of 2.5 MeV, and a rise time of 2.4 ns. Glass microfibre PTFE composites are used to construct a suspended-substrate structure as shown in Fig. 4.4. A full-length (50 cm) prototype of this structure has been built and measured at LANL. Reflection measurements in the time domain show a structure rise time of about 1.5 ns and S-parameter measurements [33] indicate that harmful resonances occur only at higher frequencies (530 MHz and 1 GHz). Regarding the RF properties, this structure is perfectly suited for this linac. Looking at the mechanical and vacuum properties, no tests have been performed so far. The following points are important:

a) Outgassing of the organic material in vacuum must be tested.

b) The combination of substrate, spacer, and ground plate has to be tested for vacuum stability: there must be no material deformation due to the vacuum.

c) The distribution of heat losses must not lead to a deformation or any other possible damage to the structure. Estimates for the expected heat loss per plate, based on LANL transmission measurements on an existing device lead to an average power loss slightly less than 10 W for a ±500 V deflecting voltage and 30–40 W for the ±1 kV scenario.

d) RF measurements have to be performed in a vacuum tank in order to include the effects of the tank.

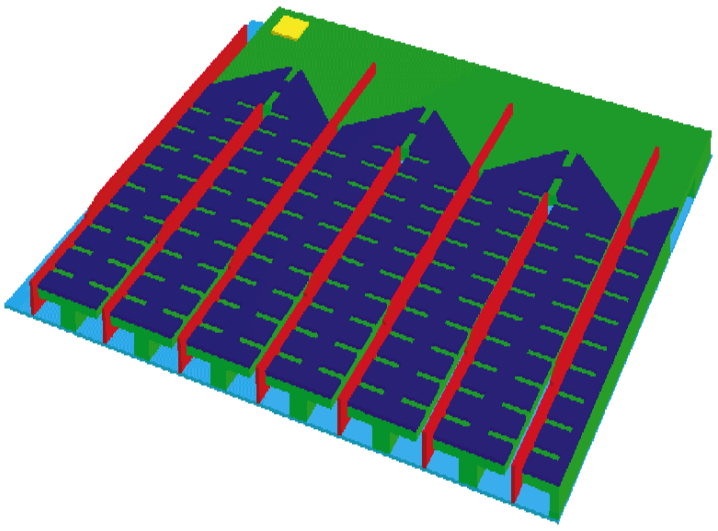

Fig. 4.4: The LANL chopper structure (the striplines are indicated; the beam comes from the left).

In case of problems with the PTFE material we propose the use of ceramics with good heat conductivity as substrate material. Because of its higher dielectric constant the shape of the meander structure has to be redesigned. If the implementation of the metallic spacers raises problems concerning the vacuum stability, the distance between the striplines has to be increased. Taking into account these measures, an alternative meander structure is considered. Figure 4.5 shows a 3-D simulation of the alternative chopper structure made with the code GdfidL [34]. Preliminary simulation results predict RF properties similar to the LANL design. The structure is mechanically easy to manufacture and makes use of well-known construction techniques and vacuum properties. Coupling between single striplines is avoided by the angular and tapered arrangement of the lines. Since all particles of a bunch should see the same deflecting field on axis, the velocity of the wave front varies along the structure. Owing to the tapering, the wave-front velocity is smaller than the particle velocity in the beginning and

bigger towards the end of the structure, so that the field irregularities on axis are simply integrated by the particles. Moreover, it should be taken into consideration that the meander-type deflecting structure has a significant frequency-dependent group velocity, which could lead to pulse shape distortion for long structures.

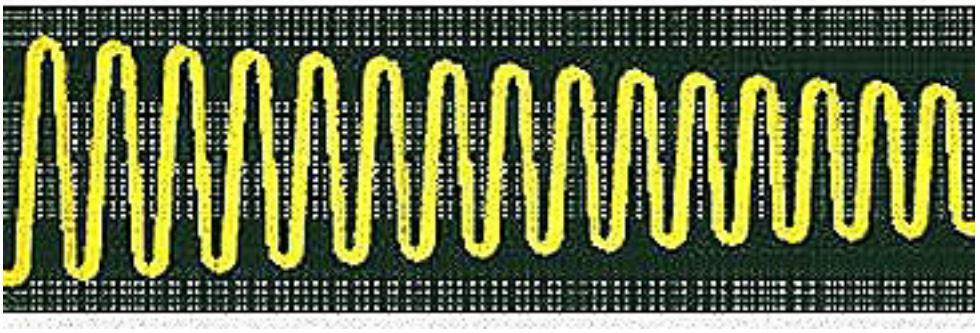

Fig. 4.5: 3-D simulation of an alternative chopper design (the beam travels from left to right).

Other possible alternatives for the substrate material could be VESPEL (similar to Kapton) or PEEK (Polyether Ether Ketone). Both materials can be metallized but they have less water absorption than Teflon and considerably less outgassing

Providing sufficient chopper voltage with a 2 ns rise time is a challenging task, therefore the amplifier voltage has been limited to 1 kV. Note that the rise time mentioned here is between 10% and 90% of the full voltage. Beam dynamics simulations will be done to study the influence of the remaining deflecting field on the particle motion. It should be noted that reducing the residual chopper field on the first bunch of the train going into the linac could be a considerable technical challenge.

4.3.2 Pulse amplifier

The chopper has to be driven with a pulse having the characteristics indicated in Table 4.2.

Table 4.2: Chopper pulse characteristics.

Pulse amplitude	1 kV
Load resistance	50 Ω
Rise and fall time (10% to 90%)	2 ns
Pulse length	10 ns to 270 ns
Repetition period	up to 44 MHz
Burst length	2.2 ms
Burst repetition rate	75 Hz

Many devices have been considered for this application and rejected because of their insufficient performance. Power MOSFETS get close to the voltage and current requirements but do not match the switching time limit. RF MOSFETS are very fast but their power and voltage limitations make them better suited for a driver stage than for providing the whole output signal. Avalanche-mode transistors can only provide a fraction of the required power with reasonable lifetime, while spark gaps, ignitrons and thyratrons do not permit high pulse repetition frequencies. It seems therefore that only vacuum tubes can switch the needed voltage and current with the required speed and repetition rate.

The pulser could be implemented as a linear amplifier but it seems more reasonable to go towards switching techniques and design a strongly non-linear device. The proposed configuration is based on a tube connected in common cathode configuration and directly driven by small, fast MOSFETS (Fig. 4.6). As for Power MOSFETS or IGBT switching, if the grid voltage is kept below conduction, the driver stage only needs to provide or remove the capacitive input charge. This allows the use of small, fast devices. Unfortunately these items only exist for low working voltages (50–70 V) and the choice is therefore limited to medium-power tubes.

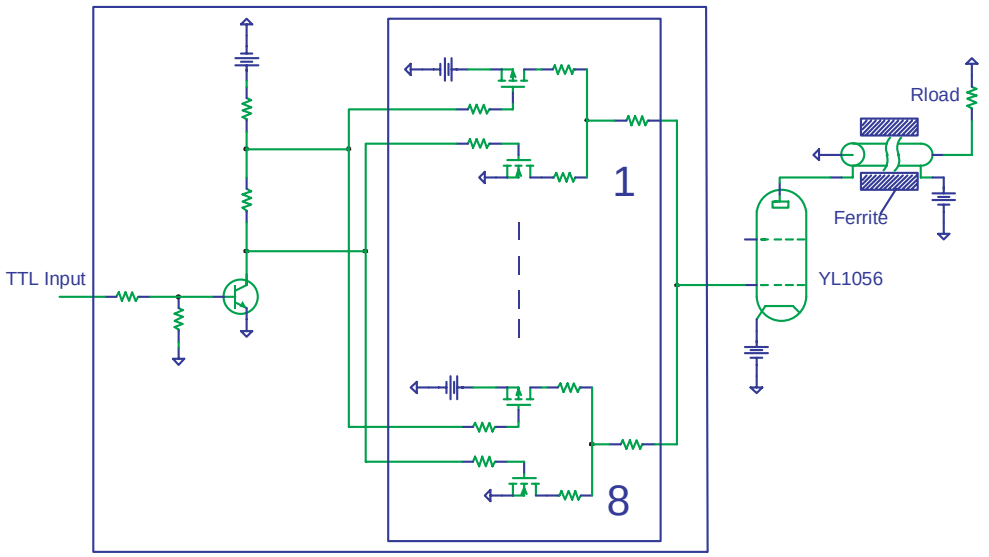

Fig. 4.6: Simplified schematic of the pulser.

The Siemens tetrode type YL1056 is a very fast device working up to 1 GHz. It can provide 250 V on 50 Ω and has been selected because the full plate current swing can be controlled with only 40 V grid-cathode voltage. The tube's main characteristics are listed in Table 4.3. Combining 16 of these units with standard RF techniques should not be a problem and would give the required 1 kV on 50 Ω.

Table 4.3: Main characteristics of YL1056.

Plate d.c. voltage	3.5kV
Plate dissipation	2 kW
Screen voltage	500 V
Screen Grid Dissipation	30 W
Control Grid Dissipation	5 W
I_a @ V_{gk} = 0 and V_a > 1 kV	5.5 A
I_a @ V_{gk} = – 40 and V_a > 1kV	0.2 A

g_m @I_a ~ 5 A and V_a > 1 kV	0.2 A/V
g_m @I_a ~ 0.5 A and V_a > 1 kV	0.055 A/V
I_s @ V_{gk} = 0 V and V_a = 1.5 kV	0.3 A
C_{gk}	42 pF
C_{gs}	60 pF
C_{ag}	0.05 pF
C_{as}	8.4 pF

Detailed simulations have been carried out on the proposed circuit, which predict rise and fall times within 2 ns and indicate that the required performance could possibly be achieved by mixing solid-state and vacuum tube technologies [35]. Figure 4.7 shows the calculated voltage pulse for a single amplifier module (250 V) operating on a 50 Ω load. For 500 V four such modules have to be

combined and for 1 kV one needs 16 modules. It must be noted that the active devices are pushed close to their technological limits and real prototyping is essential.

Particular attention has to be paid in mixing low-voltage MOSFETS with high-voltage power tubes. Moreover, because of a.c. coupling of the different units, d.c. restoration will be required on the load resistance, adding extra complexity to the pulser.

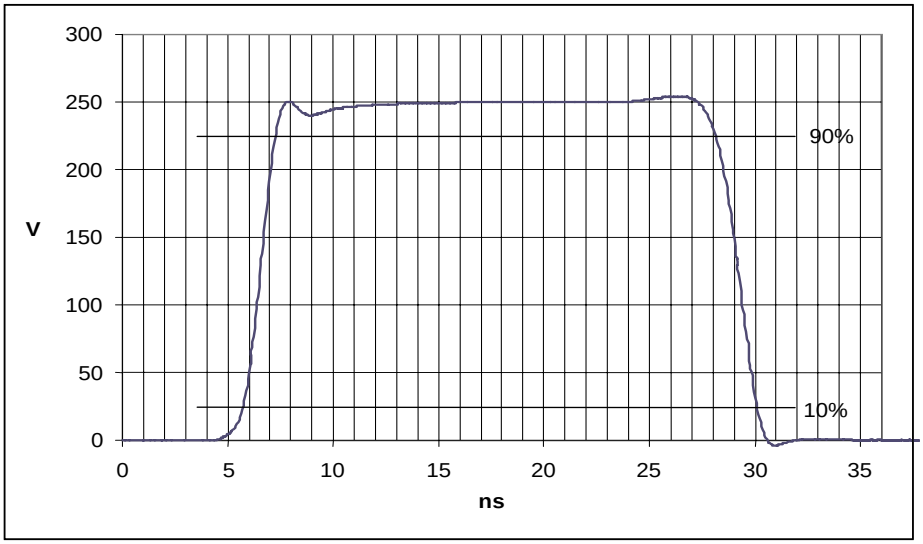

Fig. 4.7: Simulated output pulse for a single amplifier module.

4.3.3 Chopper line

The Medium Energy Beam Transport (MEBT) line, which includes the chopper, is meant to match the beam to the chopper, separate the chopped and unchopped beam, and finally rematch the beam to the acceptance of the second RFQ.

The SPL chopper line differs in two respects from similar layouts for spallation neutron sources: the beam current is lower, but the beam has to be chopped for each of the 144 accumulator ring bunches. As a consequence, the deflection voltage is limited to ±1 kV, which is about half of the voltage foreseen for spallation source facilities. On the other hand much longer chopper structures can be used, due to the relatively low 18 mA bunch current.

Two chopper structures of 60 cm length each and 20 mm or 30 mm gap height are placed in a 1.5 m long drift section. For about ±1 kV deflection voltage, the 20 mm and 30 mm chopper sections give 10 mrad and 7 mrad deflection, respectively. The width of the second chopper is increased by 10 mm to accommodate the deflected beam centre. The chopper section is symmetric around the ‘triple waist’ arrangement (waist in all three directions), in the middle of the 1.5 m long drift section. The total beam radius of 5 mm is increased to 7 mm after the first half of the drift section. The r.m.s. phase width of 10° is changed to 14° in the same drift. All three beam radii are near the acceptable limit in order to avoid filamentation caused by longitudinal and transverse nonlinear RF field components. Less than 1% of the particles are outside 10 times the r.m.s. emittance in each phase-space plane. As emittances, the values quoted in Table 4.1 are used.

Transverse and longitudinal focusing is applied by an RF cavity–triplet–RF cavity arrangement before and after the 1.5 m long chopper section. The beam collector is placed in a 0.5 m long drift section. A careful design is required because the energy is above the 2.16 MeV copper activation threshold. As a guideline for the collector system the SNS design with its TZM [molybdenum alloyed with titanium and zirconium] front plate could be used [36]. Complete 6-D phase-space matching from RFQ1 and into RFQ2 is achieved by placing doublets at the beginning and end of the chopper line. The

total length will be around 6 m, twice as long as the corresponding spallation source chopping lines. As there is only 18 mA bunch current, space-charge effects are of less importance even for a 6 m long chopper line. However, phase-space filamentation due to nonlinear RF field components cannot be avoided because of the long drift sections of the chopper line. Less than 30% r.m.s. emittance increase is expected in all three planes.

4.4 Drift Tube Linac

A Drift-Tube Linac (DTL) at 352 MHz frequency brings the beam from 7 MeV energy to 120 MeV. In the present design [37], a conventional Alvarez-type DTL is used up to 18 MeV energy. Above, a more efficient DTL structure with quadrupoles outside the tanks can be used.

The two Alvarez-type DTL tanks covering the range between 7 and 18 MeV are similar in design to the CERN Linac2, apart from the smaller diameter, corresponding to the higher resonant frequency. The tanks are stabilized by post-couplers and the focusing lattice is of the FODO type, with quadrupoles in each drift tube. The aperture diameter is 20 mm, corresponding to about 9–10 times the r.m.s. beam size, considered as a safe value for beam losses. The quadrupoles are conventional electromagnets, with water-cooled copper conductors and a soft iron core. The quadrupole power supplies are d.c., to avoid the high costs of long-pulse power supplies at a high repetition rate and to gain in flexibility for possible operation of the machine at different duty cycles. About 1 kW power has to be dissipated in each quadrupole, imposing an external diameter of the drift tubes of 200 mm. As a consequence of the choice of the aperture and of the drift tube diameter, the shunt impedances of the two Alvarez tanks are only 18 and 23 MΩ/m.

At higher energies, focusing becomes more effective and space-charge forces are lower. The focusing period can be made longer and the quadrupoles can be taken out of the tanks. DTL structures with quadrupoles between the tanks, often referred to as Separated-function DTL (SDTL), offer the double advantage of a higher shunt impedance (due to the smaller diameter of the drift tube that does not contain the quadrupole) and easy access and alignment of the quadrupoles. The tolerances on drift-tube alignment are considerably relaxed, with a reduction in the structure cost.

Several SDTL structures have been considered, but for the present design a Coupled-Cavity DTL (CCDTL) structure of the Los Alamos type [38] has been retained, though adapted to the relatively low frequency of 352 MHz. This structure is made of chains of small 2-gap DTL tanks connected by single-cell bridge couplers, with the quadrupoles placed between the tanks. The single DTL tanks operate in the 2π-mode, while the chain of tanks operates in the more stable $\pi/2$ mode, with no field in the bridge-coupler cavities. The additional advantages of this structure are that it does not need a matching section between the standard DTL and the CCDTL because it keeps the FODO focusing though with a longer period and that the RF distribution is made particularly simple. The distance between the tanks is short enough to allow them to be connected with simple 1-cell TM01-mode bridge couplers, identical all along the linac. Because of the relatively low number of tanks to be connected together, it can operate with a low coupling factor between tanks, with a minimum impact of the coupling slot on the shunt impedance.

A section of the CCDTL designed for this project is shown in Fig. 4.8. It is composed of nine chains of tanks, each one connected to one klystron. Because of the different tank lengths (about $1.5\ \beta\lambda$), the number per chain goes down from 18 for the first chain to eight for the last chain. The coupling between the tanks and the bridge coupler is 2%, a value that gives sufficient stability and a negligible power flow droop even in the longer chains, without too large a reduction in the shunt impedance due to the coupling slot (8% in the present design). The peak power per klystron is about 750 kW, and the average power being only 150 kW it is certainly possible to feed the chains of tanks via a single coupling iris placed in the central tank. RF windows for a power of 1 MW are available from industry and the coupling to the cavity can be made with a tangential waveguide terminated in a short-circuit at $\lambda/4$ from a coupling iris. With this configuration, the amplitudes and phases in each tank are precisely defined, there is no need for waveguide distributions, and the RF matching can be easily

achieved and if necessary modified for different currents by changing the position of the short-circuit. The gradient in this section is 2.5 MV/m, and the peak surface field is everywhere below 1.8 Kilpatrick. The aperture diameter is increased to 24 mm in order to accommodate the larger excursions of the beam due to the longer focusing period, and it still contains more than eight times the r.m.s. beam size. Figure 4.9 shows the computed effective shunt impedance, which includes the losses on the end walls, as a function of energy for the two DTL structures. The CCDTL allows an increase of about 50% in shunt impedance compared with the standard DTL.

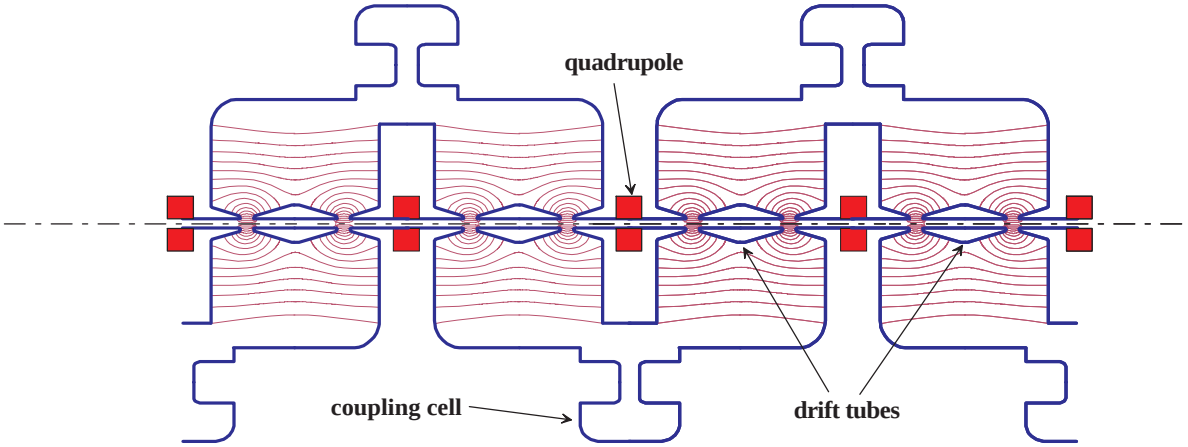

Fig. 4.8: Coupled-Cavity DTL structure at 352 MHz (indicated are electric field lines).

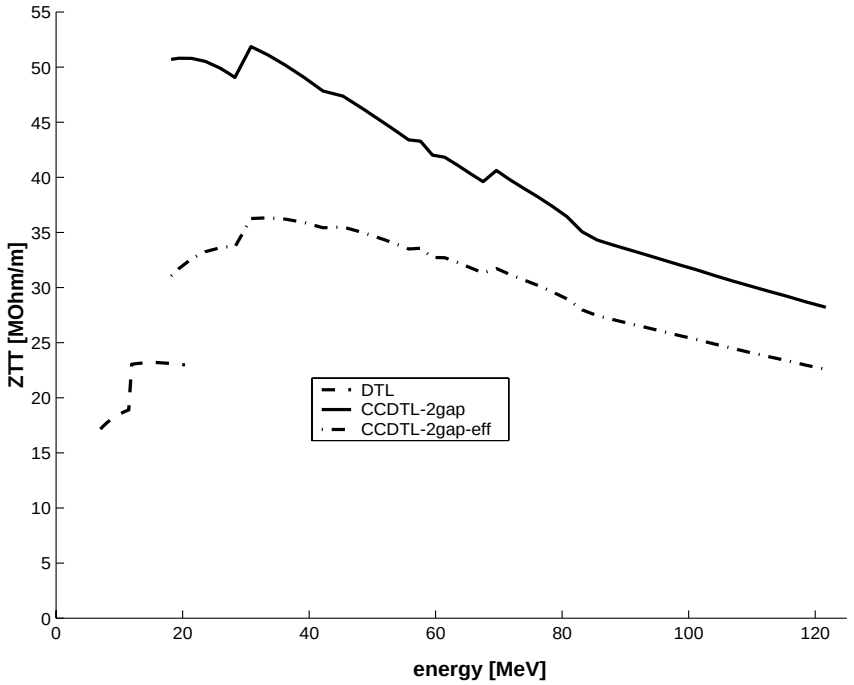

Fig. 4.9: Effective shunt impedance for DTL and CCDTL.

The main geometrical and beam dynamics parameters of the two DTL sections are given in Table 4.4. The overall length of the DTL is 78 m.

Table 4.4: Parameters of the Drift Tube Linac.

	DTL	CCDTL	
Input energy	7	18	MeV
Output energy	18	120	MeV
Number of tanks	2	98	
Number of klystrons	2	9	
Peak RF power	1.6	7.1	MW
Tank diameter	0.47 to 0.49	0.58 to 0.47	m
Tank length	4.3 to 3.3	0.23 to 0.78	m
Aperture diameter	20	24	mm
Drift-tube diameter	200	85	mm
Mean accelerating field	2–2.5	2.5	MV/m
Synchronous phase	–38 to –30	–35 to –25	(°)
Number of quadrupoles	58	98	
Overall length	8.4	69.6	m

The beam dynamics through the DTL has been computed with the code PARMILA [39] for a current of 40 mA, to leave a margin from the design bunch current of 18.4 mA, and a transverse emittance of 0.26 π mm mrad (r.m.s., normalized). In the first tank, the gradient is linearly increased and the synchronous phase decreased, to adapt progressively the beam to the higher gradient of the DTL and to increase the longitudinal acceptance at the entrance. The simulations (25’000 particles) show 100% transmission and no emittance growth. The transverse phase advance per period at zero current is 33°, and the tune depression is 0.85 at 40 mA current. Figure 4.10 shows the emittance evolution in the DTL, while Fig. 4.11 shows the r.m.s. beam size.

The increase in the period of oscillation in the CCDTL part can be seen, however there is no evidence of mismatch in the transition between the two sections.

The beam dynamics stability of the whole DTL structure was analysed using an input beam with 30% mismatch (beam radii) in all three planes. The emittance growth for the r.m.s. emittances as well as for the 90% emittances is between 30% and 35%. According to the PARMILA results, all particles are still kept well inside the aperture [37].

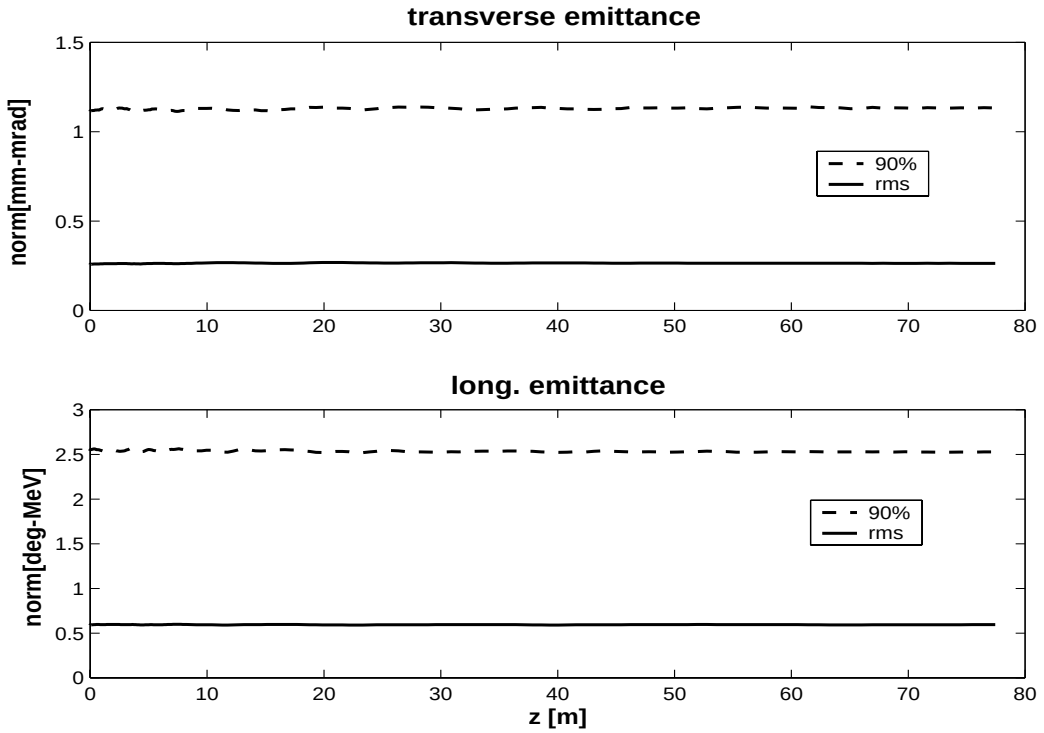

Fig. 4.10: Transverse and longitudinal emittance along the DTL.

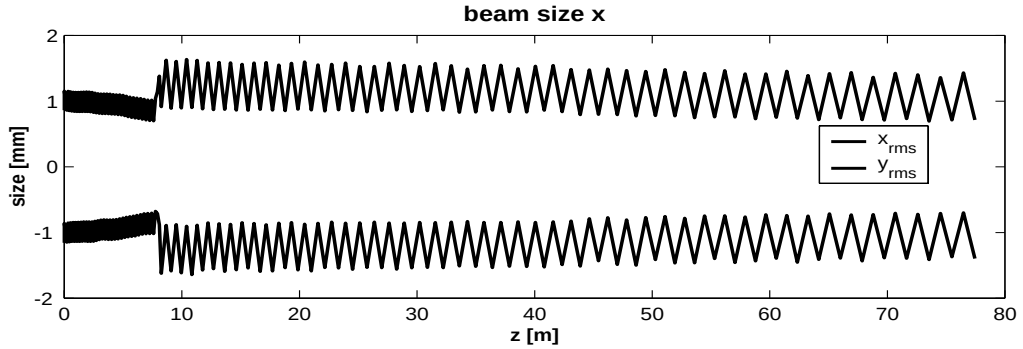

Fig. 4.11: r.m.s. beam size along the DTL (positive scale for x, negative scale for y).

4.5 Superconducting linac

4.5.1 Layout

The superconducting part of the linac covers the energy range between 120 MeV and 2.2 GeV. It is composed of four sections made of cavities designed for beta of 0.52, 0.7, 0.8 and 1. Standard 4-cell $\beta = 1$ LEP cavities are used at energies above 1 GeV. The cavities at $\beta = 0.52$ and 0.7 contain four cells, whilst the $\beta = 0.8$ cavities are made of five cells, to allow the existing LEP cryostats to be re-used. For the two lower beta sections, new cryostats have to be made, which will contain four cavities in the $\beta = 0.7$ section and three cavities in the $\beta = 0.52$, to shorten the focusing period at low energy. The shape of the basic cell profiles (central cell) for $\beta = 1$ (LEP), 0.8 and 0.7 are shown in Fig. 4.12. Figure 4.13 shows the layout of the four cryostats.

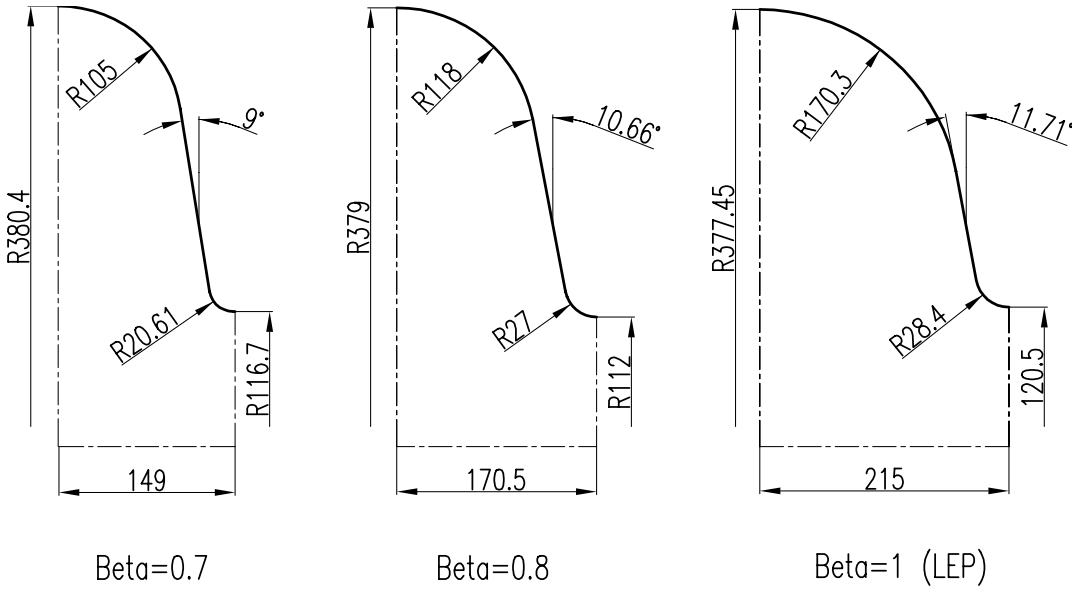

Fig. 4.12: Basic superconducting cell profiles.

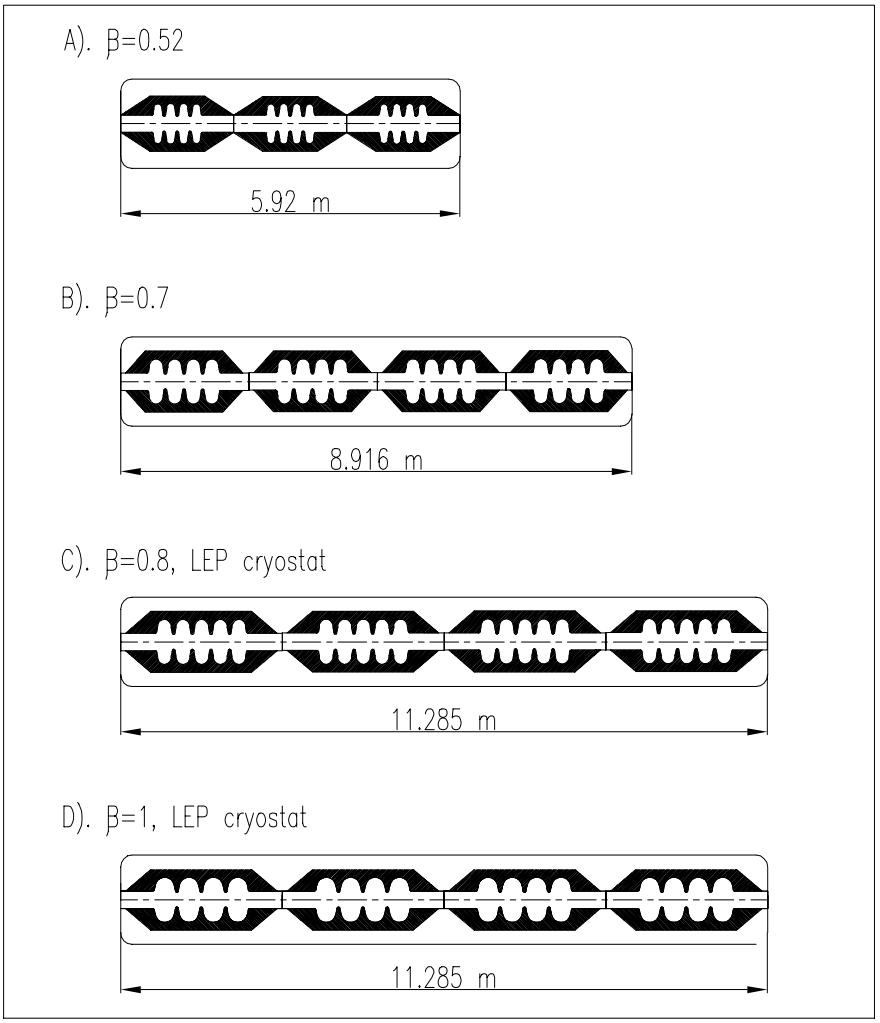

Fig. 4.13: Layout of the cryostats.

The cavities at $\beta = 0.8$ and $\beta = 0.7$ can be produced with the standard CERN technique of niobium sputtering on copper [40]. A beta of 0.7 is considered as the minimum that can be achieved with this technique [41]. The cavities at $\beta = 0.52$ could be made instead in bulk niobium or with a modified sputtering technique, with technologies still to be developed.

The layout of the superconducting linac is given in Table 4.5. Table 4.6 indicates the main design parameters for the four sections. It has been assumed that in the linac the LEP cavities will operate at 7.5 MV/m, the mean gradient achieved during the 1999 run [42]. For the $\beta = 0.8$ cavities that have to be specifically built for the linac, special cleaning procedures to achieve high gradients can be applied, and a design gradient of 9 MV/m can be foreseen. During tests, a $\beta = 0.8$ cavity has already reached gradients of 10 MV/m [43]. The Q_{ext} assumed for the different sections includes a 20% overcoupling with respect to the theoretical value to increase the bandwidth and to reduce cryogenic losses at the end of the pulse. The transition energies between sections are defined in order to have the maximum effective accelerating gradient (Fig. 4.14) and to minimize the phase slippage inside the cavities. Because of the higher field, the $\beta = 0.8$ cavities show a higher accelerating gradient than the $\beta = 1$ cavities over a wide range of energies; however, from about 1 GeV it is economically convenient to start using the LEP cavities. This transition energy could be more exactly optimized once all the cost parameters are known in detail.

Table 4.5: Layout of the superconducting sections.

Section	Beta	W_{in} (MeV)	W_{out} (MeV)	No. of cavities	No. of cells per cavity	No. of cryostats	No. of tetrodes	No. of klystrons	Length (m)
1	0.52	120	237	42	4	14	42	–	101
2	0.7	237	389	32	4	8	32	–	80
3	0.8	389	1080	48	5	12	–	12	153
4	1	1080	2221	108	4	27	–	18	357
Total				230		61	74	30	691

Table 4.6: Superconducting cavity parameters (at the design β).

Section	Beta	Gradient (MV/m)	Loaded Q_{ext}	R / Q (Ω)	Filling time (ms)	Synchronous phase (°)
1	0.52	3.5	2×10^6	61	0.90	–25
2	0.7	5	2.5×10^6	108	1.13	–20
3	0.8	9	3×10^6	192	1.36	–15
4	1	7.5	2×10^6	234	0.90	–15

Pulsing of the superconducting cavities is carried out by driving the klystrons at maximum power during the pulse rise time. With the available RF power, the rise time will, in all the cavities, be less than 2 ms. At the end of the beam pulse, the cavities are left free to empty at their natural field decay time.

Focusing is provided by quadrupole doublets placed between cryostats. The distance between cryostats is 1.42 m in all the sections, providing space for the doublets and for beam diagnostics.

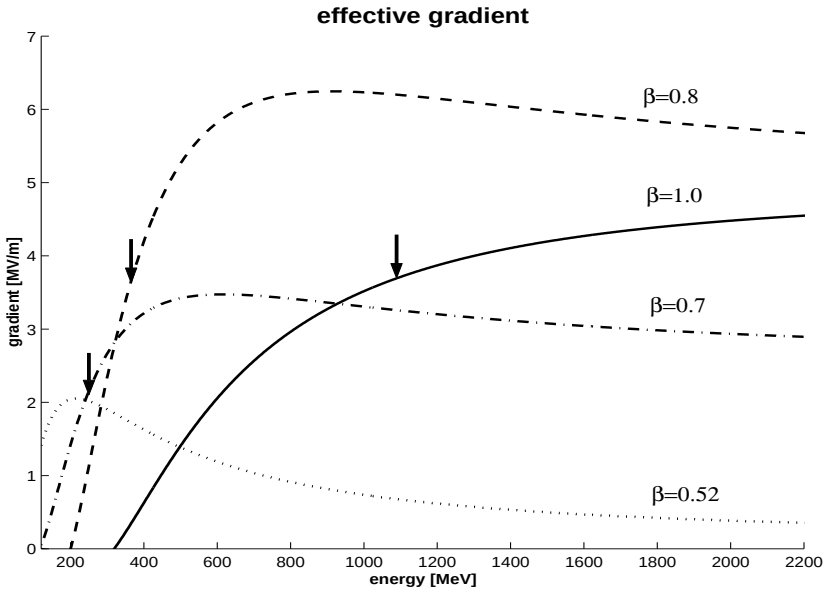

Fig. 4.14: 'Real Estate' accelerating gradients for the four sections. The starting point of each section is indicated by an arrow.

The cavities in the $\beta = 0.52$ and 0.7 sections are fed by individual 100 kW tetrode amplifiers, in order to minimize the amplitude and phase errors due to mechanical vibrations in the low beta range where the still large beta variation per cavity make the beam very sensitive to errors. From the $\beta = 0.8$ section the LEP 1 MW klystrons can be used. One klystron feeds four cavities in the $\beta = 0.8$ section and six cavities in the $\beta = 1$ section, via 2/3 – 1/3 power splitters. The RF power required from each klystron in these sections goes from 470 to 750 kW, leaving enough margin for the vector-sum compensation of cavity errors (Section 4.7). Correct phasing between cavities is achieved by changing the waveguide length.

This scheme re-uses 108 cavities out of the 288 installed in LEP. Considering that eight more LEP cavities are needed for the bunch rotation before injection into the accumulator, only 40% of the existing LEP cavities are needed in the present linac design. The required number of LEP cryostats is 41, i.e. 57% of the 72 existing ones.

4.5.2 Superconducting-cavity design and technology

The superconducting cavities at present installed in LEP have been built after the development at CERN of the technique for the sputtering of a film of niobium on the internal surface of a cavity made of copper (usually called Nb/Cu technique). This procedure, in spite of the complication intrinsic to the sputtering process, has many advantages for the large productions required by high-power linear accelerators with respect to bulk niobium cavities.

- The cost of the raw material is much less for copper than for niobium. This gives the possibility to go for low frequencies (352 MHz in our case) where the iris aperture is big (200 mm or more), relaxing the mechanical tolerances and reducing the danger of impact of the beam halo on the cavity walls.

- Nb/Cu cavities can be operated at 4.5 K with Q factors of more than 10^9. This simplifies the design of the cryostats and of the devices such as the power coupler, which have to work between 300 K on one side and the low temperature on the other side.

- The excellent mechanical properties of copper ensure a better thermal and mechanical stability, the latter particularly important in pulsed linear accelerators where cavity vibrations are a major concern.
- The performances of Nb/Cu cavities are not macroscopically influenced by the earth's magnetic field, allowing a simplified cryostat design without any magnetic shield.

The sputtering of the niobium film is carried out using the d.c. magnetron technique. A cathode covered with Nb sheets is introduced under clean conditions on the longitudinal axis of a cavity treated by chemical polishing. Under the combined action of magnetic and electric d.c. fields in a plasma atmosphere of argon, a film of Nb can be deposited on the inner surface of the cavity. The geometry of superconducting cavities allows a very simple set-up, where the cathode is just a cylinder.

A development programme was started at CERN in 1996 to investigate the feasibility of the production of reduced-beta (in the range 0.5–0.8) cavities without important modifications to the relatively simple sputtering set-up. The main results are the prototypes of a 5-cell $\beta = 0.8$ cavity and of a 4-cell $\beta = 0.7$ cavity for whose sputtering only the diameter of the cathode and the length of the magnets have been changed with respect to the LEP layout. Figure 4.15 shows the prototype $\beta = 0.7$ cavity.

Fig. 4.15: Prototype Nb/Cu $\beta = 0.7$ cavity.

Apart from the cavity itself, a complete LEP cryostat contains much 'ancillary' equipment that can be re-used without major modifications on any type of reduced-beta cavity. This includes the slow and fast tuners; the power couplers; the High Order Mode (HOM) couplers; the superinsulation, which prevents thermal losses by radiation from the insulation tank at 300 K to the cavity at 4.5 K; and the insulation vacuum tank. Only for the cavities $\beta = 0.7$ and possibly $\beta = 0.52$ will the insulation vacuum

tank and the tuners need to be redesigned because their length is too different from that of a LEP cavity. Moreover, the end drift tubes ('cut-off' tubes) connecting the cavities to each other can also be recovered for cavities $\beta = 0.7$ and $\beta = 0.8$ by cutting them from LEP cavities [44]. These tubes represent the most expensive part of a bare cavity.

The LEP cavities (Fig. 4.16) can be re-used without any modification in the linac for the section $\beta = 1$. Their design gradient of 6 MV/m has been reached and exceeded during operation. The maximum average gradient reached in 1999 is 7.5 MV/m, which can therefore safely be assumed as the target average value for operation in the linac, considering also that only 40% of the LEP cavities will be re-used in the linac, allowing some freedom to select the best performing cavities. All the ancillary equipment of these cavities has been designed for the LEP beam at 10 mA, which is very close to the nominal beam current of the linac, 11 mA. This means that at the moment no modifications have to be foreseen to the different components. In particular for the linac, an external Q of the power coupler of 2×10^6 has been assumed. This is so close to the nominal value for LEP (2.2×10^6) that no change in the length of the central conductor is necessary.

It is worth noting that the cavities are working in LEP with a slope of the floor of the tunnel around 1.4% (in Point 2 and Point 6 of LEP). This is more or less the theoretical limit for the cavities in their standard configuration, in order to be sure that no helium gas pockets can be formed, and has to be assumed as the maximum slope allowed for the linac tunnel.

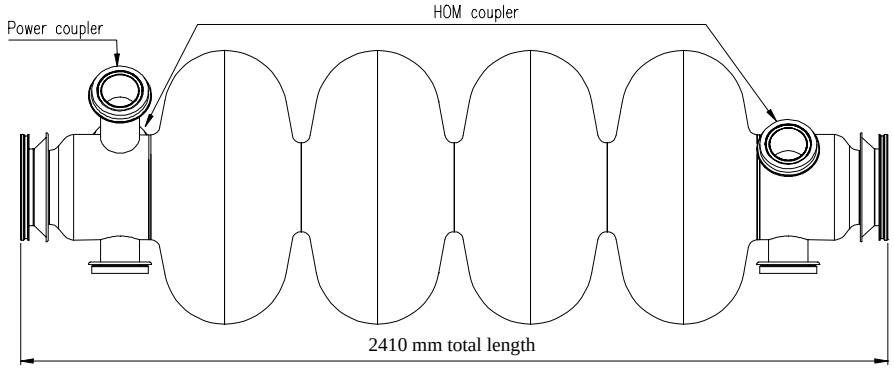

Fig. 4.16: The LEP cavity.

The cavities at $\beta = 0.8$ can also profit from the dismantling of LEP cavities. In fact a 5-cell $\beta = 0.8$ cavity will have exactly the same length as a 4-cell $\beta = 1$. It therefore fits into a LEP cryostat, re-using the cut-off tubes, the tuners, HOM couplers, insulation tank and main coupler (the external Q with the present specifications matches critically to the beam at a value of 3×10^6). A prototype of this cavity was built at CERN by modifying a LEP cavity and tested both at low power (with an input antenna critically matched to the unloaded Q of the cavity, say 2×10^9), and at high power with a LEP power coupler (Q_{ext} without modifications was 1.5×10^6) [43]. The results of low-power measurements are shown in Fig. 4.17. At high power we could condition the cavity up to the linac nominal gradient of 9 MV/m.

The cavity at $\beta = 0.7$ has been designed according to the results of the R&D programme on reduced-beta cavities at CERN [43, 44]. Its geometry was optimized to reach an unloaded Q value of 1×10^9 at 5 MV/m. The result of the measurements on several prototypes built at CERN led to the conclusion that the glazing angle of the atoms of niobium on the copper surface during the sputtering process cannot, on any point of the surface, be less than $\sim 28°$ in order to obtain a film quality comparable to that of the LEP cavities [41, 45]. In this cavity the minimum glazing angle is about 29°. A 4-cell cavity has been designed and built and the result of low-power measurements are shown in Fig. 4.17. This cavity is now being assembled in a LEP cryostat (with some modifications) in order to test it at high power.

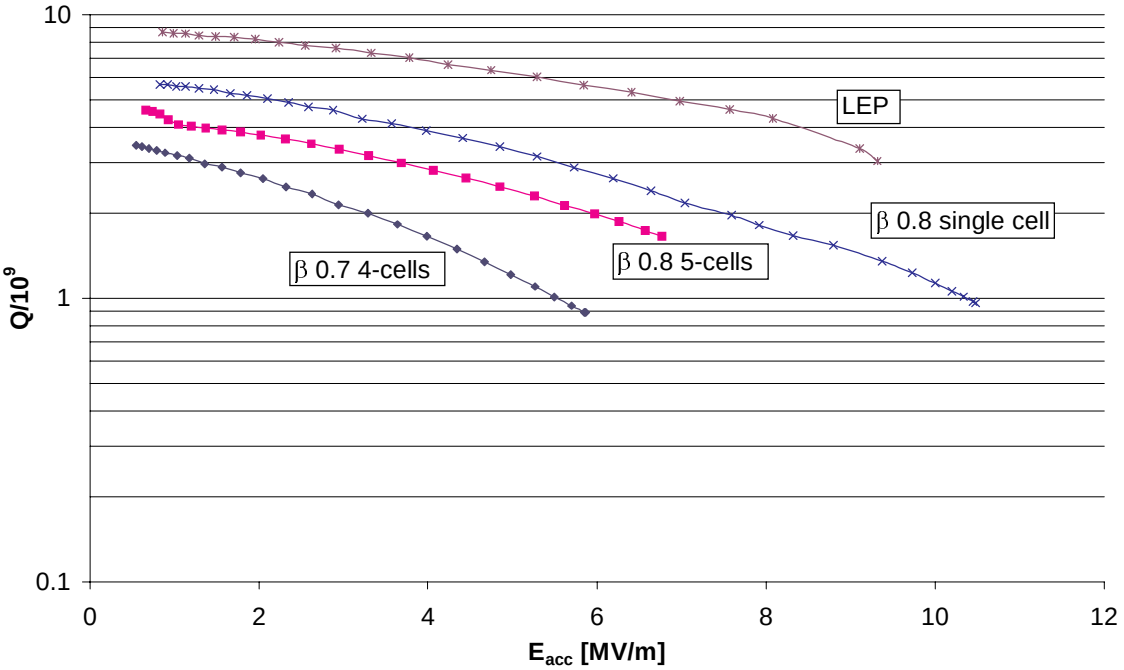

Fig. 4.17: Measured Q value vs. gradient of the prototype $\beta = 0.7$ and $\beta = 0.8$ cavities.

The section made of cavities at $\beta = 0.52$ still needs some R&D. A single-cell Nb/Cu cavity at $\beta = 0.48$ has been built with the standard technique at CERN with results that were quite disappointing [maximum field of 2 MV/m with an excessive slope of the $Q_0(E_{acc})$ curve]. Some efforts must be made to find new shapes for the cavity, or to modify the 'standard' sputtering technique. For all these reasons the nominal gradient for this section has been relaxed to 3.5 MV/m with an unloaded Q of 10^9, which seems to be within reach if a specific R&D programme can be launched. If necessary, a linac section at room temperature with the same Real Estate gradient (gradient averaged over the total linac length) of 1 MeV/m could be used to cover this section, which represents only 100 m of structure, in case the nominal performance could not be reached with superconducting cavities.

4.5.3 Beam dynamics

In the design of the superconducting linac optics [46] particular care was put into matching between the different sections, where the length of the focusing period and the accelerating gradient change abruptly, in order to avoid halo formation due to mismatch. For example, going from the beta section 0.7 to 0.8, the focusing period passes from 16 to 20 $\beta\lambda$ and the gradient from 5 to 9 MV/m. A satisfactory matching is achieved by changing slightly the quadrupole gradients and the cavity phases immediately before and after the transition point.

The magnet gradients vary between 3.9 T/m and 6.8 T/m. The gradients are adjusted so that the zero current transverse phase advance decreases from 79º for the first period to 30º for the last one. Among the different approaches for the variation of the phase advance that were tested, the present one allows for a smooth variation of the phase advance per unit length and shows the smallest emittance growth and the most stable behaviour against mismatch. The equipartitioning factor, defined as longitudinal over transverse beam temperature, is everywhere above unity, to avoid the excitation of parametric beam resonances giving rise to beam oscillations in the transverse plane.

The synchronous phase in the different sections is adjusted in order to have maximum acceleration without driving the beam too much into the non-linear region of the bucket. However, for the high-beta sections (0.8 and 1) a low phase angle (i.e. close to the crest of the wave) becomes a viable choice, because at high energy, phase oscillations are slow and non-linearities do not have time to develop filamentations. In the present design the synchronous phase angle is –15° in the section $\beta = 0.8$, and –17° in the section $\beta = 1$ (LEP cavities).

The preliminary particle tracking through the superconducting linac section was performed via simulations with the PARMILA code [39] starting from a 6-D waterbag distribution of 50'000 particles with a transverse normalized emittance of $0.4\,\pi$ mm mrad. The corresponding evolution of the r.m.s. beam radius, longitudinal coordinates along the linac, and normalized emittances are shown in Figs. 4.18–4.20.

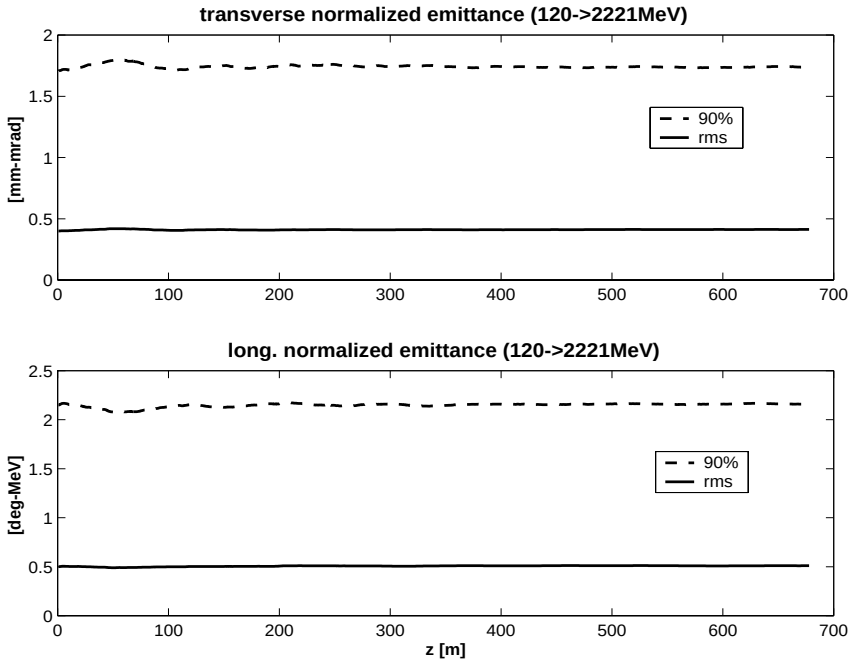

Fig. 4.18: Transverse and longitudinal r.m.s. and 90% normalized emittances along the superconducting linac (matched case).

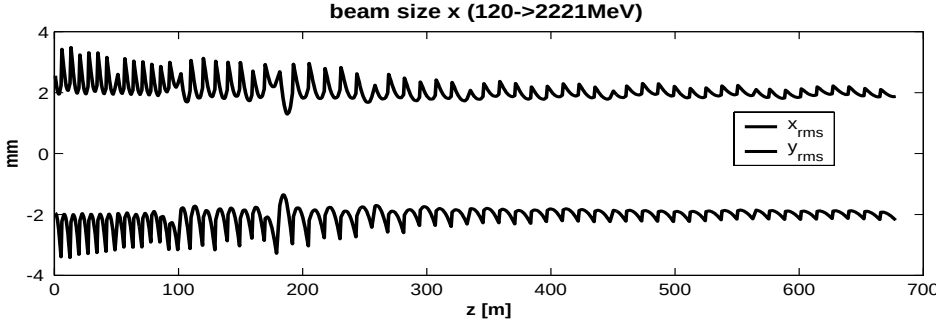

Fig. 4.19: Beam size in x and y along the superconducting linac (matched case, positive scale for x, negative scale for y).

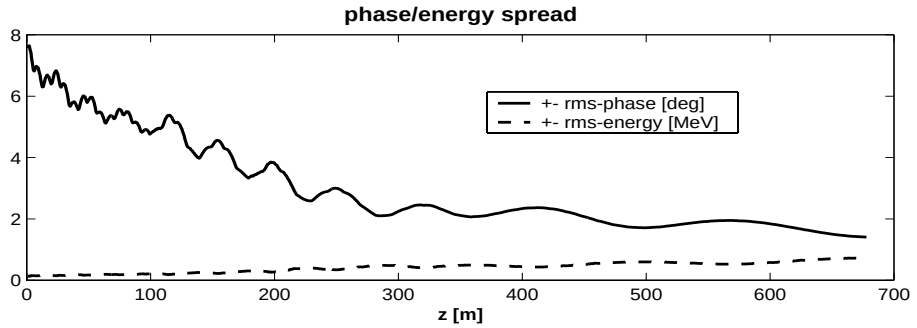

Fig. 4.20: Longitudinal beam parameters along the superconducting linac (matched case).

There is no emittance growth in the three planes, neither for the r.m.s. nor for the 90% and 99.9% emittances. As the r.m.s. beam radii are about 2 mm at the linac end, there is a safety margin there of a factor of 50 between the minimum aperture (100 mm radius in the quadrupoles) and the r.m.s. beam size.

The simulations were carried out with a current of 40 mA, i.e. more than twice the nominal linac current of 18 mA. At this current, the maximum transverse tune depression is 0.73, indicating that the linac operates well above the space-charge regime.

The stability of the optics design was tested with two different codes by introducing a strongly mismatched input beam (30% mismatch in beam size, 30% radial and ±30% axial). Using PARMILA the r.m.s. emittance growth remains below a few per cent in all three planes, and even the 99% and 99.9% emittances show no uncontrolled blow-up (Fig. 4.21).

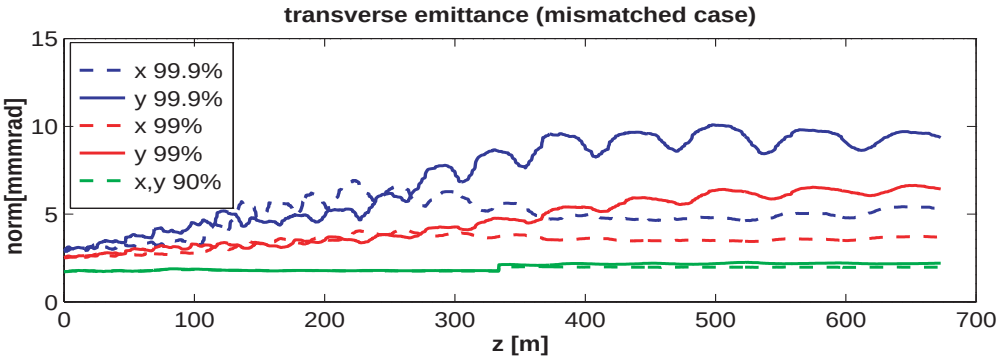

Fig. 4.21: PARMILA results for the transverse emittances (90%, 99%, 99.9%) along the superconducting linac for the 30% mismatch case.

The same set-up was simulated with the code IMPACT [47]. This 3-D parallel PIC code allows simulations with a large number of particles and includes a complete mapping of the fields in the RF cavities, which is important for the correct treatment of designs with large variations of the equivalent synchronous phase from one cavity to another.

The multiparticle simulations were carried out with 50×10^6 particles, i.e. only a factor of 7 below the actual number of particles contained in the bunch and a sufficient number to see relative losses in the range of 10^{-7}/m. A first run with the nominal setting confirmed the preliminary results obtained with PARMILA. Then, two different runs with 20% and 30% mismatched input beam showed r.m.s. emittance increases up to 100% transversally and up to 50% longitudinally, depending on the sign for the axial mismatch. However, in all the cases the beam transverse distribution remains gaussian and there is no evidence of the migration of particles into diffused halos. Looking at the longitudinal phase space one can observe only a small filamentation for the nominal case, but a noticeable one for the

mismatched case. For the 30% mismatch case, the maximum beam radius is below 20 mm everywhere, still a factor of 5 below the minimum aperture. Figure 4.22 shows the maximum and r.m.s. beam radius in x for the nominal and the mismatched case.

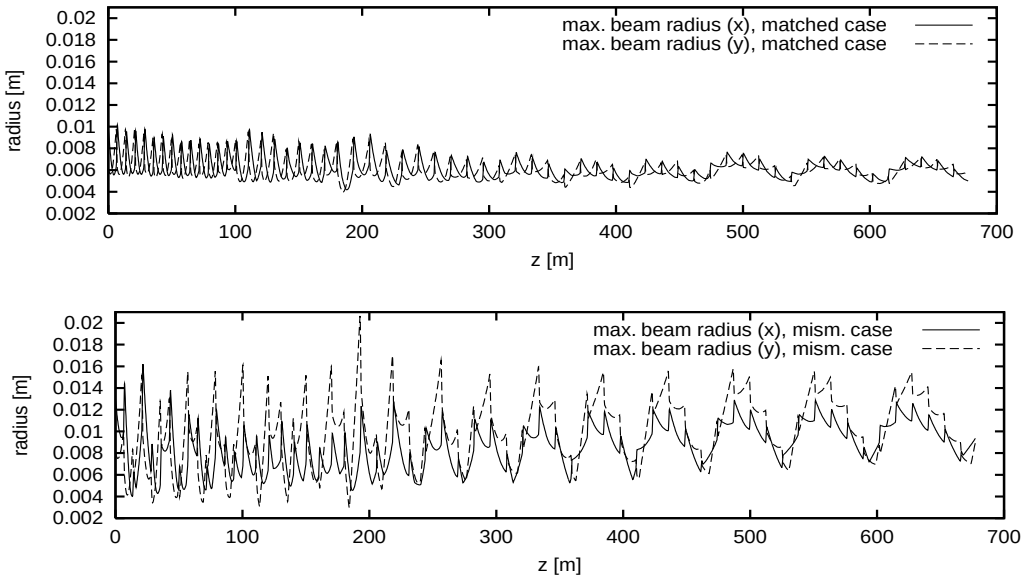

Fig. 4.22: IMPACT results for the overall beam radius (50 million particles) for matched (top) and 30% mismatched (bottom) cases.

4.6 Stretching and collimation line

The long transport line between the end of the linac and the accumulator, with connections to the PS and to ISOLDE, provides two additional functions: stretching the linac bunch length and collimation in the three planes before injection into the accumulator.

At the end of the superconducting linac section the bunches are about 40 ps long and have an energy spread of the order of 5 MeV. To reduce space-charge effects at the accumulator injection, the bunch length has to be increased in the transfer line by at least a factor of 10 and the energy spread reduced by the same factor. This is achieved by two bunch rotation systems made of LEP superconducting cavities. The first one (8 cavities, 2 cryomodules) is placed at the linac exit and increases the energy spread in such a way that in the following long drift the bunch length increases to the required value. The second bunch rotation section (2 cavities) reduces the energy spread again. The voltage on the bunch rotation cavities and their relative position depends on the longitudinal beam emittance at the linac exit. In the final layout, it can be readjusted for an effective longitudinal emittance that takes into account the effect of superconducting cavity vibrations (Chapter 4.5).

The main collimation section of the transfer line is placed in the first quarter of the ISR tunnel. Transverse and longitudinal collimation is provided by stripping foils, and the stripped ions are deflected in the bending magnets situated after the collimator towards beam dumps placed in shielded regions at the edges of the ISR tunnel. Six dumps are foreseen, two per phase plane, designed for a maximum beam power of 8 kW, corresponding to 0.2% of the beam. In total, they can intercept 1.2% of the beam before injection into the accumulator. Longitudinal collimation is designed to eliminate particles outside the accumulator acceptance, whilst transverse collimators will clean a large fraction of residual halo particles. The 15 m cross-section of the ISR tunnel is large enough to accommodate three parallel chambers (accumulator, compressor and transfer line) plus some additional shielding. The dumps can be placed in shielded bunkers on the outside of the circumference. In addition, some pre-collimation on smaller dumps can be made in the bend between the end of the linac and the ISR tunnel, to partially clean the beam before it is injected into the PS at a much lower beam power.

The quarter turn of the ISR and the transfer line add up to a length of ~ 456 m, which consequently defines the maximum length of the stretching and collimation line. The first bunch rotation section, 25.6 m long, will be placed inside the linac tunnel. The second bunch rotator of length 12.8 m will be placed after 281.4 m, and the remaining 136 m will be used for the collimation section. The general layout of this line [48] is described in Table 4.7, and Table 4.8 reports the longitudinal beam parameters along the line computed with a distribution of 100,000 particles at the entrance of the superconducting linac section. Phase and energy spread are presented in Fig. 4.23 and the corresponding phase space distributions are shown in Fig. 4.24.

Table 4.7: General layout of the stretching and collimation line.

Element	Length [m]	No. of LEP cavities	No. of focusing periods	Cavity parameters
Bunch rotation 1	25.6	8	2	8.6 MV/m at ϕ = +90°
Drift	281.4		22	
Bunch rotation 2	12.8	2	1	4.4 MV/m at ϕ = –90°
Collimation	135.8		11	
Total	455.6			

Table 4.8: Total bunch length and energy spread.

	2 × r.m.s. length	100% length	2 × r.m.s. energy	100% energy width
	[ns]	[ns]	[MeV]	[MeV]
Linac out	0.011	0.029	1.5	5.0
Transfer line out	0.15	0.44	0.11	0.5

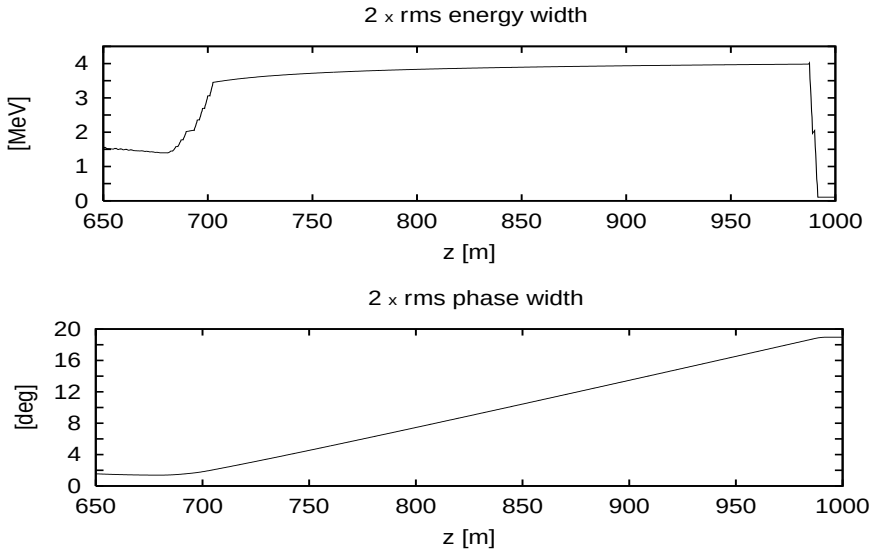

Fig. 4.23: Energy and phase width in the last part of the linac and along the transfer line (end of linac at z = 680 m).

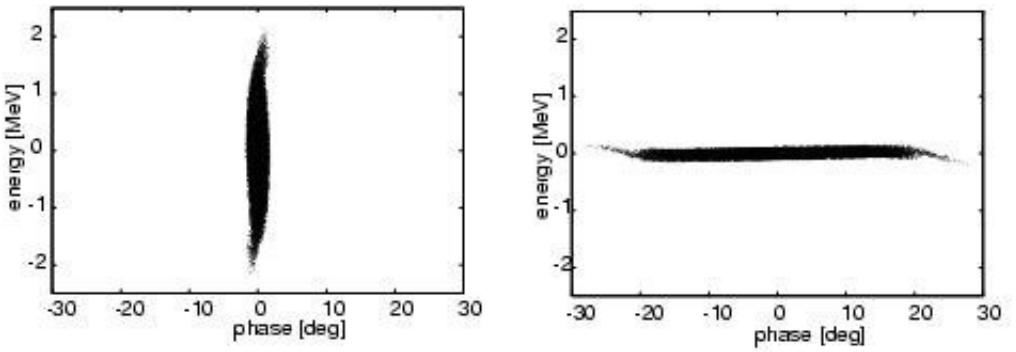

Fig. 4.24: Longitudinal phase space before and after the transfer line.

The overall layout of the transport line is shown in Fig. 4.25. The transfer to the PS and to ISOLDE is made via existing tunnels, where a collimation section with smaller dumps can be placed. The bending radius of the transfer tunnels is large enough to avoid Lorentz stripping (see next chapter). A full power (4 MW) dump is foreseen after the collimation section and before the injection into the accumulator, to be placed inside or close to one of the old SPS experimental halls. The same dump could also be used for setting up the accumulator and compressor rings.

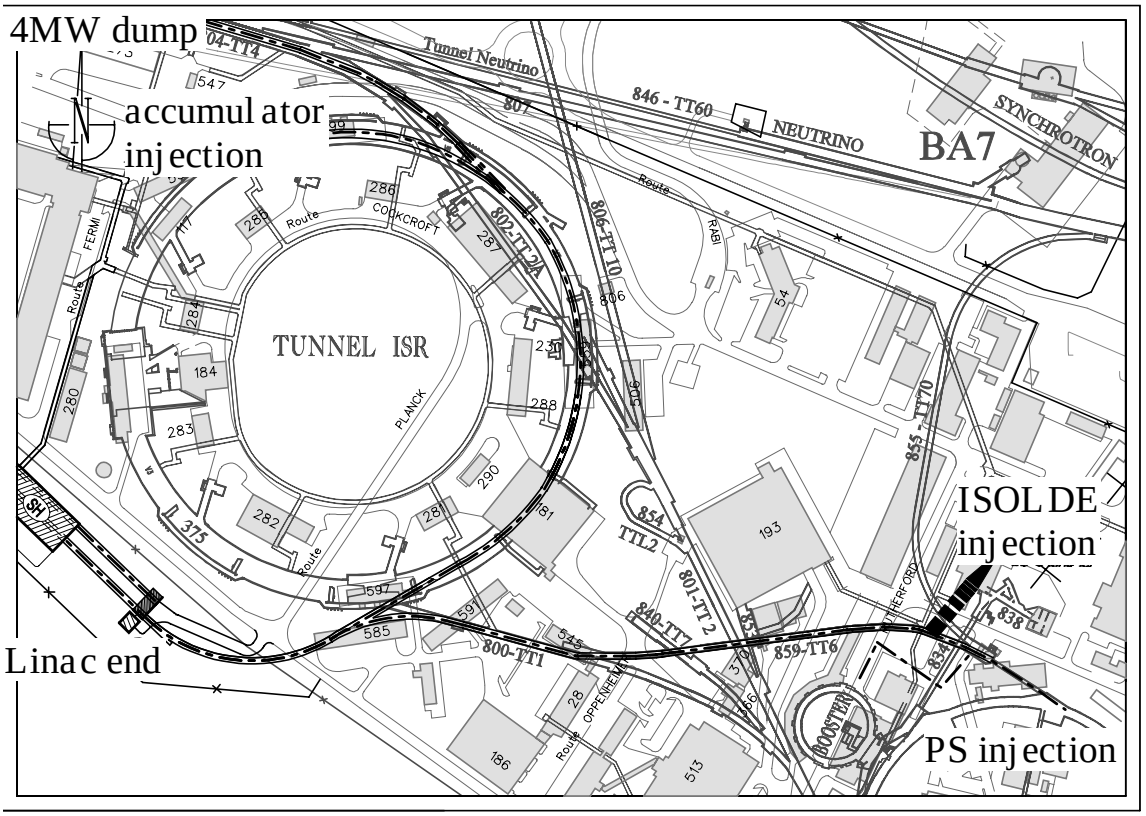

Fig. 4.25: Layout of the transfer lines.

4.7 Pulsed operation and energy stability

In the superconducting part of the linac, the resonance frequency of the cavities can fluctuate as a result of external excitations such as cryogenic pressure oscillations, bubbles in the cooling liquid, vibrations from the vacuum pumps or ground movements. The Lorentz force also lowers systematically the resonance when the field in the cavities rises. Since the loaded bandwidth of superconducting cavities is generally small, even minor mechanical perturbations can produce a resonance shift of a considerable fraction of a bandwidth. Furthermore, the sudden onset of the beam loading creates a fast transient of the cavity field. All these effects, if not correctly compensated, can create beam oscillations that would finally result in beam loss.

To reduce the effect of the perturbations on the cavity field, a fast vector RF feedback loop has to be built around the cavity and its transmitter. Since the gain is limited by loop delays, there will always remain a residual perturbation on the field. Moreover, in the last two sections of the superconducting linac a single RF transmitter feeds several cavities. The system therefore stabilizes the nominal vector sum, but the individual cavities react within their filling time on sudden changes. The latter are of the order of milliseconds, comparable to the field rise time and pulse duration, so that there is always a non-negligible ongoing drift of the individual cavity fields.

To study the influence of all these perturbations and system errors on the beam, a computer program was written which simulates the acceleration of bunches in a full phase space representation along the whole linac [49]. It simulates all fast RF vector sum feedback loops with non-linearities, such as loop delays, transmitter power limits and limited amplifier bandwidth.

The program was initially used to simulate configurations with different numbers of cavities per klystron. It appeared immediately that the low-energy sections were extremely sensitive to errors and that every attempt to feed more cavities from a single RF transmitter led to beam loss. The configuration where every cavity in the $\beta = 0.52$ and $\beta = 0.7$ sections is fed by its individual transmitter is much more stable and has been retained for a more detailed study. The following analysis was made taking a beam with the nominal longitudinal emittance (±35 ps, ±140 keV) entering the superconducting section at 120 MeV, and crossing a linac with 1, 1, 4 and 6 cavities per transmitter in the four linac sections. Only the final results are shown here and more details, as well as the analysis of the different configurations, can be found in Ref. [50].

The gain of the feedback loop is set to 100, a compromise between the stability requirements and the presence of power peaks. Errors in the power-splitting network and Q_{ext} of the power couplers are included, but their effect is minimal since they are counteracted by the vector sum. A random complex error in the vector sum of 5% maximum value has been included in the simulations.

Lorentz force detuning was not examined in detail because it is a repetitive effect and feedforward techniques can be applied which largely reduce its effect. The TESLA project [51] is putting a large effort into this subject and has already indicated ways to solve the problem [52, 53]. A first estimate — using a coarse measurement for the LEP2 cavities — shows that our cavities without stiffening but with lower field levels, will react with about the same excursion (measured in bandwidths) as the stiffened TESLA 9-cell cavities. Therefore the RF control solutions for TESLA could be directly applicable under the same conditions, provided enough RF power is available. However, an additional difficulty for the SPL is its much higher repetition rate, where oscillations at the mechanical modes are not damped between pulses and resonant enhancement is possible. Therefore, further experiments on test cavities are necessary, especially with respect to Lorentz force detuning and mechanical behaviour.

To illustrate how the vector sum operates, Figs. 4.26 and 4.27 shows the calculated evolution of voltages and powers during a linac pulse for a test case of the first $\beta = 0.8$ module (four cavities connected to the same transmitter). In the calculation it is assumed that the four cavities vibrate with different frequencies and amplitudes (Fig. 4.26 top). At the beginning of the pulse, the transmitter rises to full power, 1 MW, while the cavities begin to be loaded with their filling time, the real part of all four voltages rising in a very similar way. The imaginary parts differ more because of the different

individual detuning status (vibration) (Fig. 4.26 middle). When the measured vector sum (Fig. 4.26 bottom) reaches the set value, the transmitter power reduces to an equilibrium value, identical to the reflected power.

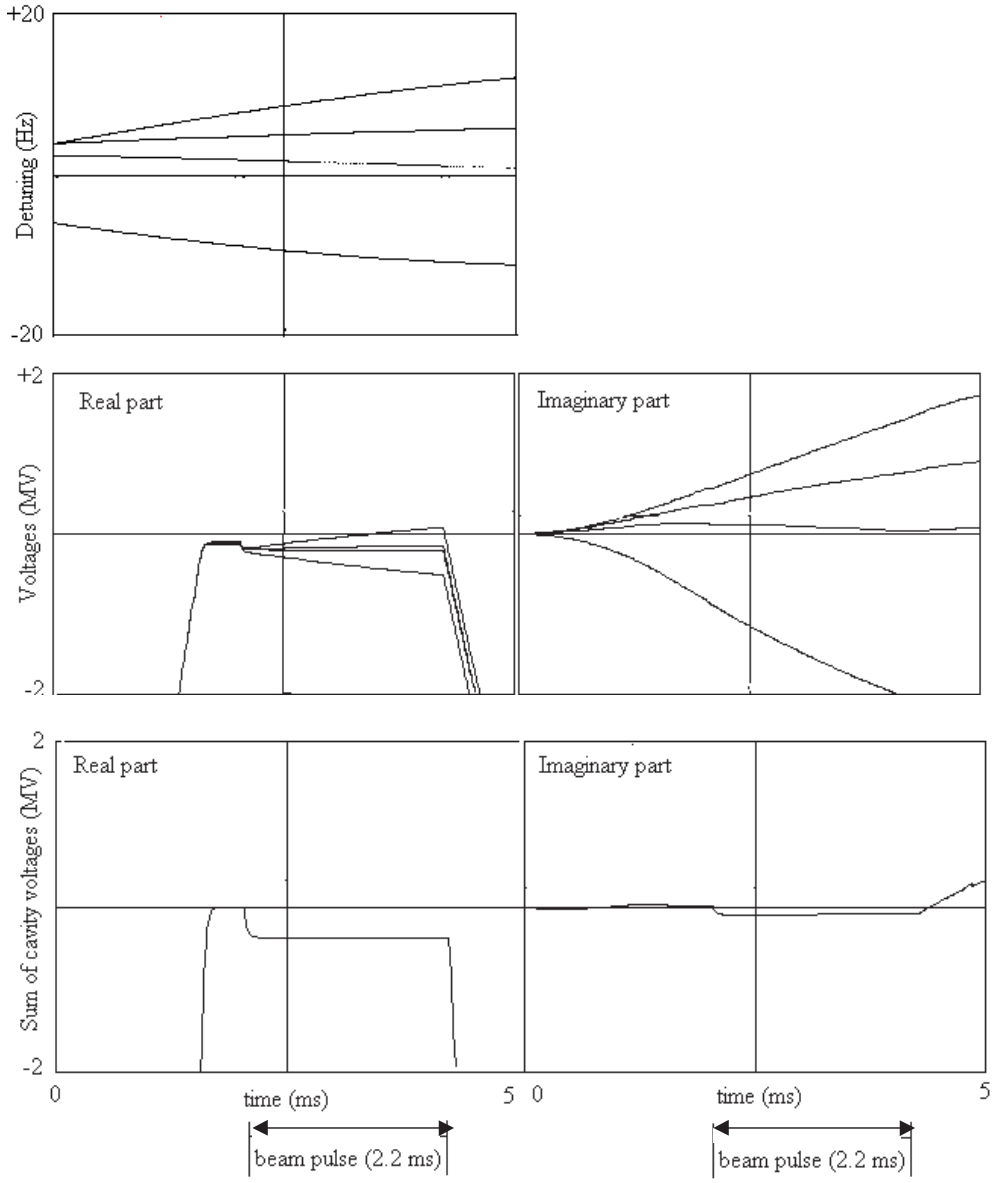

Fig. 4.26: Typical pulse shapes in a vector sum compensation case (first $\beta = 0.8$ module, four cavities per transmitter, incoherent random vibrations of individual cavities with amplitude up to 20 Hz). From top: individual cavity frequencies, individual cavity voltages (real and imaginary parts, deviation from nominal value), sum signal of all four cavity voltages with errors as seen by the feedback system (real part and imaginary part, deviation from nominal value).

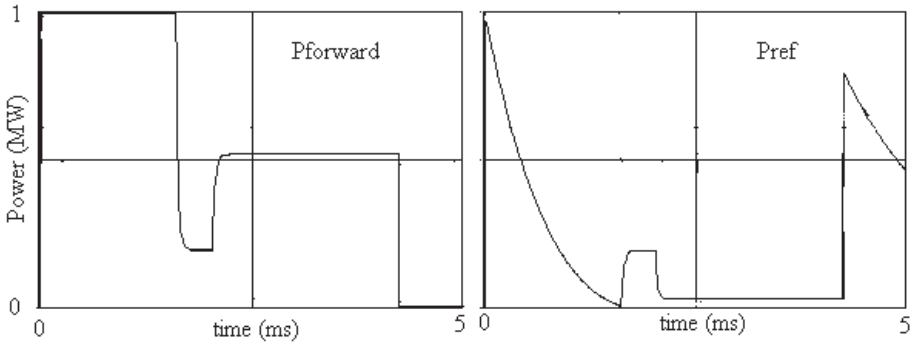

Fig. 4.27: Forward and reflected klystron power corresponding to the case of Fig. 4.26.

After 2 ms the beam pulse starts, and changes the cavity voltage. Since the beam loading is different for the four cavities because the transit time factor varies with the particle velocity, the individual cavity voltages drift apart with their filling time, but the vector sum is kept constant by the feedback system. The transmitter power quickly rises to a new equilibrium to supply the beam power, and the reflected power drops to about zero (for a matched coupler). At the end of the pulse (t = 4.2 ms) the RF is switched off and the cavities unload naturally.

Even in the presence of a perfect vector sum compensation, the individual cavities in a module will have different phases due to dynamic detuning and consequently the energy gained by the bunch will differ from one cavity to another. In the case of low-beta protons, the drift times and thus the synchronous phase angles become different, leading to large bunch oscillations in the longitudinal phase space. For large perturbations, a bunch can even go over the crest of the RF wave in one cavity, introducing strong non-linearities that cannot be recovered again on any other cavity and producing large filamentations, increasing considerably the energy spread of the beam. The situation is made worse by the errors in the realization of the vector sum. The limit of the tolerable increase in energy spread caused by the vibrations is given by the acceptance of the accumulator and by the design of the collimation section in the transfer line. The ±2 MeV total acceptance of the accumulator transforms into ±10 MeV at the linac exit. Should these limitations become slightly tighter, the permissible vibration amplitudes and/or system errors will have to be reduced correspondingly. Particles outside these limits can be cleaned out in the collimation line and collected on the beam dumps. However, for a maximum beam power on the dump of 50 kW, one has to allow only 10^{-2} of the particles outside these limits.

Externally-driven vibrations:

The case of externally driven vibrations has been studied considering that the resonant frequency of each cavity can oscillate, driven by vibrations at a certain mechanical frequency. The amplitude of the mechanical vibrations determines the amplitude of the resonant frequency oscillations. Several vibration amplitudes, expressed in Hz of deviation from the normal resonant frequency were considered but only the 40 Hz cases are shown here. They represent the limiting conditions. For the mechanical vibration frequency two distinct cases, coherent and incoherent, were considered. A coherent case uses only one common vibration frequency, as is the case for that of a common origin (e.g. driven by the cryogenics system). The value chosen for the simulations was 47.8 Hz, as uncorrelated as possible to the 75 Hz repetition rate. The arrival of the centre of the bunch in phase space is plotted in Fig. 4.28a for four statistically independent ‘chosen’ machines, and the display range is ±0.1 ns (equivalent to ±13° at 352 MHz) and ±20 MeV. Each beam pulse is represented by 10 reference bunches distributed equally along the 2.2 ms pulse length. The distribution of the beam particles in the longitudinal plane is calculated for 100 consecutive pulses. The equivalent incoherent case uses statistically independent frequencies scattered ±20 Hz around 47.8 Hz, and the arrival of the centre of the bunch in phase space is plotted in Fig. 4.28b.

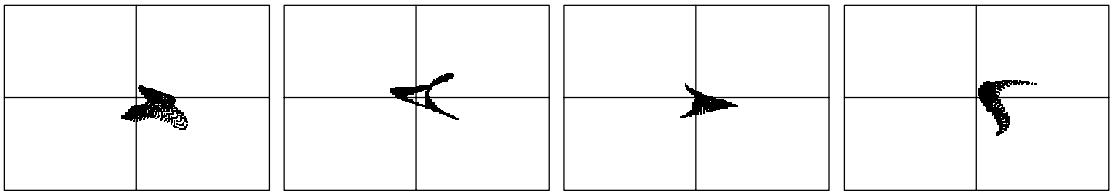

Fig. 4.28a: Location in phase space (±0.1 ns, ±20 MeV) of the centre particle at the exit of the linac. Amplitude 40 Hz, coherent oscillation at 47.8 Hz for four different random parameter distributions.

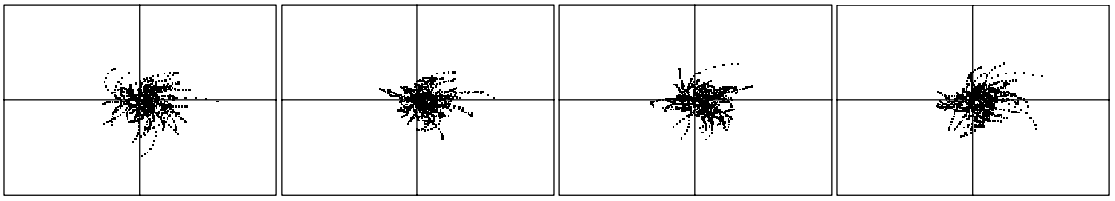

Fig. 4.28b: Location in phase space (±0.1 ns, ±20 MeV) of the centre particle at the exit of the linac. Amplitude 40 Hz, incoherent oscillations around 47.8 Hz ±20 Hz for four different random parameter distributions.

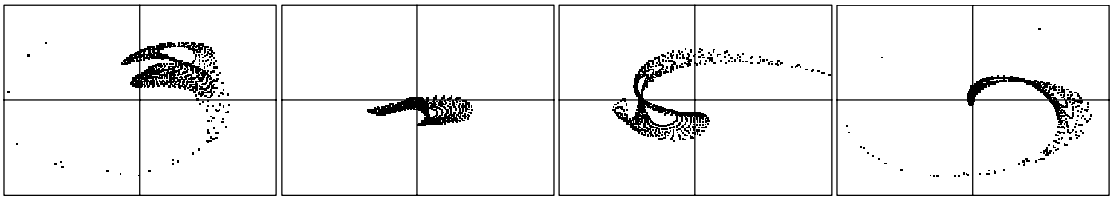

Fig. 4.28c: As 4.28a but with 5% vector sum and power splitting error, 10% Q_{ext} scatter.

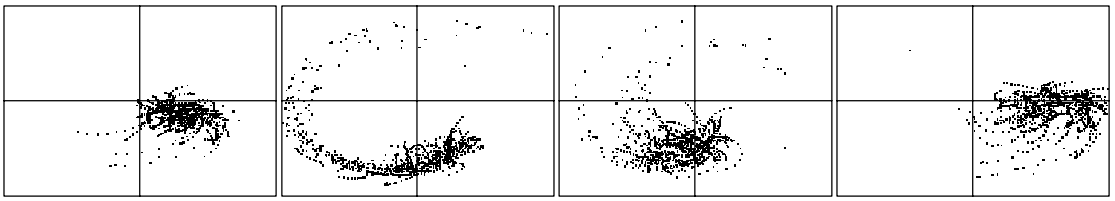

Fig. 4.28d: As 4.28b but with 5% vector sum and power splitting error, 10% Q_{ext} scatter.

Figure 4.29 shows some typical phase-space images of bunches at the end of the linac, with coherent frequency errors for vibration amplitudes of 40 Hz. The conclusion of this analysis is that in the present linac design with a perfect vector sum, vibration amplitudes of up to 40 Hz can be accepted, the desired 99% of the beam still arriving within a span of ±10 MeV at the end of the linac.

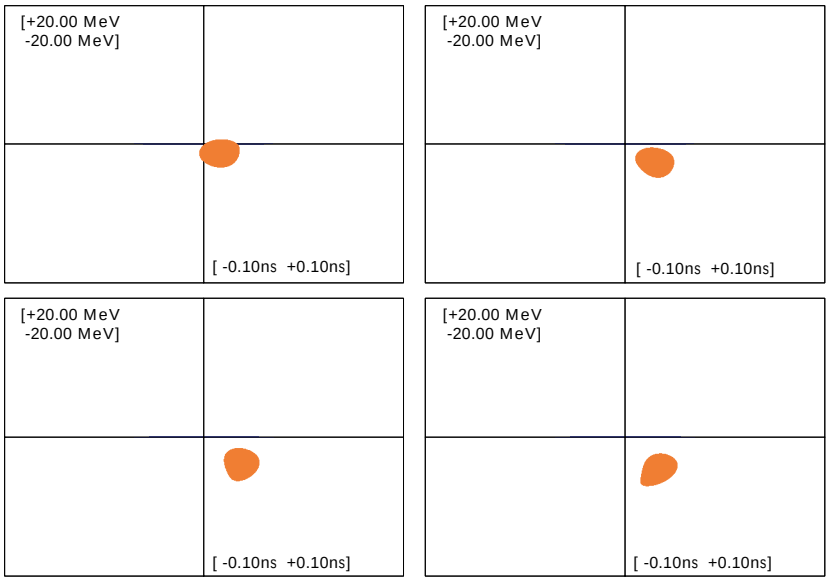

Fig. 4.29: Longitudinal phase-space images at the end of the linac corresponding to the case on the left of Fig. 4.28a, 40 Hz coherent amplitude with perfect vector sum. The four bunches shown are equally distributed along the pulse.

Vector Sum Errors:

Optimum compensation of the perturbations is reduced by the vector sum errors in the feedback loops (Figs. 4.28c and 4.28d). With errors of up to 5% the beam starts to go beyond the energy limits for a vibration amplitude of 40 Hz. In comparison, 5% errors in the power splitters and 10% in Q_{ext} are negligible. Figure 4.30 (lower four frames) includes a badly filamented set of bunches for about 25% of the 'bad' pulses. However, even with 5% vector sum errors but reduced vibration amplitudes (e.g. 20 Hz), the energy spread remains within its limits.

Beam loading:

The sudden onset of beam loading induces a coherent voltage change which is not completely compensated because of the finite gain of the feedback (see Fig. 4.26). This lets the first bunch at the end of the linac arrive at the nominal position in phase space whilst the following bunches sweep through the phase space to settle rapidly on the new equilibrium position. The 'sweep time' is as expected, of the order of the filling time divided by the loop gain, i.e. a few tens of μs. The simulations for an ideal system with sudden onset of beam loading and a feedback loop of gain 100 show that the energy deviation is largely below ±10 MeV. However, tests with 5% error for the vector sum feedback showed beam sweeps larger than ±10 MeV for a few (about 10%) statistical sets.

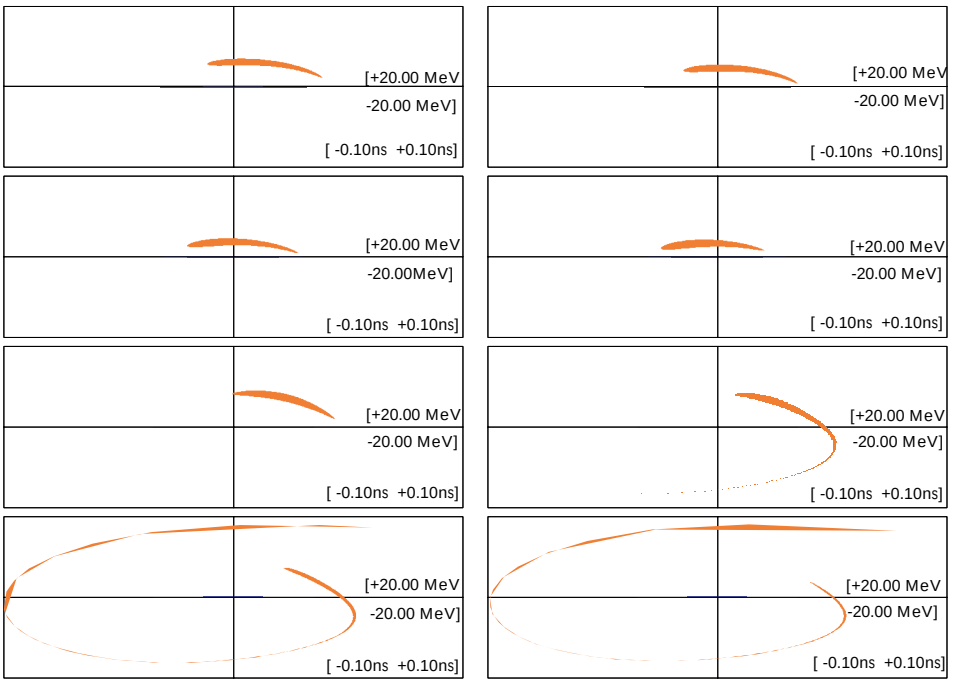

Fig. 4.30: Longitudinal phase-space images at the end of the linac corresponding to the left case of Fig. 4.28c. The upper four plots correspond to bunches equally distributed along the pulse for a good case, and the lower plots correspond to a bad case with strong filamentations.

4.8 Beam dynamics and loss management

An essential requirement of this linac design is to keep beam losses below the 1 W/m level. An accurate analysis of the different beam loss mechanisms was made, which led to some precautions in the design in order to eliminate known sources of losses. Simulations with large numbers of particles were performed to test the validity of some design choices. However, the approximations used in the codes, as well as their ability to model all the possible sources of errors in a real machine, only allow some preliminary positive conclusions to be drawn. Only more detailed simulations following the evolution of the beam from the source to the entrance of the accumulator ring, with a sufficient number of particles and including a detailed description of all the machine elements in the presence of random error distributions, will give a sound idea of the expected loss level. Such simulations are at the limit of the present computational power, and for the time being one should consider more limited simulations and refer to the progress recently made in the understanding of halo formation mechanisms in linacs.

Two main mechanisms can result in beam loss in an H^- linac: stripping losses and halo scraping losses. The stripping losses can again come from two different mechanisms, gas stripping caused by the residual gas and magnetic (Lorentz) stripping in the presence of magnetic fields.

The stripping caused by the residual gas was calculated for a gas composed of 95% hydrogen and 5% oxygen, following the treatment given in Ref. [54], based on a theoretical model [55] already confirmed by experimental data. The gas stripping loss is negligible (< 0.03 W/m) for 10^{-8} mbar pressure, while it approaches 0.25 W/m at 2.2 GeV energy for 10^{-7} mbar pressure. In the SC cavities the pressure is usually in the 10^{-9} to 10^{-10} mbar range, whilst in the short focusing sections between cryostats, it can be easily maintained in the 10^{-8} range, keeping gas stripping losses well below the limit level.

Magnetic stripping can occur in the bending magnets of the transfer lines or in the quadrupoles. A theoretical formula by Scherk [56] complemented by experimentally measured constants [57] allows the lifetime of the H^- ions in the rest frame of the particles to be calculated. This formula, applied to the bending of the 4 MW beam at 2.2 GeV, gives the beam loss per metre as a function of the bending field (see Fig. 4.31). A conservative factor of 10 should be assumed in the loss level, to account for the uncertainties in the theoretical treatment. Therefore, a maximum allowed field level of 0.16 T can be assumed, corresponding to 0.1 W/m calculated losses. Considering a magnet filling factor of 60% in the transfer line, this field corresponds to a 100 m minimum curvature radius permitted in the transfer lines.

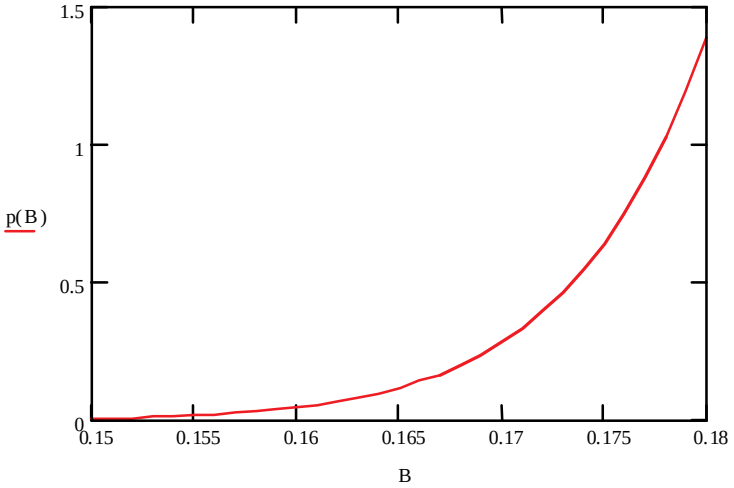

Fig. 4.31: Loss level (W/m) as a function of the magnetic field (T) for the SPL beam at 2.2 GeV.

The maximum quadrupole gradient at 2.2 GeV is 6.4 T/m (Section 4.5), i.e. the maximum field seen by a strongly mismatched beam at a distance of 16 mm from the axis (maximum excursion of Fig. 4.22) is only 0.1 T, well below the limit field for stripping.

The losses caused by the impact of beam halo with the vacuum chamber are a vast subject that has already been treated in the different beam dynamics sections of this chapter. Here it can be recalled that standard precautions (careful matching, smooth variation of focusing parameters, controlled equipartitioning factor, avoidance of resonances) have been applied in the design of the linac optics. A sensitivity study of the linac has shown that the present design remains stable against a strongly mismatched beam at injection. Moreover, the design of the superconducting linac was tested with 50 million particles, and even for the 30% mismatched case, no particles were outside ±20 mm at the linac end, and less than 0.1% of the particles were outside ±1 MeV after bunch rotation. Although a Monte Carlo analysis of distributions of 'realistic' errors would give a more detailed insight into the real increase in beam radius that can be expected, the 'mismatch test' can be considered a satisfactory proof of the insensitivity of this design to resonances and other factors that could send particles into a diffused halo. It must also be stressed that in comparison with other designs, the SPL has a relatively low bunch current of 18.4 mA (there are therefore no problems connected to space charge), and that in all the linac elements a large aperture has been preferred, to leave a greater safety margin against an unforeseen increase of beam radius.

However, some other studies with a lower number of particles in the simulations have been devoted to possible longitudinal beam losses, particles leaving the bucket as a result of phase and amplitude errors in the RF cavities, in particular because of vibrations of the superconducting cavities. The analysis in Section 4.7 shows that in the presence of large vibration errors in the cavities (±40 Hz maximum detuning), only a small fraction of the beam falls outside the acceptance of the accumulator. The collimators in the transfer line (Section 4.6) are designed to intercept up to 1.2% of the beam, and

this, together with the large acceptance of the accumulator transformed back to the linac exit (about ±10 MeV), gives a certain freedom against errors in cavity phase and amplitude. A different subject that has not yet been treated in detail is the longitudinal loss during initial turn-on transients in the RF cavities. However, the different options available for feedback and feedforward compensations will give some space for a precise adjustment of the fields when the beam starts to cross the cavities.

4.9 Radio Frequency

The Radio Frequency system makes use of two different types of transmitters, a low-power tetrode unit and a high-power klystron unit.

The low-power tetrode amplifier could be of the type used for leptons in the CERN SPS. This is a commercial Thomson amplifier cavity equipped with a TH571B tube. It can deliver up to 50 kW CW, limited by heating of the amplifier body, and thus in pulsed mode at the SPL duty cycle, up to 100 kW can be expected. This is large enough for the low-beta superconducting cavities, which require input powers between 23 kW and 65 kW, leaving enough margin for fast filling of the cavities and for the feedback loop.

For most of the linac cavities, i.e. the room-temperature and the high-power superconducting cavities at $\beta = 0.8$ and $\beta = 1$, it is intended to re-use the LEP RF equipment, i.e. the klystrons, the waveguide distribution system, and the klystron high-voltage, high-power converters.

The power converters for the klystrons have to deliver about 18 MW continuously to the RF systems (plug power about 24 MW). This estimation is based on the power transferred to the beam, the power needed to fill the cavities, and an estimated klystron efficiency of 50%. The LEP klystron power converters (4 MW, 100 kV d.c., 40 A) are primary thyristor controlled and in their present state not suited to the pulsed operation foreseen in the SPL [58, 59]. The control circuitry will be too slow to stabilize the collector voltage of the klystrons during the RF burst lasting only about 4 ms, with a repetition rate of 75 Hz. A way out would be the addition of energy storage capacitors to each klystron, sufficiently large to reduce the collector voltage drop to an acceptable amount. The power converter will then work as a practically constant current source. With respect to the present LEP situation, the secondary filter resonance (now 50 Hz) will considerably decrease. The consequences on the controls will have to be studied. The klystron current modulator will have to be upgraded as well for faster pulse response with steep slopes. A feedback or feed forward using the modulator anode could be envisaged in order to stabilize klystron operation during the RF burst, with the advantage of reducing the size of the energy storage capacitors. Test runs with a fast-pulsed klystron are expected to start soon [60]. Taking a reasonable safety margin, it is proposed to use only 3 MW out of the 4 MW available in each power converter. Six units with in total 46 klystrons connected will therefore be needed to satisfy the SPL RF power demands.

Appropriate circulators and loads will have to be foreseen in front of the superconducting cavities, in order to absorb the large amount of reflected power during the rise time of the pulse, and new 2/3–1/3 splitters will have to be used for the $\beta = 1$ superconducting section (18 klystrons), where one klystron feeds six cavities.

The nominal power required from the klystrons is between 500 kW and 750 kW. These levels are considerably lower than the peak klystron power of 1 MW (1.3 MW for some klystrons), which is however used for filling of the superconducting cavities. There is enough margin for the feedback loops, and a high system reliability is expected.

4.10 Cryogenics and vacuum

4.10.1 Cryogenic system

Since the LEP cryogenic system will be entirely converted for the LHC, new cryogenics has to be built for the superconducting linac, detailed in Ref. [61]. Table 4.9 presents the review of heat loads for the proposed linac design. Values are based on LEP measured data, whenever possible, or on the stated assumptions. Considering that the LEP RF equipment will be re-used, most of the values are given per module of four superconducting cavities.

Table 4.9: Review of heat loads.

	Heat load values (per module)	Assumptions
Static losses	107 W @ 4.5 K	• 80 W for the module itself (measured during acceptance tests) • 27 W for the helium lines contribution (measured during acceptance tests)
Liquefaction	0.80 g/s of LHe	Couplers and tuners measured consumption
Dynamic losses $\beta = 0.52$ $\beta = 0.7$ $\beta = 0.8$ $\beta = 1.0$	 82 W @ 4.5 K 196 W @ 4.5 K 732 W @ 4.5 K 210 W @ 4.5 K	• Corresponding to gradients and Q values of Table 4.6 • Considering 30% duty cycle (beam duty cycle plus pulse rise and fall time)
Thermal shields	6300 W @ 75 K (total)	Conservative value based on 10 W/m for 630 m of helium transfer lines

For the time being, the remaining uncertainties on different parameters concerning the superconducting cavities (duty cycle, quality factor values) require very conservative assumptions for the dynamic heat load estimations. The dynamic losses for $\beta = 0.8$ cavities are critical (significantly larger than the maximum of 650 W for LEP2 cavities), thus a special effort to reduce them and modifications of the LEP2 cryostats for increasing liquid helium supply flow rates would be mandatory. For the other heat load contributions, a minimum margin of 5% has been added. The global heat loads and the total cooling power required are presented in Table 4.10. No contribution for beam-induced losses has been taken into account.

Table 4.10: Total cooling power required.

	Installed capacity (including 5% margin)	Comments (Equivalence @ 4.5 K)
Static losses	6.9 kW	1 W ↔ 1 W
Liquefaction	48.8 g/s	1 g/s ↔ 125 W
Dynamic losses	18.4 kW	1 W ↔ 1 W
Thermal shields (50 to 75 K)	6.3 kW	1 kW ↔ 70 W
Total equivalent at 4.5 K	32.0 kW	

The proposed cryogenic system is illustrated in Fig. 4.32. The total equivalent refrigeration capacity of 32 kW at 4.5 K could be achieved using two refrigerators based on proven functional blocks similar to existing units in operation at CERN composed of the following:

– Storage tanks: the helium will be stored as gas, allowing the recompression and storage of evaporated helium in case of power supply failures.

– A compression unit based on oil-injected screw compressors with their oil removal system, compressing helium up to 20 bar and delivering a total flow of about 1250 g/s. Considering the LEP2 cryoplant experience, a helium drier would be foreseen before the cold box.

– A cold box with plate-fin heat exchangers and turbo-expanders, with a Joule–Thomson flow of about 820 g/s.

– A distribution valve box for interconnecting the two refrigerators via local helium transfer lines, and delivering the liquid helium to the superconducting cavities via the cryogenic transfer line.

The refrigerator will be connected to the cryostats via a helium transfer line covering the 630 m of superconducting linac length. It will include the liquid helium delivery, the cold gaseous return and a thermal shield loop housed in the same vacuum jacket of about 500 mm diameter.

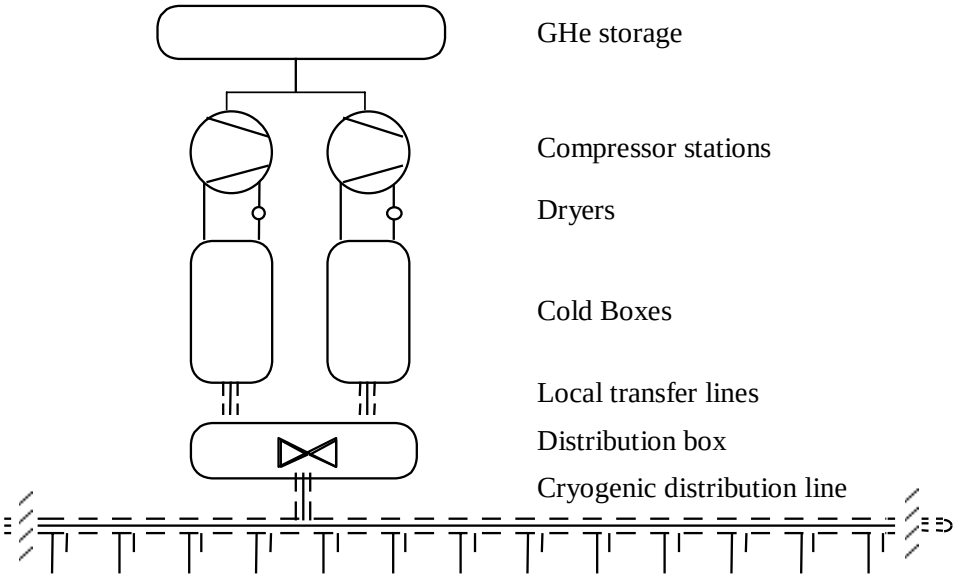

Fig. 4.32: Cryogenic system basic scheme.

4.10.2 Cryogenic infrastructure

The total helium inventory will be of about 42,000 Nm^3. Considering 250 m^3 horizontal storage tanks at 20 bar as for the LHC, a total of 10 tanks will be needed. Two layers of five units are proposed, with similar structures to the ones used for LHC.

For the hall housing the compressors, a standard CERN concrete wall construction of about 1650 m^2 is foreseen (building SH). It would contain the screw compressors with their oil removal systems (oil separator, coalescers and charcoal adsorber), as well as the electrical substations, the compressed air for instrumentation and some free space for unloading, spare parts storage and work place.

For the cold boxes and the distribution box, a standard CERN metallic wall construction of about 1000 m^2 is foreseen (building SDH). It would mainly contain the two cold boxes, the distribution box and some additional space for unloading and controls.

A 1×1 m duct should connect the storage tanks to the compressor building and a 2×2 m gallery should connect the compressor building to the cold boxes building.

With a power factor of 250 W/W, the equivalent 32 kW at 4.5 K cryogenic power would result in a nominal electrical power consumption of 8.0 MW. With the motors' power rating of 1.2, the installed power to be considered would be about 9.6 MW. At least one compressor ($\approx$ 1 MW) per cryoplant should be supplied as back-up system to allow the recompression of evaporated helium in case of utility failure. For the design of the cooling-water capacity required, a value equal to the nominal power

consumption is considered, i.e. 8.0 MW. This covers the needs for the compressors and the cold boxes. The ventilation required for the compressor building would be about 4% of the nominal power consumption, i.e. 320 kW. A typical 250 Nm^3/h compressed air unit would suit the instrumentation needs.

4.10.3 Alternative solutions to reduce costs

The interest of reducing the dynamic heat loads is evident when trying to economize cryogenic power. The latter results in 46% of the total cooling power required.

One option would be to operate the cavities at lower temperature, thus increasing the quality factor of the cavities and consequently reducing the heat loads to be evacuated. In addition, as the cost of cryogenic power would increase when decreasing the operating temperature, a theoretical optimum could be defined. As lower temperature means lower pressure, and as the cryogenic hardware of the LEP2 modules was not designed for sub-atmospheric pressures, technological reasons could prevent the theoretical optimum being reached. Nevertheless, it has been measured that a reduction of 0.3 K of the operating temperature would result in a reduction of 16% of the dynamic cryogenic power. One could envisage operating the cavities at 4.2 K (1.0 bar), which corresponds to ambient pressure, and compensate the corresponding 0.3 bar at the refrigerator entrance by cold pumps similar to the one foreseen for LHC, or by more warm compressors.

Another option would be to reduce static losses and liquefaction rate. The new cryostats for the $\beta = 0.52$ and $\beta = 0.7$ cavities have to be designed. Minimizing their volume would reduce static losses, and using mechanical tuners would eliminate the liquefaction rate for these cavities. For the $\beta = 0.8$ cavities the LEP cryostats will be adapted. One should also consider using mechanical tuners in order to reduce the liquefaction rate. It has to be noted that suppressing liquefaction would consequently simplify piping and instrumentation for the cryostats.

4.10.4 Vacuum

The vacuum system of the linac facility, which has an overall length close to 1100 m, can be divided into three parts with different vacuum requirements and space constraints: the warm section including the source (110 m), the cold section composed of all the superconducting cavities (720 m), and the last warm section corresponding to the transfer line (270 m). Owing to the short time the protons spend in the accelerator, the pressure requirements given by lifetime considerations are not stringent. On the other hand, the presence in the linac of superconducting cavities necessitates producing a clean and dust-free vacuum having all the characteristics of the ultra-high vacuum.

Although the use of recovered LEP equipment allows substantial cost savings, the cost of reconditioning the equipment must also be taken into account. Moreover, the decision concerning the recovery of this equipment must be taken soon enough to avoid both the extra cost of storing it and the destruction of equipment, such as vacuum chambers, which could be used in some parts of the SPL machine.

The first section of the SPL machine, which contains the source of protons plus the pre-accelerating RF cavities, will have complex vacuum vessels and probably little space available for pumps. In order to avoid ‘pollution’ of the superconducting cavities, part of this section will probably be baked to decrease the outgassing and will be mounted under clean conditions to avoid dust contamination of the vacuum vessels.

The vacuum system of the superconducting cavities section must ensure the clean and dust-free pumping of the delicate superconducting cavities. It could be a copy of the actual LEP straight sections where the cavities operate. The vacuum system is designed to minimize detrimental gas condensation inside the helium-cooled cavities. The procedures to operate it are defined, to avoid the propagation of dust particles during the roughing or the venting of these cavities. They also use ultra-high vacuum standards in order to avoid any contamination of the cavities’ surface.

The warm vacuum system is a bakeable stainless-steel system with a 100 mm aperture (DN100) using mainly items recovered from LEP. Powerful pumping stations (400 l/s ion pump and titanium sublimation pumps) allow the molecules outgassed in the adjacent warm parts of the vacuum system to be trapped and their condensation inside the cold modules to be avoided. Inverted magnetron gauges are used in the vicinity of the cold parts to avoid excessive heat loads to the cold system. All-metal roughing valves allow the roughing stations to be connected to the vacuum system. Each module is isolated by all-metal gate valves to avoid any contact with the dusty environment of the accelerator tunnel during their installation and transport.

The warm vacuum system of the transfer line will be rather simple but the pressure should be low enough to avoid the contamination of the cold cavities upstream. It is recommended to extend the use of UHV standards and to bake out the linac extremity of this transfer line.

5. LAYOUT ON THE CERN SITE

5.1 Radiation protection and shielding

In this initial stage of the shielding design, a simple model was employed to estimate the lateral shielding required for the linac and the high-energy transfer line, as well as to assess the radiation streaming through the waveguide ducts which will link the accelerator tunnel to the klystron tunnel. Two situations were considered, namely normal operation and accidental beam loss. Beam losses for normal operation were assumed to be 1 W/m, a generally accepted figure which should keep the induced radioactivity in the machine to a level sufficiently low to permit hands-on maintenance (see, for example, Ref. [62]). An accident scenario considers a full loss of the 4 MW beam either at a single point or distributed over a length of several metres (probably a more realistic scenario).

In the present design, the accelerator will be installed underground on Swiss territory. If the surface above the linac is not included in the CERN site, it will be a non-designated area according to the CERN Radiation Safety Manual [63], so that the dose must be kept below the limit of public exposure. Outside the fenced areas of the Organization, the dose at any point must not exceed 1.5 mSv per year and the dose actually received by a person must not exceed 0.3 mSv per year. The latter figure includes both external exposure due to stray radiation and the internal exposure due to radioactive releases from CERN. The service tunnel housing the klystrons (klystron gallery) is also underground, but as its access is restricted to CERN personnel, it will be classified as a controlled radiation area. If the piece of land under which the linac will be installed is acquired by CERN it will be classified as a supervised area and the dose-rate limit taken as 1 μSv/h (2.5 μSv/h being the maximum allowable under normal operation and 7.5 μSv/h the value under transient conditions).

For the shielding design, the dose-rate limit was taken as 0.1 μSv/h for public areas and 10 μSv/h for controlled areas. With an operating time assumed to be 180 days per year, i.e. 1.6×10^7 s per year, these figures ensure that the annual dose limit for the public and for CERN staff under individual dosimetric control (15 mSv) will not be exceeded. In practice, owing to the limited occupancy time of the klystron gallery, the dose to CERN personnel will stay well below the annual limit. In addition to the above requirements, a full beam loss at a localized point must not give rise to a dose equivalent rate outside the shielding exceeding 100 mSv/h, and the accelerator control system must be capable of aborting the beam in a time short enough that the integral dose caused by such an accidental condition remains negligible.

For the normal operation, the shielding calculations were performed at a few selected energies, namely 25, 100, 400, 1000 and 2000 MeV. The most stringent shielding requirements are imposed at the high-energy end of the accelerator because of the more penetrating component of the secondary neutrons. Below 1 GeV the simple point-source/line-of-site model was adopted. This model requires the knowledge of the source term (i.e. the number and energy distribution of the neutrons generated by the interaction of the proton beam with accelerator components or a target) and of the attenuation length (which accounts for the shielding properties of the material). At energies above a few GeV the Moyer model can be employed, for which there also exists a formulation for a line source [64]. The line-source model was applied above 1 GeV and the results compared with those of the calculations made for a point source. Such a comparison has shown that the two calculations give similar results if one assumes a beam loss over a distance of about 7 m concentrated at a single point. Thus the shielding assessments can be made by assuming a 1 W/m loss over 7 m concentrated in one point.

Source terms and attenuation lengths from Ref. [65] were used for energies from 25 MeV to 1 GeV, taking data for a thin copper target. The use of thin-target data is a reasonable assumption since a continuous loss during normal operation will most likely be produced by the beam halo grazing the vacuum chamber or interacting with aperture limitations at inter-cell gaps or at quadrupoles. This choice also represents a conservative assumption, as the neutron spectrum from a thick target would be softer, i.e. less penetrating through the shield. At 2 GeV, use was made of source term and attenuation length of the Moyer model. The minimum shielding thicknesses required to reduce the dose equivalent

rate to below the public limit and to below the design value of a controlled radiation area are given in Table 5.1. The required shielding thickness for a supervised area will be somewhere between the two values given in Table 5.1. The thickness for earth was assessed by simply scaling the shielding thickness for concrete by the ratio of the densities of the two materials (taken as 1.8 g/cm^3 for earth and 2.35 g/cm^3 for concrete).

Table 5.1: Minimum shielding thickness required to reduce the dose rate below 0.1 μSv/h (limit for public exposure) and 10 μSv/h (controlled radiation area) for a continuous loss of 1 W/m.

Energy (MeV)	Intensity (protons per second per 7 W loss)	Required shielding (cm of concrete)		Required shielding (cm of earth)	
		Public	Controlled	Public	Controlled
25	1.7×10^{12}	205	150	270	195
100	4.5×10^{11}	305	210	395	275
400	1.1×10^{11}	520	335	680	440
1000	4.5×10^{10}	595	375	780	490
2000	2.2×10^{10}	606	380	795	500

A beam-loss monitoring system, interlocked with the accelerator control, will be needed to ensure that during operation losses stay below the specified value of 1 W/m.

A shielding designed for a continuous beam loss of 1 W/m during routine operation is also adequate for an accidental loss of the full beam at a localized point, provided that the linac can be stopped within 100 ms, which is well within the capabilities of the accelerator control system. The integral dose delivered to the public area in this time interval is of the order of 1 μSv, essentially independent of whether the loss is localized at one point or distributed over several metres.

In the present design, several ducts of 0.5 m^2 cross-section will connect the linac and klystron tunnels and house the waveguides linking the klystrons to the RF cavities. At the low-energy end of the linac, the duct consists of two legs, the first 3.5 m long and the second 11 m long. At the high-energy end the duct is four-legged, with the first leg 3.2 m long, the second and the third 3 m long and the fourth 8 m long. Using the transmission curves of Ref. [65] and assuming a line source to calculate the attenuation provided by the first leg, the overall attenuations provided by the two extreme configurations are approximately 6×10^{-7} and 1×10^{-10}, respectively. Estimates of the line-source term corresponding to 1 W/m yield a (possibly conservative) value of about 10 Sv/h. To reduce this figure to the required 10 μSv/h demands that the duct provide an attenuation of 10^{-6}. Whilst this requirement is largely met by the four-legged configuration, the design of the two-legged one seems barely sufficient and will have to be more carefully studied at a further stage in the project.

If beam losses in the transfer line from the linac to the accumulator ring can be controlled to the value of 1 W/m, the shielding requirements are the same as those of the high-energy end of the linac. However, there will be exceptions represented by the collimators, where beam losses will be higher. The present design foresees six collimators which will in total intercept about 1% of the beam intensity. The collimators are actually stripping foils designed to remove particles from the beam halo and direct them into small dumps. If the beam transfer line is not at a sufficient depth, some local shielding will have to be provided around these dumps. For example, if the fraction of the beam dumped at one location is 0.3% of the full intensity, the shielding requirement is 10 m of earth plus a local shielding made of 80 cm of iron, to meet the dose-rate limit for the public. For the section of the transfer line running under CERN territory, which is a supervised area, the dose-rate limit can be taken as 1 μSv/h

and the local shielding can be reduced to 40 cm of iron. A detailed study will be needed once the design and the positioning of the transfer line have been finalized.

At present no design study has been undertaken for the beam dumps. There will be at least two types of dump: one to stand about 100 kW, for beam set-up at relatively low intensity, and one designed to absorb the full 4 MW beam. The former unit has a thermal power of the same order as the present SPS internal dump and a similar design can perhaps be used as a guideline. The design of the latter will need a dedicated study to address both radiation and thermo-mechanical issues (cooling, mechanical stresses, etc).

With the advance of the project, the present preliminary shielding and duct design will have to be confirmed by Monte Carlo simulations. The design of the beam dumps will need careful attention. Further issues which will have to be considered in a more advanced design are groundwater activation (although geological prospecting carried out in 1970 showed that at this depth there is no water table, this will have to be confirmed), as well as radioactive air and liquid releases. An aspect which will have to be carefully addressed is the induced radioactivity in the linac and surrounding structures (shielding, support structures, cables and cable-trays, etc.), also in view of assessing the amount of radioactive waste to be handled at the time of the facility's decommissioning.

5.2 Civil engineering

The main guidelines for the design of the civil-engineering parts of the linac were:

– to minimize the civil-engineering costs (e.g. by re-use of existing tunnels and infrastructure);

– to respect the tunnel depth and shielding specified by radiation protection;

– to provide an easy connection with the ISR tunnel, with the PS (clockwise injection) and with the ISOLDE area;

– to minimize the environmental impact.

Five alternative positions of the linac were compared. After an analysis of their advantages and disadvantages and a brief cost estimation, the advantages of the layout shown in Fig. 5.1 are clear. The linac tunnel and a parallel klystron gallery follow Route Gregory for 800 m immediately outside the existing CERN fence, on Swiss territory. For this solution, the connections with the ISR, the PS and ISOLDE can re-use a maximum of existing tunnels, and a cut-and-cover excavation technique can minimize the construction costs. The final environmental impact is minimum (most of the site is at present an empty grass field) and a maximum of existing buildings on the Meyrin site can be re-used. Access to the site is easy from the existing Route Gregory.

The overall length of the linac tunnel is 800 m, with cross-sectional dimensions of 4 m in width by 4.80 m in height. At the end of the linac, there is a 20 m long dump tunnel.

In order to maintain the slope of the linac tunnel to 1.4% as in the LEP straight sections, to avoid modifications to the cryostats, and to respect the shielding requirements imposed by radiation-protection considerations, the level of the top section of the tunnel is about 4 m below ground level at the start of the linac and about 20 m at the end (Fig. 5.2). Earth backfill will be placed on the top of the tunnel where the depth of the underside of the cover slab is less than 6 m.

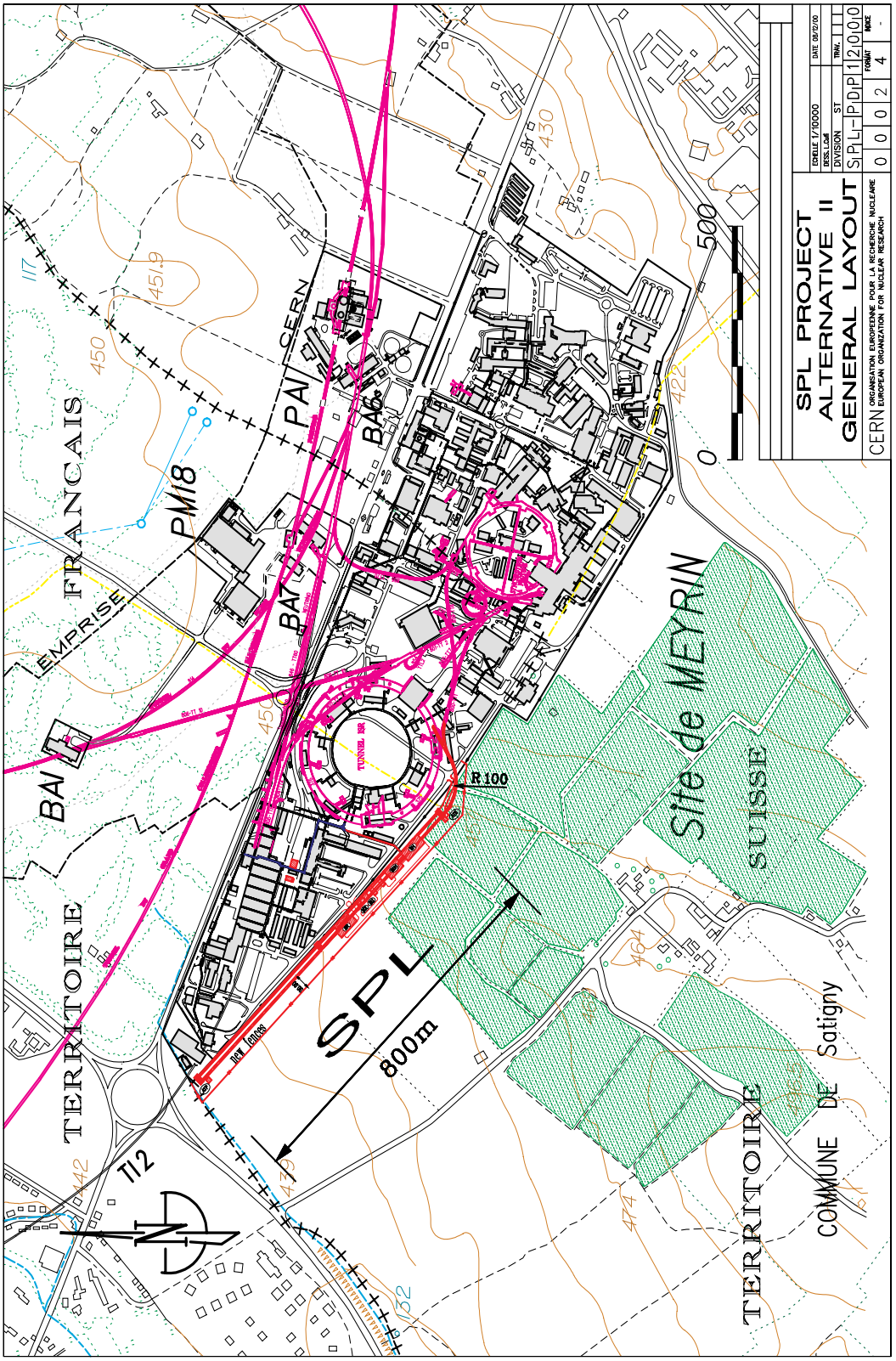

Fig. 5.1: Proposed layout of the linac facilities on the CERN Meyrin site.

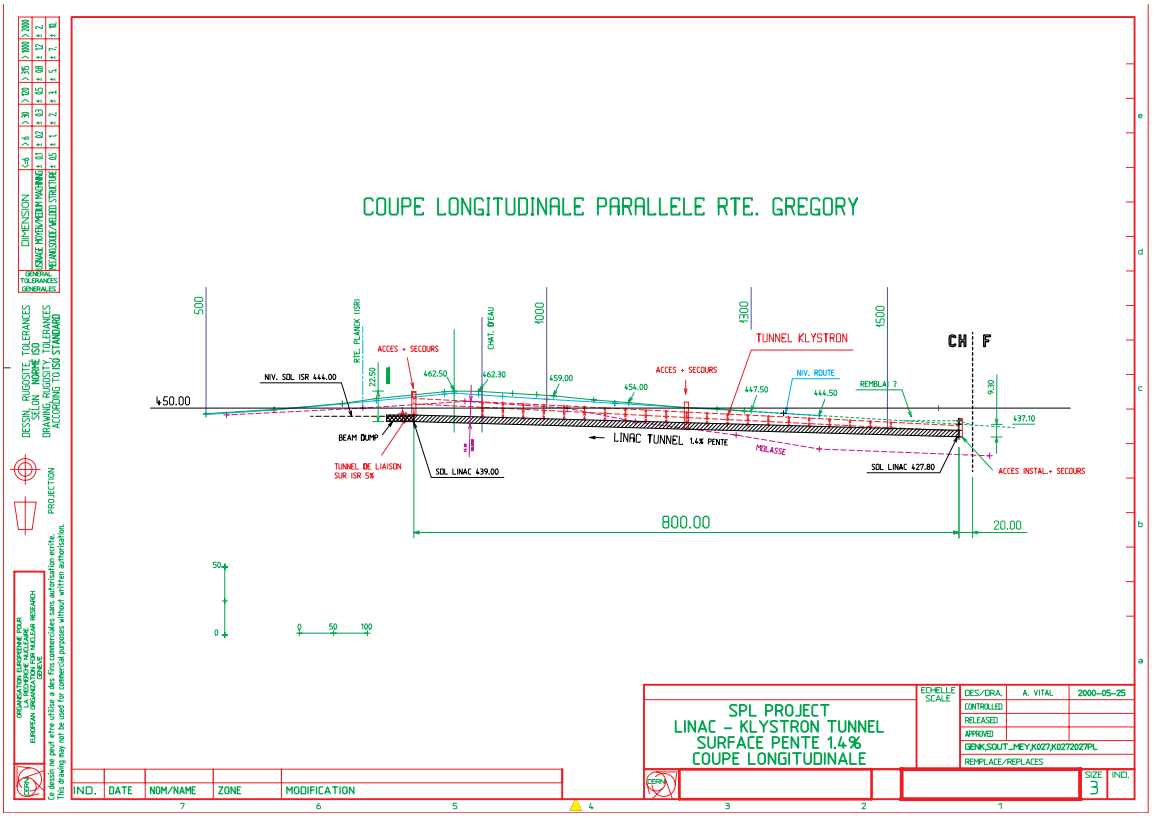

Fig. 5.2: Longitudinal section of the linac tunnel.

The underground structures are made of reinforced concrete with thickness of the order of 40 cm for walls, 60–70 cm for floors and covering slabs, to be determined more precisely at a later stage of the design. Figure 5.3 shows a transverse cut of the tunnel. Tunnel works are carried out using the cut-and-cover method (earthworks, diaphragm wall or sheet piling), optimizing the depth with reference to predicted costs and environmental impact. One access shaft is located at each end of the linac tunnel for transfer of the equipment. A third access to the linac will be located in the middle section of the tunnel. This involves narrow shafts next to the tunnel itself, with a staircase and access to/from the surface through a small shielded building. The large equipment will be introduced by the transfer tunnel of the ISR. Figure 5.4 shows a cross-section with access shaft.

Rather than considering 20 klystron buildings (dimensions $18 \times 16 \times 4.5$ m each), a tunnel alternative has been chosen in order to reduce the environmental impact. The klystron tunnel is 800 m long, with cross-sectional dimensions of 4 m in width by 4 m in height. The depth of the underside of the cover slab is about 1 m below ground level. This tunnel follows the natural slope of the ground and tunnel construction will also be carried out using the cut-and-cover method.

The length of the transfer tunnel linac–ISR is about 150 m and the minimum curvature radius imposed to avoid stripping losses is 100 m. The cross-sectional dimensions are the same as those of the linac tunnel. It will have a slope of about 3.5%, governed by the present location of the ISR. In this case, tunnel works are carried out using excavation by roadheader, this tunnel being too short to use a tunnel-boring machine. The level of the top section of the tunnel is about 14 m underground, and 6 m into the molasse.

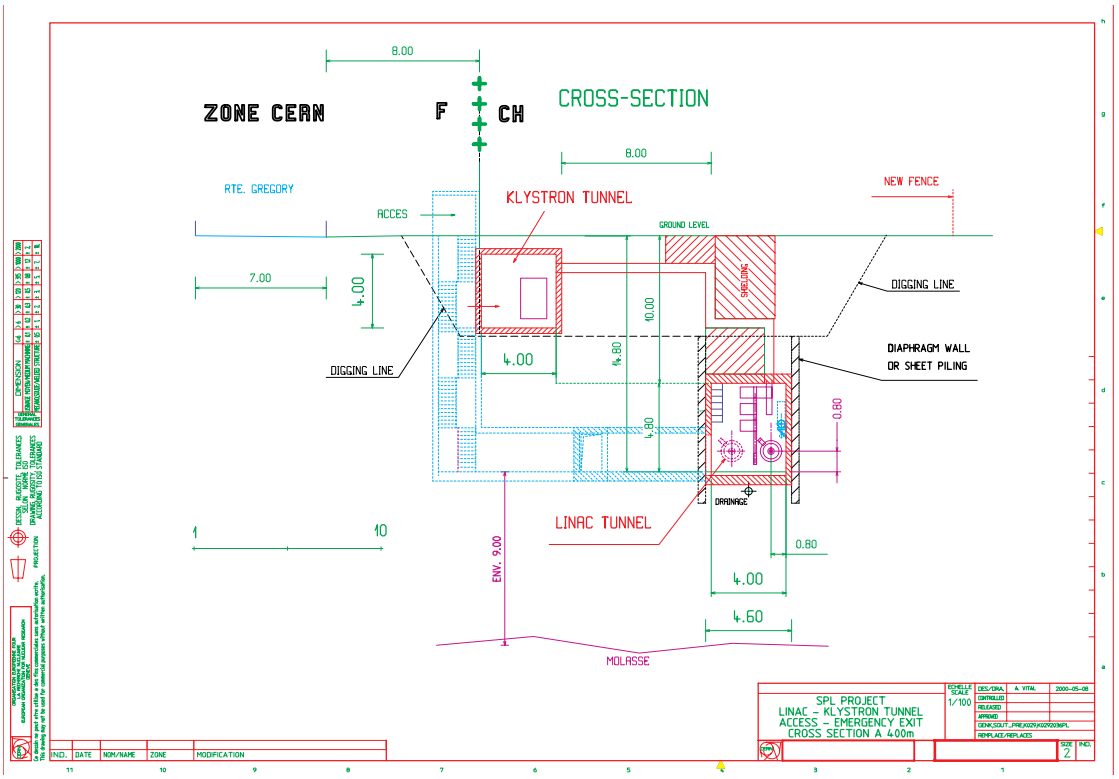

Fig. 5.3: Cross-section of the linac and klystron tunnels.

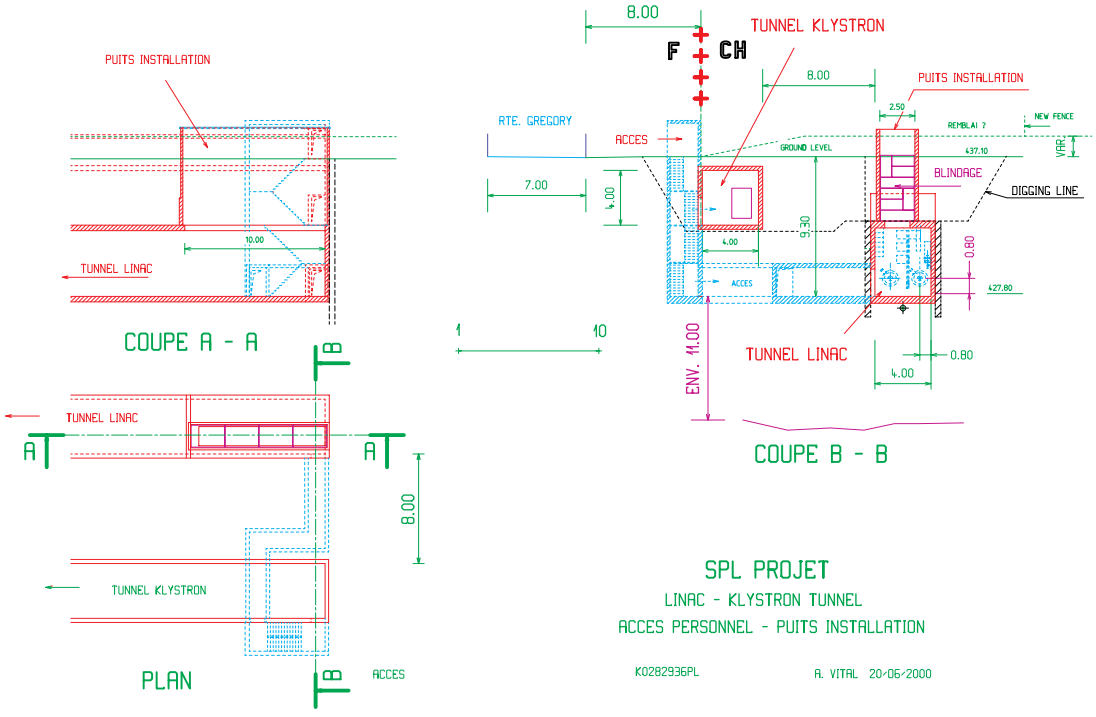

Fig. 5.4: Cross-section with access and access shaft.

The transfer tunnel is connected to both the ISR and the TT1 tunnel via a new cavern (Fig. 5.5). The TT1 tunnel, and further on the TT6 tunnel, connects the linac with the PS ring (clockwise). No civil-engineering works are necessary for this connection.

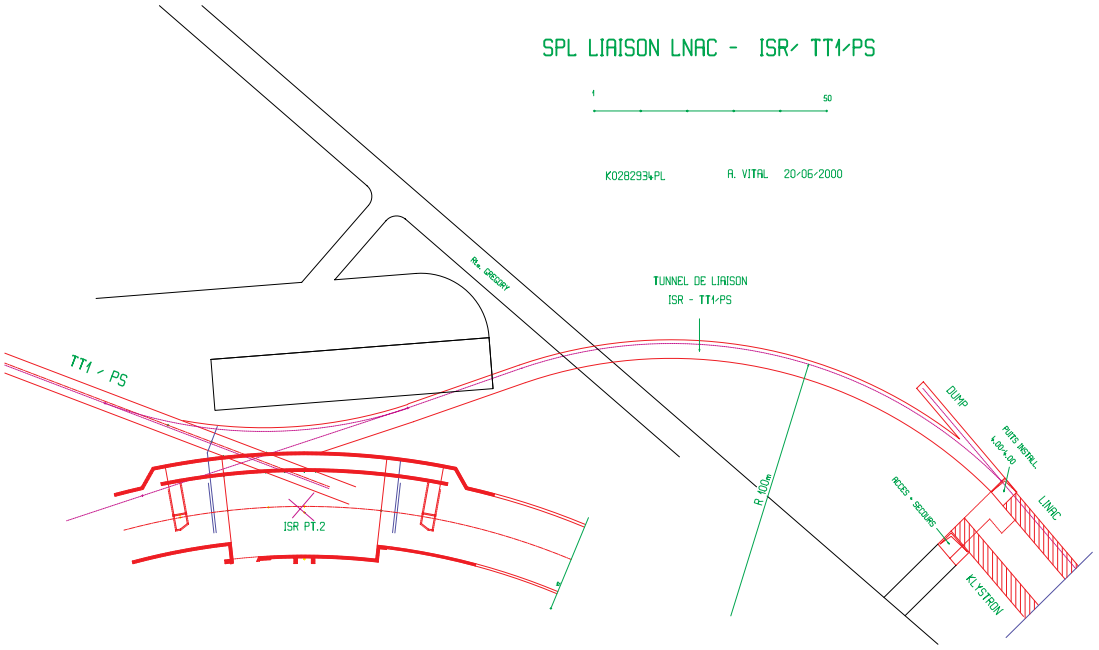

Fig. 5.5: Connection of the transfer tunnel to the ISR tunnel and to the existing transfer line to the PS.

The connection with ISOLDE (Fig. 5.6) is made via the TT6 tunnel. It requires a new tunnel of about 40 m length, including a dump of 10 m length. The tunnel floor level is horizontal, to avoid the risk of irradiation to Route Democrite, and crosses the existing TT70 tunnel, no longer in use. In this preliminary design, a vertical shaft links the transfer tunnel with the ISOLDE area (Fig. 5.7). The exact position and angle of the beam entering the area will be defined according to ISOLDE's future plans. Tunnel works are again carried out using excavation by roadheader.

For the services related to the machine, it is foreseen to re-use a large number of existing buildings and much infrastructure like the cooling towers (Building 274), technical galleries TP6, etc. For a preliminary analysis of the layout, all the new buildings have been placed on the new land to be acquired by CERN across Route Gregory (Fig. 5.8). The new surface buildings and related ancillary structures that are directly linked to the running of the machine are described in Table 5.2. In a final installation, some of the buildings could be placed instead in different positions inside the Meyrin site.

No additional road networks need to be created. The existing roads provide access to all surface buildings, to the shafts and the underground machine facilities (Route Gregory). However, some adaptation of the existing roads is likely to be required. Car parks and areas for handling of equipment are foreseen around the buildings and the shafts.

A new plot of land has to be integrated in the CERN Meyrin site, through negotiations with the relevant Swiss Authorities. Particular care has to be given to the final landscaping of this area.

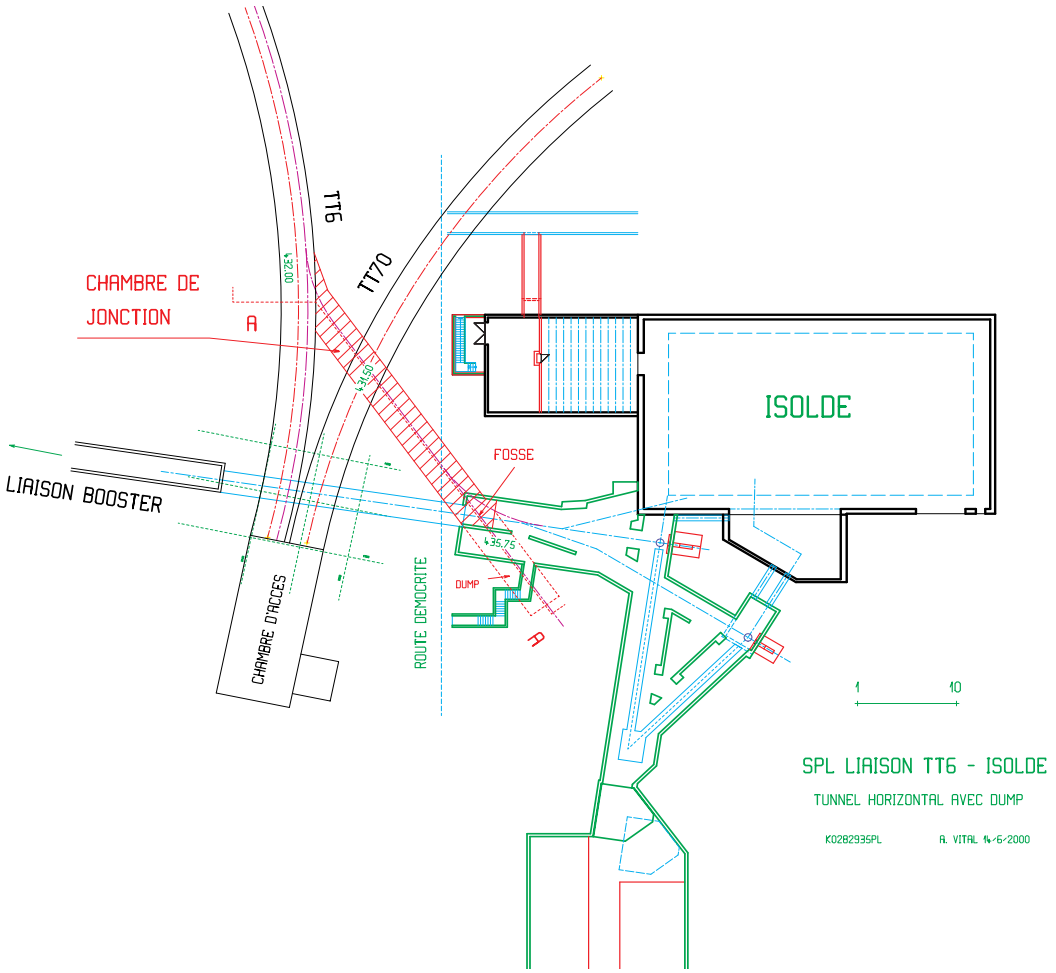

Fig. 5.6: Connection of the transfer tunnel to ISOLDE, plan view.

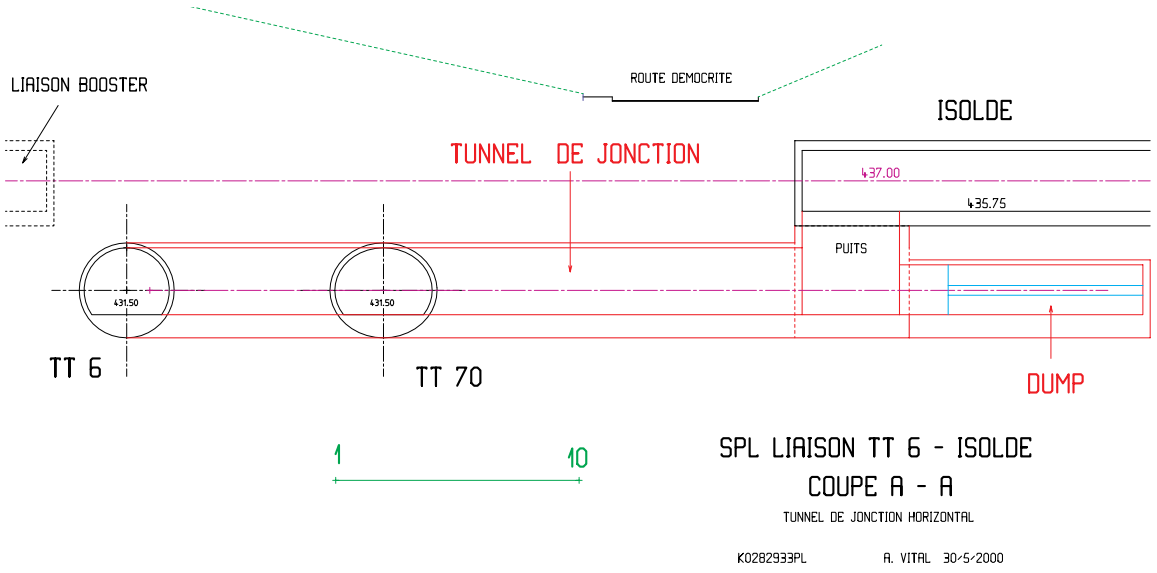

Fig. 5.7: Connection of the transfer tunnel to ISOLDE, vertical cut.

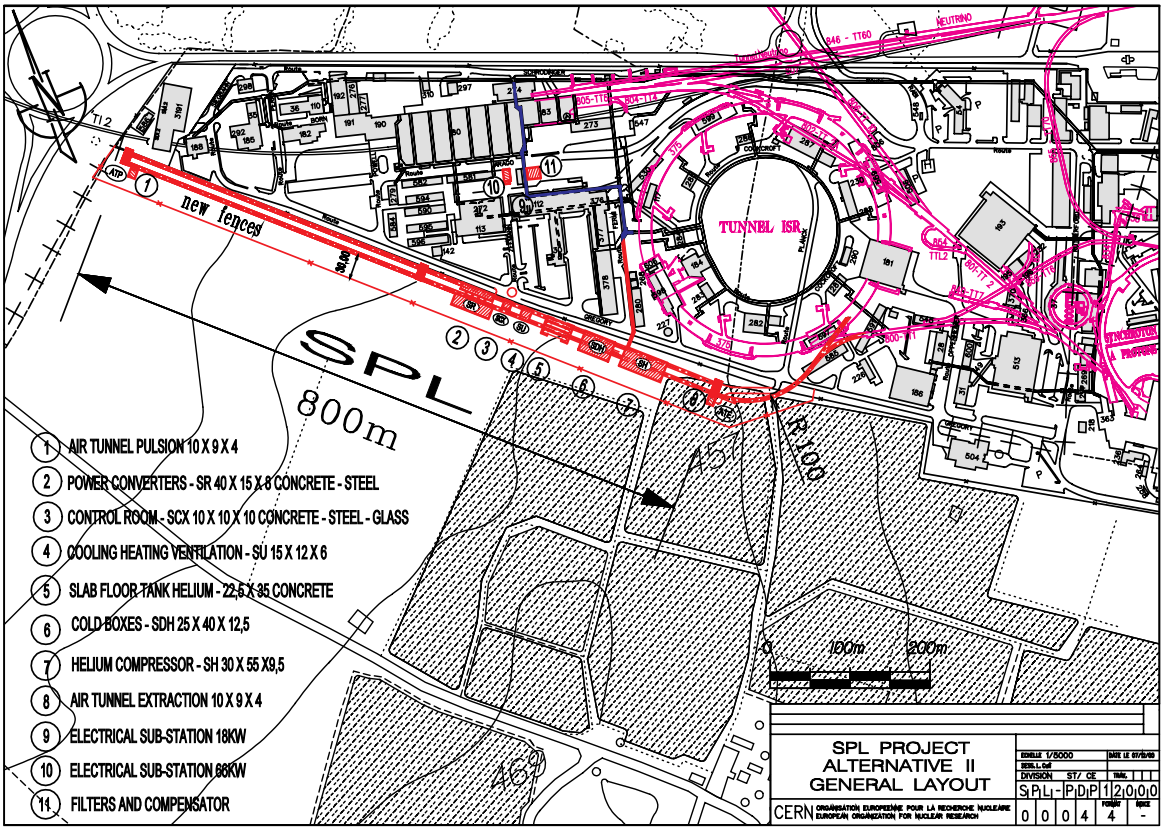

Fig. 5.8: Preliminary position of service buildings.

5.3 Cooling and ventilation

5.3.1 Primary cooling plant

The cooling is achived by means of cooling towers which dump into the atmosphere all the power dissipated as heat, both by machine elements and their facilities. The primary cooling circuit collects the water from the cooling towers' basin and delivers it to the different users, who can either use the primary water to directly cool their equipment (as in the case of cryo-compressors) or, when required by the process, to cool down the secondary circuits.

For the amount of cooling required by this project, the use of large cooling towers is mandatory. To minimize the cost of basic infrastructure, it is foreseen to convert an existing set of cooling towers in the nearby West Experimental Area (WEA), in Building 274. However some modifications to the existing plant layout will be necessary, like the replacement of the primary pumps to accommodate the new flow-rate and head requirements and also the refurbishment of the cooling-tower equipment (package, fan and power supplies).

The primary water will be routed along existing technical galleries and buildings to the vicinity of the existing Building 378, where the future cooling technical building (SU) will be situated. In spite of the cost of extended distribution networks, the investment that would be required if new cooling towers were to be built amply justifies the cost of the primary piping from the WEA cooling towers. It will then be used in the SU building for the cooling of the secondary circuits (demineralized or 'doped' water) in the machine (for which some 6 MW are needed), and in the cryogenics (SH) building for direct cooling of the two 16 kW cryoplants (requiring same 8 MW of cooling).

The cooling temperature is conditioned by the thermodynamic characteristics of the outside air, the final cold source. The cooling-tower water will reach temperatures of about 24 °C during the summer months in the Geneva region, which in turn entails temperatures of the order of 26 °C for the secondary circuits (demineralized or 'doped' water).

The services (two DN500 pipes) from the cooling towers (Building 274) will be routed mostly along existing technical galleries (TP6 up to Building 112) and then along a trench to be built from the south façade of Building 112 running along the car park opposite Building 30 up to Route Gregory, and from there to the future site of the SU building, near the Chateau d'eau (Building 227). The existing infrastructure (technical galleries) is used to the maximum extent in this way.

Table 5.2: Surface buildings.

Purpose	Name	Dimensions (m) Length × width × height	Materials	Particularities
Control room	SCX	10 × 10 × 10	Concrete–steel–glass	False floor under racks
Power converters	SR	40 × 15 × 8	Concrete–steel	False floor under racks Overhead crane 10 t
Helium compressor	SH	55 × 30 × 9.5	Concrete–concrete	Overhead crane 20 t
Cold boxes	SDH	40 × 25 × 12.5	Concrete–steel	Overhead crane 5 t
Slab floor tank helium		22.5 × 35	Concrete	–
Cooling–heating–ventilation	SU	15 × 12 × 6	Concrete–concrete	False floor 2 m Overhead crane 5 t
Electrical sub-station 18 kV		12 × 9 × 5	Concrete–concrete	False floor 2 m Overhead crane 5 t
Electrical sub-station 66 kV		15 × 12 × 5	Concrete–concrete	False floor 2 m Overhead crane 5 t
Air tunnel pulsion		10 × 9 × 4	Concrete–concrete	–
Air tunnel extraction		10 × 9 × 4	Concrete–concrete	–

Table 5.3 summarizes the primary cooling needs and the parameters defining the circuit.

Table 5.3: Primary cooling needs and cooling-circuit parameters.

Item	ΔT (K)	Power (kW)	ΔP (bar)	Flow rate (m^3/h)
Primary cooling SPL	15.6	6100	5	340
Cryo-compressors	7	8000	5	1200

5.3.2 Secondary cooling plant

The secondary cooling circuits are used when the process to be cooled requires a cooling medium other than mains water. This is usually the case for magnets and RF amplifiers where demineralized water is necessary. The secondary circuits extract the heat dissipated by the warm sources and convey this heat to the primary source via heat exchangers. The klystrons are a particular case in that they require a

somewhat lower resistivity of the secondary cooling circuit water, usually achieved by ‘doping’ (with some added salts) the demineralized-water circuit. The klystron cooling circuit is particularly complex, and the flow rate assumed in the following is underestimated. A reliable estimate will only be available at the end of the on-going detailed design of the circuit.

In order to further minimize the cost and complexity of the cooling facilities, it is foreseen to build ‘lumped’ cooling circuits to be shared amongst machine components which require similar cooling characteristics. The schematic diagram of the main cooling plant (housed in Building SU) is shown in Fig. 5.9.

It is customary to house as much of the equipment as possible in the cooling technical building, in order to simplify the associated operation and maintenance costs. However, as can be seen in Fig. 5.9, some minor circuits will be located outside the SU building. Such is the case for the beam dump, which will be in the non-accessible machine tunnels on account of the induced radioactivity.

The SU building would have a floor area of 15 m × 12 m and a height of some 5 m, with a false floor of some 2 m. Its location must be chosen in the proximity of Buildings 378 and 227, so as to minimize the length of the trench required for the primary services and to be as close as possible to the future linac tunnel, klystron gallery and the ISR ring. Tables 5.4 and 5.5 summarize the secondary and tertiary cooling circuits required.

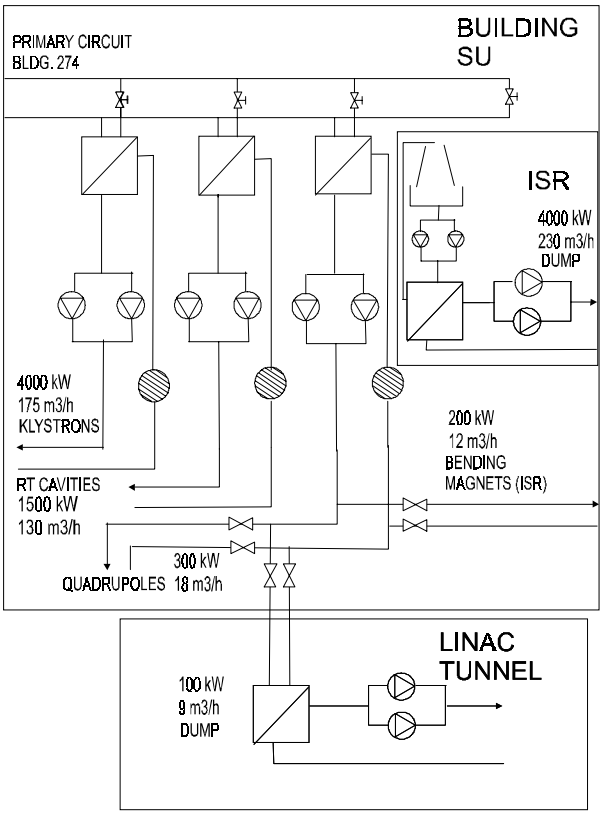

Fig. 5.9: Schematic diagram of the main cooling plant.

Table 5.4: Secondary circuits.

Item	Fluid	Power (kW)	Pmax (bar)	DT (K)	Flow rate (m^3/h)
Klystron	Doped water	4,000	8.5	20	175
RT cavities	Demineralized water	1,500	8.5	10	130
Magnets (quad)	Demineralized water	300	12	15	18
Magnets (bend)	Demineralized water	200	12	15	12
Dump linac	Demineralized water	100	12	15	6

Table 5.5: Tertiary circuits.

Item	Fluid	Power (kW)	ΔT (K)	Flow-rate (m^3/h)
Dump linac	Demineralized water	100	15	9

5.3.3 Chilled-water plant

The chilled-water plant provides the cold fluid (6 to 12 °C) necessary for the air conditioning of the different spaces and for the cooling of racks and electronics.

A power of about 600 kW is required for air conditioning and dehumidification of the linac tunnel and the klystron gallery. Owing to the presence of electronic components in the tunnel, the design temperature for the air is 25 °C. A system of refrigerating machines (chillers) is needed to provide chilled water at temperatures in the range of 6 to 12 °C.

Since there is no existing infrastructure available for chilled water, new chillers and the associated pump sets have to be installed. This can be done however in the existing building, so no civil engineering is required.

5.3.4 Heating, ventilation and air conditioning

Air handling units (AHUs) are needed for the heating, ventilation and air conditioning of underground and surface buildings and their equipment. For the ventilation of the linac tunnel and klystron gallery, two stations are foreseen. The basic layout consists of a supply station at one end of the underground structures (where outside air is drawn, filtered, dehumidified, cooled or reheated and finally blown into the tunnel and gallery) and an extraction station at the opposite end. This arrangement, although requiring more cooling capacity (the system has to run entirely on outside air which needs to be cooled from the outside to the necessary supply temperature), has a lower initial cost than a system with a lower cooling capacity running partially on recirculated air, which requires the return air to be ducted all along the tunnel. Table 5.6 presents the internal loads considered for cooling and ventilation.

Table 5.6: Ventilation loads.

Item	Internal load (kW)
Tunnel/gallery	50
Control room	30
SH	250 (ventilation only)

5.4 Electrical infrastructure

An estimation of the electrical power requirements for the different components of the linac facility is presented in Table 5.7. It must be noticed that the table lists MW, while the corresponding MVA will have to be determined at a later stage.

Table 5.7: Electrical power requirements.

RF system	24 MW
Cryogenics	10 MW
Cooling and ventilation	2 MW
Other	1 MW
General services	3 MW
TOTAL	40 MW

Probably a set of harmonics filters will be required to obtain a satisfactory mains quality with respect to harmonic distortion from the klystron power converters, and possibly a reactive power compensation system will be necessary to avoid voltage variations. The cryogenic system will load the power distribution system with motor-compressor sets, which constitute a linear and constant load.

The main distribution substation will be at the 18 kV level. Because of the high power needed, a 66 kV cable will be required from the Prévessin site together with a 66/18 kV substation, situated close to the 18 kV distribution substation.

The model for the 66/18 kV substation, the filter and the compensator will be the solutions applied to the LEP1 and LEP2 projects (Fig. 5.10). The rated power of the transformer will be 38 MVA, a size of which CERN already has six units, so no extra spares will be necessary. The 66 kV substation can be modelled on a solution already used several times. The 18 kV substation will be another copy of a solution used regularly since 1985. It is envisaged to install it in the existing SW substation, in order to minimize civil engineering, as long as there is enough available space. All auxiliary and safety systems will be the CERN standard solutions adopted for LEP.

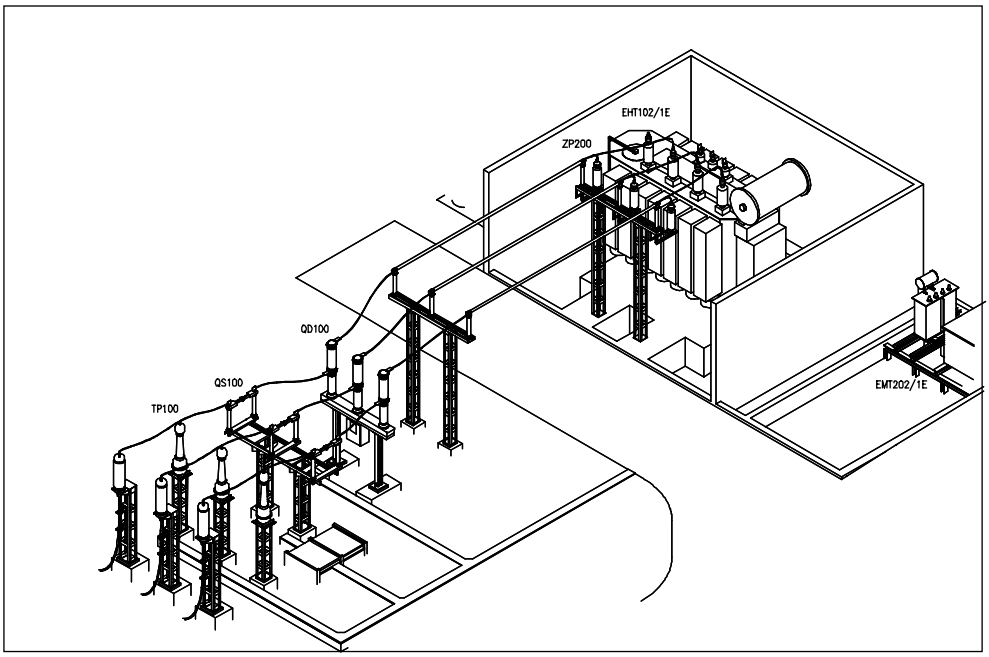

Fig. 5.10: Layout of a 66/18 kV substation.

The total power available from the present 400/66 kV system is 220 MVA: two transformers, each 110 MVA. The total foreseen requirements will be around 180 MW, with the LHC requirements estimated to be around 125 to 130 MW. As the load is well compensated, the difference between MW and MVA will be quite small.

Simply taking the power requirements for this new facility from the existing installation is in principle possible, but would mean that there is neither redundancy nor reserve for future extensions of the load. It is therefore proposed that an additional 400/66 kV transformer be added to the 400/66/ 18 kV substation. This will require the displacement of the 400 kV incomer and a complete new 400 kV bay in addition to the transformer.

The new electrical installations required will therefore be the following.

400 kV system: An additional 400 kV bay, including a 400/66 kV, 110 MVA transformer.

66 kV system: At the main 66 kV substation at Prévessin, SEH9, there is enough available space for one more incomer and one additional feeder. Although the power requirement is estimated at around 40 MVA, the cable link would be designed for 70 MVA, a standard cross-section that would allow later upgrades. A more detailed analysis and cost comparison would show whether the project should start with a 38 MVA or directly with a 70 MVA transformer, two standard sizes already existing at CERN. Using one of them would allow us to stay with standard solutions, fairly well adapted to the project. The 66/18 kV substation at Prévessin should be installed opposite the SW substation, where an open space is at present available.

18 kV system: To be installed, if possible, in conjunction with the SW substation. The two substations should be electrically separate, but using a part of the SW would save considerable civil-engineering costs. A first estimation points to a main switchboard with approximately fifteen 18 kV cubicles. The need for a more elaborate system, possibly with back-up supplies and a separation in ‘machine’ and ‘services’ switchboards, will have to be the subject of a more detailed study. The 18/0.4 kV transformers will be placed close to the users and connected to the substation by 18 kV PEX or EPR cables. The transformers for the klystrons can be recuperated from LEP, while the exact ratings of the other transformers have to be studied.

3.3 kV system: It should be installed in conjunction with the cryogenics installation, to save civil-engineering costs by using a part of the cryogenic building. A first estimation points to a switchboard with approximately twelve to fifteen 3.3 kV cubicles. It may be required to feed the system from two sources, depending on the wishes of the project. The 18/3.3 kV transformers will be placed close to the 3.3 kV substation and connected to the substation by PEX or EPR cables.

General service installations: General services in the buildings as well as auxiliary and safety systems, would be designed using the standard solutions applied CERN-wide by the electrical service since the construction of LEP.

5.5 Access control and safety systems

The SPL infrastructure being considered as a primary beam area, an access control system and a machine interlock safety system will be installed to ensure personnel and equipment protection. The SPL infrastructure will be subdivided in three areas equipped with the usual CERN equipment dedicated to primary beam area access (controlled access doors, search sectors).

The personnel protection is ensured by the machine interlock system; thus, in access mode, a VETO signal avoids any activation of specific machine equipment (beam stopper, RF modulators, power supplies).

All the access procedures will be supervised by an operator from the PS Main Control Room (MCR). As for the existing PS primary beam areas, warnings will be activated in the SPL areas before beam operation.

The fire and gas detection policy will be based on the CERN Fire Protection Code [66] and on the CERN Flammable Gas Code [67]. CERN policy is to protect first and foremost the integrity of the people inside the installations, followed by the environment and the equipment. Consequently, and following the advice of TIS Division, adequate alarm systems will be installed in the linac tunnel and buildings.

6. HIGHER BEAM POWER OPTION

The basic challenge of a Neutrino Factory is to provide the required number of high-energy muons per year in the high-energy storage ring. Since capturing and cooling muons is complex and costly, it has to be balanced against the brute force possibility of delivering a larger proton flux onto the target. A proton beam power of 4 MW is being used in the present design because of estimated limitations in the target area, but not in the linac. It can be increased to 24 MW without substantial modifications to the accelerator by increasing the duty factor to 100%. This would be beneficial for the regulation of the field in the superconducting cavities, and neutral for the equipment which is already running continuously (H^- source, quadrupoles, etc.). It would involve a review of the following systems:

– the beam collector after the low-energy chopper, because it receives six times more particles when the linac operates continuously;

– the room-temperature part of the accelerator (up to 120 MeV) where the cooling system must evacuate 85% of the RF power because it is dissipated in the structures (up to 8.2 MW in continuous operation);

– the RF amplifier installations (up to 32 MW mean RF power in continuous operation instead of 10 MW), increasing the cooling and the capabilities of the power supplies (up to 22 LEP-type power converters instead of six);

– the cryogenics cooling capacity to evacuate the heat from the superconducting RF cavities at 4.5 K (up to 75 kW equivalent power at 4.5 K instead of 32 kW). Although adding new cryoplants to increase the cryogenic power available could be possible, the cryogenics distribution system (cryogenic transfer line and cryostat) could be critical;

– the management of beam loss and irradiation, because the limit of 1 W/m of uncontrolled beam loss along the accelerator has to be kept (up to a six-fold improvement for running continuously); shielding should also be adapted around collimation dumps;

– the electrical power distribution, because the electrical power requirement would approach 100 MW when running the facility continuously (a comparison of the linac power requirement for the presently foreseen duty cycle and for continuous operation is reported in Table 6.1);

– the size and number of surface buildings providing these upgraded services (× 2).

Table 6.1: SPL power requirements.

Item	Design case	Continuous beam case (estimates)
Mean beam power	4 MW	24 MW
Electrical power consumption		
– RF (mean RF power)	24 MW (12 MW)	64 MW (32 MW)
– Cryogenics (cooling power at 4.5 K)	8 MW (32 kW)	20 MW (75 kW)
– Cooling & ventilation	2 MW	6 MW
– Other & general services	4 MW	5 MW
Total electrical power consumption	38 MW	95 MW

Moreover, such an increase of the duty cycle will have major consequences downstream of the linac, and in particular:

– for the accumulator and compressor rings, where difficulties can be foreseen concerning the stripping of H^- ions (should foil stripping be replaced by laser stripping [68]?) and the irradiation due to losses;
– for the target itself, the proton dump and the pion/muon collection system, which have to be adapted;
– in the muon complex, where the heat dissipation in the pulsed devices and the total power consumption must stay manageable.

7. OTHER APPLICATIONS OF THE FACILITY

7.1 Other physics interests

Although less extensively studied so far than the physics provided by muon storage rings, the high-intensity proton driver will offer high-energy physics opportunities that could be interesting in their own right, and perhaps available on a shorter time-scale.

7.1.1 High-intensity stopped muon physics

Lepton flavour violations, already seen in neutrino oscillations, are expected at some level in muon decays, especially in several classes of supersymmetric models [69–72]. The availability of a high-power, high-duty-factor proton beam could provide opportunities in stopped muon physics if the rate of muons was increased by several orders of magnitude over presently planned experiments [73, 74]. At present the PSI runs a 1 MW d.c. proton beam at 590 MeV, with a muon target of typically 5% efficiency. A programme at CERN could include experiments such as rare decays $\mu \rightarrow e\gamma$, $\mu \rightarrow eee$ searches or muon conversion $\mu N \rightarrow eN$, and improvements in muon decay properties.

The search for rare decays requires a d.c. beam (or a time structure with a repetition rate faster than the muon lifetime), in sharp contrast with the front end of the neutrino factory. An almost d.c. beam could be obtained by inserting a thin internal target inside the accumulator ring. To avoid the evaporation of this target and proton beam blow-up, one should consider a thin rotating solid target in a relatively low-beta insertion to be added to the accumulator lattice. This should be coupled to a large aperture capture solenoid and possibly RF phase rotation to provide the required gains in intensity. Studies are now beginning in order to understand the feasibility and achievable performance of this option.

7.1.2 Low-energy muon neutrino beams

In collisions of 2.2 GeV protons, no kaons or strange particles are produced. Therefore a conventional, wide-band, horn-focused neutrino beam from pion decay could be envisaged, with relatively small and controllable electron neutrino contamination, at a typical energy of 200 to 300 MeV. The main physics objective would be the search and study of $\nu\mu \leftrightarrow \nu_e$ oscillations. The target, horn and decay tunnel would be very similar or perhaps identical to those of the neutrino factory.

Although it appears unlikely that flux purity and normalization, as well as low-energy neutrino cross-sections could be understood with sufficient accuracy to allow the type of precision oscillation physics available at the neutrino factory itself, this option is presently being investigated.

7.2 Possible use of the linac for a neutron facility

Neutrons play an increasing role in materials research, engineering, chemistry, biology and biotechnology. For some 4000 scientists in Europe, neutron beams have become an indispensable tool for their research programmes [75]. In contrast to the increasing demand from users, there is a predicted decline in the number of neutron sources. The planned SNS in the US and the foreseen ESS and Austron facilities in Europe propose new possibilities. Unfortunately only the SNS has been approved so far.

In a previous report [4] it has been shown that this linac, which was conceived as an injector to the PS only, could be operated at a higher duty cycle of up to 5% for the production of spallation neutrons. In this scenario, beam powers between a few kilowatts and one megawatt (depending on the pulse structure and the use of the PS as the intermediate ring) looked feasible. The SPL as it is proposed now as an injector for a neutrino factory runs with a beam power of 4 MW. This is not yet the limit of this machine. A higher duty cycle or a higher beam current are not ruled out.

A pulsed source of neutrons has definite advantages compared to a reactor [75]. Although there are users for millisecond pulses, quite a strong community needs shorter pulses like 50–100 μs or even down to 10–20 μs [76, 77]. It should be recalled that the neutron pulse is lengthened due to the action of the moderator (to produce thermal or even much colder neutrons). Hence, to achieve a 10 μs pulse for example, the proton pulse must not be longer than a few microseconds.

The scenario for the neutrino factory contains an accumulator ring, which compresses the linac pulses to 3.3 μs. The available power is now determined by the linac current, its duty cycle, and the permissible losses, but also by the stripping foil in the accumulator. At present there is a safety margin if compared to the 1996 ESS design. A modest increase of the linac power to a total of 5 MW (leaving 1 MW for the neutron production) might be tolerable for the foil in its present design. Different schemes (increase of duty cycle, pulse length) would be possible, as well as 'stealing' pulses from the train foreseen for the neutrino factory, e.g. every 5th pulse, resulting in a 15 Hz 1 MW neutron source. The use of the proposed linac and accumulator ring for a spallation neutron source would of course require an additional target station and the necessary beam lines. More detailed work is necessary to assess the full benefits of this scenario.

ACKNOWLEDGEMENTS

Among the many who have contributed to this study, the authors would particularly like to acknowledge the help of P. Bourquin, D. Cornuet, B. Frammery, G. Geschonke, H. Frischholz, J.M. Lagniel (CEA), A. Pisent (INFN), J.P. Potier, J.P. Royer, R. Ryne (LANL) and M. Sassowski.

References

[1] B. Autin, A. Blondel, J. Ellis (eds.), Prospective Study of Muon Storage Rings at CERN, CERN 99–02.

[2] B. Autin (ed.), Proc. ICFA/ECFA Workshop Neutrino Factories based on Muon Storage Rings (NuFact'99), Lyon, France, 5–9 July 1999, Nuclear Instrum. Methods **A451** (2000) 1.

[3] R. Garoby, M. Vretenar, Proposal for a 2 GeV Linac Injector for the CERN PS, PS/RF/Note 96–27.

[4] D. Boussard, R. Cappi, R. Garoby, H. Haseroth, C.E. Hill, P. Knaus, A.M. Lombardi (ed.), M. Martini, P.N. Ostroumov, J.M. Tessier, M. Vretenar (ed.), Report of the Study Group on a Superconducting Proton Linac as a PS Injector, CERN/PS 98–063.

[5] C. Rubbia, J.A. Rubio, A Tentative Programme towards a Full Scale Energy Amplifier, CERN/LHC 96–11.

[6] D. Boussard, E. Chiaveri, G. Geschonke, J. Tuckmantel, Preliminary Parameters of a Proton Linac using the LEP2 RF System when Decommissioned, SL–RF Technical Note 96–4.

[7] B. Autin, Low Energy Proton Driver for a neutrino Factory, Proc. of HIMUS99 Workshop, Tsukuba, 1999 (to be published) and CERN/PS/2000–067 (PP), NF Note 047.

[8] H. Haseroth for the NFWG, Status of Studies for a Neutrino Factory at CERN, Proc. EPAC 2000, Vienna, June 2000 and CERN/PS 2000–026 (PP).

[9] B. Autin, A. Blondel, J.-P. Delahaye, R. Garoby, H. Haseroth, K. Hübner, C.D. Johnson, E. Keil, A. Lombardi, H. Ravn, H. Schönauer, The CERN Neutrino Factory Working Group. Status Report and Work Plan, CERN NuFact Note 28 (2000).

[10] B. Autin, R. Cappi, M. Chanel, J. Gareyte, R. Garoby, M. Giovannozzi, H. Haseroth, I. Hofmann, S. Koscielniak, M. Martini, E. Métral, D. Möhl, C. Prior, G. Rees, K. Schindl, H. Schönauer, Design of a 2.2 GeV Accumulator and Compressor for a Neutrino Factory, EPAC 2000, Vienna, June 2000 and CERN/PS 2000–011.

[11] F. Dydak (spokes-person), Proposal to study the hadron production for the neutrino factory and for the atmospheric neutrino flux, CERN–SPSC / 99–35.

[12] A. Lombardi, A 40–80 MHz system for phase rotation and cooling, CERN NuFact Note 34 (2000).

[13] LHC Conceptual Design, CERN/AC/95–05 (LHC).

[14] J. Vervier (ed.), J. Äystö (ed.), S. Galès (ed.) et al., Nuclear physics in Europe: highlights and opportunities, Nuclear Physics European Collaboration Committee (NuPECC), Garching, December 1997.

[15] The NuPECC working group on Radioactive Nuclear Beam Facilities, NuPECC Report, April 2000, http://www.nupecc.org.

[16] U. Georg, R. Catherall, T. Giles, O.C. Jonsson, U. Koester, E. Kugler, J. Lettry, T. Nilsson, H. Ravn, H. Simon, C. Tamburella, U.C. Bergmann, A.R. Junghans, K.-H. Schmidt and the ISOLDE Collaboration, Isotope production comparison at ISOLDE with 1 GeV and 1.4 GeV protons, Proceedings of RNB-5, Divonne, April 2000, to be published.

[17] E. Forkel-Wirth, A. Muller, F. Pirotte, Reflections on Super-ISOLDE, CERN/TIS–RP/TM/2000–18.

[18] J.R.J. Bennett, C.J. Densham, P.V. Drumm, W.R. Evans, G.R. Murdoch, V. Panteleev and M. Holding, The design and development of the RIST target, Nuclear Instrum. Methods **B126** (1197) 117.

[19] J. Peters, Negative ion sources for high energy accelerators, Rev. Sci. Instrum. **71** (1999) 1069–1074.

[20] M. Bacal, A.M. Bruneteau, C. Deniset, L.I. Elizarov, F. Sube, A.Y. Tontegode, Effect of cesium and xenon seeding in negative hydrogen ion sources, Rev. Sci. Instrum. **71** (1999) 1082–1085.

[21] Y.S. Hwang, G.H. Lee, Feasibility study of a new negative ion source using a transformer coupled plasma source, Rev. Sci. Instrum. **71** (1999) 943–945.

[22] O. Fukumasa, M. Matsumori, Electron cyclotron resonance negative ion source, Rev. Sci. Instrum. **71** (1999) 935–938.

[23] A. Takagi, Y. Mori, A 2.45 GHz microwave negative hydrogen source, Rev. Sci. Instrum. **71** (1999) 1042–1044.

[24] M. Tanaka, K. Amemiya, Negative ion beam production by a microwave ion source equipped with a magnetically separated double plasma cell system, Rev. Sci. Instrum. **71** (1999) 1125–1127.

[25] J.-M. Lagniel et al. (20 authors), Status and new developments of the high intensity electron cyclotron resonance source light ion continuous wave and pulse mode, Rev. Sci. Instrum. **71** (1999) 830–835.

[26] E. Surrey, AEA Technology. Private Communication.

[27] M. Weiss, The RFQ2 complex: the future injector to CERN Linac2, Proc. EPAC'92, Berlin, 1992 and CERN/PS 92–34 (HI).

[28] J. Staples, M. Hoff, C. Chan, All electrostatic split LEBT test results, Proc. Linac 96, Geneva, 1996, p. 157.

[29] D. Schrage et al. (23 authors), CW RFQ Fabrication and Engineering, Proc. Linac 98, Chicago, 1998, p. 679.

[30] R. Ferdinand P.-Y. Beauvais, R. Duperrier, A. France, J. Gaiffier, J.-M. Lagniel, M. Painchault, F. Simoens, P. Balleyguier, Status Report on the 5 MeV Iphi RFQ, Proc. Linac 2000, Monterey, 2000.

[31] A. Pisent, M. Comunian, A. Palmieri, G. Lamanna, D. Barni, TRASCO RFQ, Proc. Linac 2000, Monterey, 2000.

[32] A. Ratti, C. Fong, M. Fong, R. MacGill, R. Gough, J. Staples, M. Hoff, R. Keller, S. Virostek, R. Yourd, Conceptual Design of the SNS RFQ, Proc. Linac 98, Chicago, 1998, p. 276.

[33] S. Kurennoy, J.F. Power, Meander-Line Current Structure Development for SNS Fast Chopper, Proc. Linac 2000, Monterey, 2000.

[34] W. Bruns, Improved GdfidL with Generalized Diagonal Fillings and Reduced Memory and CPU Requirements, ICAP 98, 1998.

[35] M. Paoluzzi, Design of 1 kV Pulse Amplifier for the 2.2 GeV Linac Beam Chopper, CERN PS/RF/Note 2000–018.

[36] J. Staples, D. Oshatz, T. Saleh, Design of the SNS MEBT, Proc. of Linac2000, Monterey, 2000.

[37] F. Gerigk, M. Vretenar, Design of the 120 MeV Drift Tube Linac for the SPL, CERN–Nufact–Note 37.

[38] J. Billen, F. Krawczyk, R. Wood, L. Young, A New RF Structure for Intermediate-Velocity Particles, Linac 94, Tsukuba, 1994, p. 341.

[39] H. Takeda, PARMILA, LA–UR–98–4478.

[40] C. Benvenuti, N. Circelli, M. Hauer, Niobium Films for Superconducting Accelerating Cavities, Appl. Phys. Lett. **45** (1984) 583–584.

[41] R. Losito, Design and test of a 4-cell $\beta = 0.7$ cavity, CERN SL–Note–2000–047–CT.

[42] P. Brown, O. Brunner, A. Butterworth, E. Ciapala, H. Fritscholz, G. Geschonke, E. Peschardt, J. Sladen, Performance of the LEP200 Superconducting RF System, 9th Workshop on RF Superconductivity, Santa Fe, November 1999, CERN–SL–RF–99–075.

[43] O. Aberle, D. Boussard, S. Calatroni, E. Chiaveri, E. Häbel, R. Hanni, R. Losito, S. Marque, J. Tückmantel, Technical Developments on Reduced β Superconducting Cavities at CERN, PAC 1999, New York, 1999.

[44] C. Benvenuti, D. Boussard, S. Calatroni, E. Chiaveri, J. Tückmantel, Production and Test of 352 MHz Niobum-Sputtered Reduced-β Cavities, Proc. 8th Workshop on RF Superconductivity, Abano Terme, Italy, 6–10 Oct. 1997, LNL–INFN–133–98, pp. 1038–1049.

[45] R. Losito, Design of a β = 0.66 monocell cavity, CERN SL–Note–98–008–RF.

[46] F. Gerigk, Beam Dynamics in the Superconducting Section of the SPL (120 MeV–2.2 GeV), CERN PS/RF Note 2000–009, NF Note 24.

[47] J. Qiang, R.D. Ryne, S. Habib, V. Decyk, An Object-Oriented Parallel Particle-In-Cell Code for Beam Dynamics Simulation in Linear Accelerators, J. Comput. Phys. **163**, (2000) 1–18.

[48] F. Gerigk, Bunch Stretching in the Transfer Line between SPL and Accumulator and Optimization Against Initial Energy and Phase Jitter, CERN NF Note 50.

[49] J. Tuckmantel, SPLinac, A Program to Simulate SC Linac RF Systems with Beam, CERN SL–Note–2000–053 (November 2000).

[50] J. Tuckmantel, Simulation of the SPL SC RF System with Beam using SPLinac, CERN SL–Note–2000–054 (November 2000).

[51] B. Aune et al. (53 authors), Superconducting TESLA Cavities, Phys. Rev. Spec. Topics: Accel. and Beams, Vol. 3, 092001 (2000).

[52] A. Mosnier, J.M. Tessier, Field Stabilization studies for TESLA, TESLA 94–16.

[53] S. Simrock, Advances in RF control for high gradients, Proc. of the IX Workshop on RF superconductivity, 1–5 November 1999, Santa Fe (to be published).

[54] G. Arduini, R.L. Martin, S. Rossi, M. Silari, Vacuum and Magnetic Field Constraints in a H^-/ light ion Synchrotron, Nuclear Instrum. Methods **A346** (1994) 557–564.

[55] G.H. Gillespie, Phys. Rev. **A15** (1977) 563 and **A16** (1977) 943.

[56] L. Scherk, Can. J. Phys. **57** (1979) 558.

[57] G.M. Stinson, W.C. Olsen, W.J. McDonald, P. Ford, D. Axen, E.W. Blackmore, Nuclear Instrum. Methods **74** (1969) 333, A.J. Jason et al., IEEE Trans. Nucl. Sci. **NS–28** (1981) 2704.

[58] P. Proudlock, H.W. Isch, The Power Converters for the RF Klystrons of LEP, CERN SL/90–33 (PC).

[59] F. Bordry, private communication.

[60] H. Frischholz, private communication.

[61] M. Sanmarti, S. Claudet, SPL Cryogenics, CERN LHC Note 2000–01A.

[62] H. Nakashima, N. Sasamoto, Y. Sakamoto, J. Kusano, K. Hasegawa, H. Handa, K. Hayashi, K. Yamada, T. Abeet, Estimation of activity and dose distributions around a proton linac induced by beam spill, J. Nucl. Sci. and Technology, Supplement 1, p. 870–874 (March 2000).

[63] CERN Radiation Safety Manual, Safety Code F (1996).

[64] A. Fassò, K. Goebel, M. Höfert, J. Ranft, G.R. Stevenson, Shielding against high energy radiation. Landolt-Börnstein, Numerical data and functional relationships in science and technology, New series, Group I: nuclear and particle physics, Volume 11, ed. H. Schopper (Springer-Verlag, Berlin, 1990).

[65] R.H. Thomas and G.R. Stevenson, Radiological safety aspects of the operation of proton accelerators, IAEA Technical Reports Series No. 287, IAEA, Vienna (1988).

[66] CERN Fire Protection Code E Rev., Revision 1995.

[67] CERN Flammable Gas Safety Code G Rev., Revision 1996.

[68] R.T. Lee, J. S. Fraser, C.D.P. Levy, Laser stripping of the TRIUMF H^- beam, Proc. PAC 1989, Chicago, 1989, p. 414 and TRI PP 89–17.

[69] R. Barbieri, L. Hall, Phys. Lett. **B338** (1994) 212.

[70] R. Barbieri, L. Hall, A. Strumia, Nucl. Phys. **B445** (1995) 445.

[71] J. Ellis, M.E. Gomez, G.K. Leontaris, S. Lola, D.V. Nanopoulos, Charged-Lepton-Flavour Violation in the Light of the Super-Kamiokande Data, Eur. Phys. J. **C14** (2000) 319–334.

[72] Y. Kuno and Y. Okada, Muon Decay and Physics Beyond the Standard Model, hep–ph/9909265 (1999), to appear in Review of Modern Physics.

[73] T. Mori (spokesperson), Search for $\mu+ \rightarrow e+\gamma$ down to 10^{-14} branching ratio, Research Proposal to the Paul Scherrer Institute, R–99–051.

[74] W. Molzon (spokesperson for the MECO Collaboration), Search for $\mu N \rightarrow eN$ with a sensitivity below 10-16, AGS proposal P940, 1997.

[75] J. Kjems, A.D. Taylor, J.L. Finney, H. Lengeler, U. Steigenberger (eds.) ESS A Next Generation Neutron Source for Europe The European Spallation Source, ESS–96–53–M, March 1997, Volume I.

[76] J. Kjems, A.D. Taylor, J.L. Finney, H. Lengeler, U. Steigenberger (eds.) ESS A Next Generation Neutron Source for Europe The European Spallation Source, ESS–96–53–M, March 1997, Volume II.

[77] H. Scherm, private communication.

APPENDIX

DESIGN PARAMETERS AND LAYOUT AS AT END 2000

a. Beam parameters for the main SPL users

Table 1: Beam parameters from the Neutrino Factory proton driver (after accumulator and compressor rings).

Pulse duration	3.18 μs
Time between bunches (RF frequency)	22.7 ns (44.025 MHz)
Number of bunches	140
r.m.s. bunch length	1 ns
Number of protons per bunch	1.06×10^{12}
Number of protons per pulse	1.49×10^{14}
Total longitudinal emittance ε_l	0.1 eVs
Transverse r.m.s. emittance	50 μm

Table 2: Tentative parameter list of possible beams at low energy in the PS machine at T = 2.2 GeV.

Beam	N_b	h	ε_l	τ_b	ε_x*	ε_y*	ΔQ_x	ΔQ_y
	[$\times 10^{11}$]		[eVs]	[ns]	[μm]	[μm]		
LHC ‘ultimate’	8.3	21	0.6	60	1	1	0.24	0.39
High intensity for SPS	25	16	0.8	75	4	6	0.21	0.21

Table 3: Tentative parameters of the ISOLDE beam.

Particles	H^-
Mean current	2 to 200 μA
Particles per pulse	1.6 to 80×10^{11}
Repetition frequency	75 Hz
Kinetic energy	2.2 GeV
Additional energies for variable energy option	120 MeV – 237 MeV 389 MeV – 1080 MeV

b. Linac beam parameters and layout

Table 4: Main linac design parameters.

Particles	H^-
Kinetic energy	2.2 GeV
Mean current during pulse	11 mA
Repetition rate	75 Hz
Beam pulse duration	2.2 ms
Number of particles per pulse	1.5×10^{14}
Number of particles per second	1.1×10^{16}
Duty cycle	16.5%
Mean beam power	4 MW
RF and bunch frequency	352.2 MHz
Chopping factor	40%
Mean bunch current	18.4 mA
Overall length	799 m
Peak RF power	32 MW
Total main power	38 MW
Transverse r.m.s. emittance (norm.)	< 0.6 μm
Longitudinal r.m.s. emittance	< 0.6 π ° MeV < 15 μeVs
Bunch length at accumulator, total	0.5 ns
Energy spread at accumulator, total	0.4 MeV
Energy jitter at accumulator, between pulses (max.)	±2 MeV

Table 5: Linac layout.

Section	Input energy (MeV)	Output energy (MeV)	Number of cavities	Peak RF power (MW)	Number of klystrons	Number of tetrodes	Length (m)
		(MeV)					
Source, LEBT	–	0.045	–	–	–	–	3
RFQ1	0.045	3	1	0.4	1	–	3
Chopper line	3	3	5	0.3	–	5	6
RFQ2	3	7	1	0.5	1	–	4
DTL	7	120	100	8.7	11	–	78
SC – reduced β	120	1080	122	10.6	12	74	334
SC – LEP	1080	2200	108	12.3	18	–	345
Debunching	2200	2200	8	–	1	–	26
Total			337	32.8	44	79	799

c. Main parameters for the different linac sections

Table 6: Preliminary source parameters.

Particles	H^-
Extraction voltage	45 kV
Max. pulse length	2.32 ms
Repetition rate	75 Hz
Extracted current	30 mA
Transverse emittance (r.m.s., norm.)	0.2 π mm mrad

Table 7: Main RFQ parameters.

	RFQ1	RFQ2
Input energy	45 keV	3 MeV
Output energy	3 MeV	7 MeV
Frequency	352 MHz	352 MHz
Voltage	90 kV	90 kV
Maximum electric field	34 MV/m	34 MV/m
Length	2.6 m	3.9 m
Shunt impedance	60 kΩ m	60 kΩ m
Power losses	360 kW	500 kW
Average bore radius	0.34 cm	0.34 cm
Modulation factor (max.)	2.15	2.15
Transmission (at 40 mA current)	95%	100%
Input emittance (r.m.s., norm.)	0.2 π mm mrad	0.26 π mm mrad
Total normalized acceptance	3 π mm mrad	3 π mm mrad
Longitudinal output emittance (r.m.s.)	0.12 ° MeV	0.16 ° MeV
Output emittance (r.m.s., norm.)	0.2 π mm mrad	0.3 π mm mrad

Table 8: Parameters of 3 MeV chopper and chopper line.

Chopper pulse amplitude	±1 kV
Rise and fall time (10% to 90%)	2 ns
Pulse length	10 ns to 270 ns
Repetition rate	up to 44 MHz
Burst length	2.2 ms
Burst repetition rate	75 Hz
Number of chopper structures	2
Length of each chopper structure	60 cm
Vertical aperture of chopper 1	20 mm
Vertical aperture of chopper 2	30 mm
Focusing elements in chopper line	2 triplets, 2 doublets
Number of RF cavities (bunchers)	5
Total length of chopper line	6 m

Table 9: Parameters of the Drift Tube Linac.

	DTL section	CCDTL section	
Input energy	7	18	MeV
Output energy	18	120	MeV
Number of tanks	2	98	
Number of klystrons	2	9	
Peak RF power	1.6	7.1	MW
Tank diameter	0.47/0.49	0.58–0.47	m
Tank length	4.3/3.3	0.23–0.78	m
Aperture diameter	20	24	mm
Drift tube diameter	200	85	mm
Mean accelerating field	2–2.5	2.5	MV/m
Synchronous phase	–38/–30	–35/–25	(°)
Number of quadrupoles	58	98	
Overall length	8.4	69.6	m

Table 10: Parameters of the superconducting sections.

Section	Beta	W_{in} (MeV)	W_{out} (MeV)	No. of cavities	No. of cryostats	No. of tetrodes	No. of klystrons	Length (m)
1	0.52	120	237	42	14	42	–	101
2	0.7	237	389	32	8	32	–	80
3	0.8	389	1080	48	12	–	12	153
4	1	1080	2221	108	27	–	18	357
Total				230	61	74	30	691

Table 11: Superconducting cavity parameters at the design β.

	Beta	Gradient	Loaded Q_{ext}	R / Q	Filling time	Synchronous phase
		(MV/m)		(Ω)	(ms)	(°)
1	0.52	3.5	2×10^6	61	0.90	–25
2	0.7	5	2.5×10^6	108	1.13	–20
3	0.8	9	3×10^6	192	1.36	–15
4	1	7.5	2×10^6	234	0.90	–15

Table 12: Layout of the stretching and collimation line.

Element	Length [m]	No. of LEP cavities	No. of focusing periods	Cavity parameters
Bunch rotation 1	25.6	8	2	8.6 MV/m at ϕ = +90°
Drift	281.4		22	
Bunch rotation 2	12.8	2	1	4.4 MV/m at ϕ = –90°
Collimation	135.8		11	
Total	455.6			

d. Cryogenics, cooling, electricity and infrastructure parameters

Table 13: Review of heat loads for the superconducting section.

	Heat load values (per module)	Assumptions
Static losses	107 W @ 4.5 K	• 80 W for the module itself (measured during acceptance tests) • 27 W for the helium lines contribution (measured during acceptance tests)
Liquefaction	0.80 g/s of LHe	Couplers and tuners, measured consumption
Dynamic losses $\beta = 0.52$ $\beta = 0.7$ $\beta = 0.8$ $\beta = 1.0$	 82 W @ 4.5 K 196 W @ 4.5 K 732 W @ 4.5 K 210 W @ 4.5 K	• Corresponding to gradients and *Q* values of Table 4.6 • Considering 30% duty cycle (beam duty cycle plus pulse rise and fall time).
Thermal shields	6300 W @ 75 K (total)	Conservative value based on 10 W/m for 630 m of helium transfer lines

Table 14: Total cooling power required for the cryogenic system.

	Installed capacity	Comments (Equivalence @ 4.5 K)
Static losses	6.9 kW	1 W ↔ 1 W
Liquefaction	48.8 g/s	1 g/s ↔ 125 W
Dynamic losses	18.4 kW	1 W ↔ 1 W
Thermal shields (50 to 75 K)	6.3 kW	1 kW ↔ 70 W
Total equivalent at 4.5 K	32.0 kW	

Table 15: Electrical power requirements.

RF system	24 MW
Cryogenics	10 MW
Cooling and ventilation	2 MW
Other	1 MW
General services	3 MW
Total	40 MW

Table 16: Surface buildings.

Purpose	Name	Dimensions (m) Length × width × height	Materials	Particularities
Control room	SCX	10 × 10 × 10	Concrete–steel–glass	False floor under racks
Power converters	SR	40 × 15 × 8	Concrete–steel	False floor under racks Overhead crane 10 t
Helium compressor	SH	55 × 30 × 9.5	Concrete–concrete	Overhead crane 20 t
Cold boxes	SDH	40 × 25 × 12.5	Concrete–steel	Overhead crane 5 t
Slab floor tank helium		22.5 × 35	Concrete	–
Cooling–heating–ventilation	SU	15 × 12 × 6	Concrete–concrete	False floor 2 m Overhead crane 5 t
Electrical sub-station 18 kV		12 × 9 × 5	Concrete–concrete	False floor 2 m Overhead crane 5 t
Electrical sub-station 66 kV		15 × 12 × 5	Concrete–concrete	False floor 2 m Overhead crane 5 t
Air tunnel pulsion		10 × 9 × 4	Concrete–concrete	–
Air tunnel extraction		10 × 9 × 4	Concrete–concrete	–

Table 17: Primary cooling needs and cooling-circuit parameters.

Item	ΔT (K)	Power (kW)	ΔP (bar)	Flow rate (m^3/h)
Primary cooling SPL	15.6	6100	5	340
Cryo-compressors	7	8000	5	1200

Table 18: Secondary circuits.

Item	Fluid	Power (kW)	P_{max} (bar)	ΔT (K)	Flow rate (m^3/h)
Klystron	Doped water	4,000	8.5	20	175
RT cavities	Demineralized water	1,500	8.5	10	130
Magnets (quad)	Demineralized water	300	12	15	18
Magnets (bend)	Demineralized water	200	12	15	12
Dump linac	Demineralized water	100	12	15	6

Table 19: Tertiary circuits.

Item	Fluid	Power (kW)	ΔT (K)	Flow rate (m^3/h)
Dump linac	Demineralized water	100	15	9

Table 20: Ventilation loads.

Item	Internal load (kW)
Tunnel/gallery	50
Control room	30
SH	250 (ventilation only)

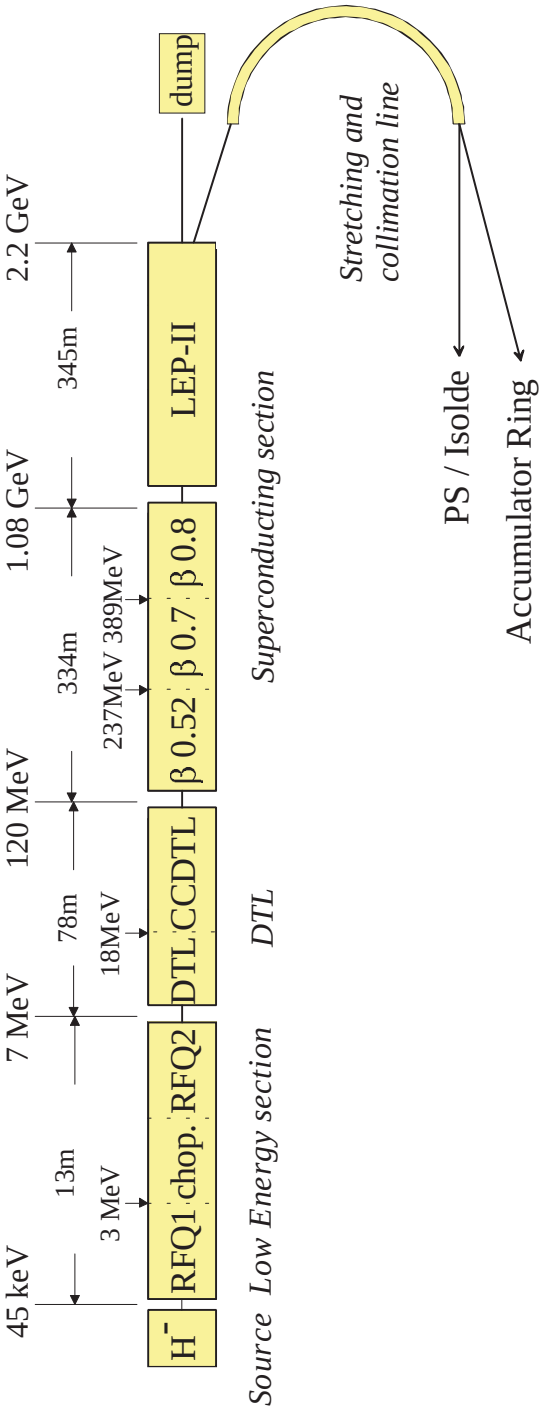

Layout of the SPL.

CERN 2000–012
15 December 2000

CONCEPTUAL DESIGN OF THE SPL, A HIGH-POWER SUPERCONDUCTING H⁻ LINAC AT CERN

ERRATUM

The following figure replaces Figure 2.2, page 5

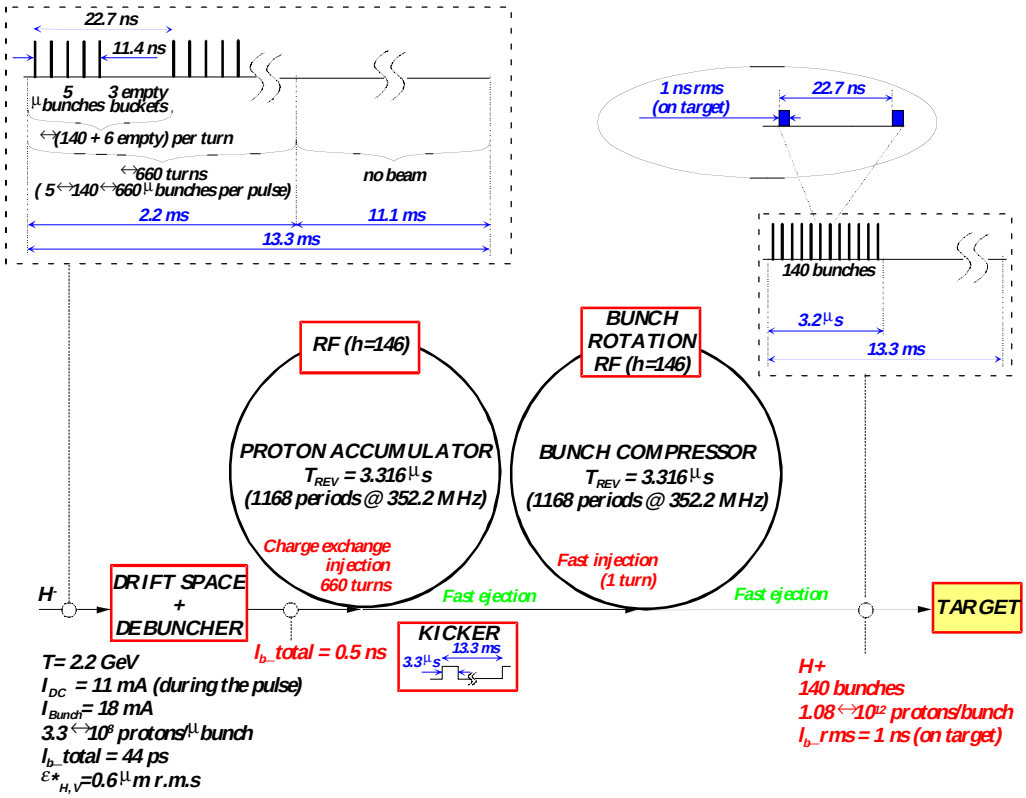

Fig. 2.2: Beam time structure in the proton driver machines.